POLITECNICO DI TORINO

Corso di Laurea Magistrale in Ingegneria Civile

Tesi di Laurea Magistrale

An application to the Queensferry Crossing Structural Health Monitoring system data: Parameter estimation on concrete used for the Central Tower

Relatore:
Prof. Rosario Ceravolo

Correlatore:
Prof. Daniele Zonta

Candidato:
Francesco Lovero

A.A. 2018/2019

Abstract

Structural Health Monitoring (SHM) is a popular and growing research field, providing a powerful tool for damage assessment and performance evaluation of engineering structures. SHM system applications, based on advanced sensors and real-time monitoring, offer great potential for informed and effective management of large infrastructures, such as long-span bridges. It is certainly a powerful instrument that helps engineering assessments about the status of a structure and its lifecycle behaviour. However, data collection from SHM systems not only supports maintenance level but also represents an important source of information that can be analysed in order to evaluate structural members' properties.

The aim of this thesis is the application of SHM principles to data collected during the construction of the Queensferry Crossing, a three tower cable-stayed bridge crossing the Firth of Forth near Edinburgh, Scotland. The bridge opened to the public on the 30th of August 2017. It is a statically indeterminate structure, composed of two approach viaducts on the North and South sides that connect the cable-stayed bridge to the mainland. The bridge was provided of an extensive SHM system since the construction operations and proved to be an ideal subject for a case study.

As the work focused on strain data registered on towers concrete, deck erection method was highlighted during the observations. Indeed, it was built using a balanced cantilever process, resulting in the bridge spans fanning out from the towers and, at one point during the construction, the central tower span was the longest free standing cantilever structure in the world. The data gathered during the erection of the towers and main bridge deck from the SHM system on the central tower were analysed to determine when key construction operations took place and their effect on the data.

At a later stage, the same data were used to understand the contracting behaviour of the concrete during the first three and a half years after casting. More specifically, data were processed to estimate the elastic, creep, shrinkage and temperature contributions to the strain. Two different parameter estimation methods were applied: the *Least Squares Analysis* (LSA) and the *Bayesian inference* (BA). A parametric model of the strain has been built, in order to estimate some parameters of the concrete: the modulus of elasticity E [MPa], the creep coefficient φ [-], the shrinkage strain at t=∞ $\varepsilon_{s,\infty}$ [$\mu\varepsilon$] and the thermal

coefficient α [με/°C]. At the end of the estimation process, huge differences between the results coming out of the two methods were found and discussed. The LSA is a regression analysis that approximates the solution using the least squares criterion: the solution is the one that minimizes the sum of the squares of the residuals (the difference between the observations and the model output). The BA approach is a method of statistical inference that relies on the Bayes' theorem; it proved to be a more accurate method for the evaluation of the parameters, since it takes into account both the uncertainties of the model and the *a priori* knowledge of the parameters. In particular, engineering judgements and regulations were used as prior information. To perform the calculation of the expected values of the parameters and their corresponding uncertainties, in order to reduce the computational effort, the author employed the Metropolis-Hastings (MH) algorithm for the BA. In this way a set of expected mean values, a covariance matrix and a correlation matrix were obtained.

Finally, after the estimation of the parameters, the temperature compensated strain was evaluated and plotted. Then, some analytical calculations were performed in order to give evidence to the estimated parameters values.

1. INTRODUCTION

Structural Health Monitoring (SHM) is a process of in-service health assessment for a structure through an automated monitoring system, and it is a key element of cost-effective strategies for condition-based maintenance. A SHM strategy consists of many important components including sensing network, data processing and analysis, damage assessment and decision-making. SHM technology has the great potential to offer significant economic and life-safety benefits. However, the application of the SHM technology to actual civil engineering structures is still in its infancy, and it requires advancements in various fields due to its multi-disciplinary nature. Extensive further works are therefore needed to ensure that infrastructure managers benefit from this emerging technology (Hua-Peng, et al., 2018).

The structural health monitoring process involves the observation and evaluation of a structure over time using periodically sampled measurements from a sensing system. Structural health monitoring is a popular and growing research field, providing a powerful tool for damage assessment and performance evaluation of engineering structures.

In this work, a case study of the monitoring process and assessment of an exhaustive Structural Health Monitoring system has been considered and presented. The structure in exam is the Queensferry Crossing, which is the newest of the three bridges crossing the Firth of Forth, and connecting Edinburgh, at South Queensferry, to Fife, at North Queensferry.

The Queensferry Crossing, the world's longest three tower cable-stayed bridge was opened to traffic on August the 30th 2017. This was the largest infrastructure project in Scotland for a generation (Watt, 2017). The bridge has a large SHM deployment, consisting of a variety of different sensor types. The system is intended to provide almost real-time information about structural behaviour during its service life. As most of the sensors were installed during the construction of the bridge, they started to collect data since the moment of their application to the structure, so that also construction operations were monitored in order to ensure that no unexpected effects were occurring on the already placed structural elements.

This chapter first aims to give a clear overview of SHM systems technology, framework and strategy, as well as to present the potential benefits of the application of SHM to civil engineering structures.

1.1 Aims

The aims of this thesis are as follows:

- to develop a thorough enough understanding of the structural scheme and construction of the Queensferry Crossing to enable adequate analysis of the data from the sensors;
- to infer what construction operations are taking place by analysing the SHM data;
- to interpret strain data and understand their correlation with temperature;
- to build a realistic parametric strain model that could be compared with strain data and, then, to estimate concrete parameters related to each strain component;
- to provide evidence to support the inferences made and the results obtained.

1.2 Structural Health Monitoring (SHM)

Maintaining safe and reliable civil infrastructure for daily use is critical to the well-being of the society. Thus, structural health can be stated as its current capacity for providing intended level of service in a safe and cost-effective manner against the expected hazards during its service life.

The deterioration over time of civil engineering structures is a commonly acknowledged concern. This day can be caused by various reasons, including:

- Failure due to cyclic traffic loads;
- Effects of environmental factors (e.g. steel corrosion, concrete carbonation);
- Aging of the construction materials;
- Damage due to exceptional events, such as earthquakes, hurricanes and floods;
- Normal load conditions during lifetime.

All these factors are variables with uncertainties, so it is difficult to define the structural health in terms of its age and usage and its level of safety to resist severe natural actions. In order to reliably assess structural health and maintain structural safety, continued in-service monitoring of the structure is essential.

Currently, the condition assessment of existing civil infrastructure such as bridges largely depends on visual inspection. This subjective and inaccurate condition assessment methodology has been identified as the most critical technical barrier to effective infrastructure management. For example, condition of bridges is typically expressed in terms of subjective indices based on visual inspection alone. Thus, it is difficult to accurately evaluate structural condition from the inaccurate visual inspection data, even when this may be conducted by experts (Aktan, et al., 1998).

Health monitoring applications based on advanced sensors and real-time monitoring for civil infrastructure offer great potential for informed and effective infrastructure management. It is necessary for civil engineering structures since they may exhibit premature deterioration, structural damage and performance problems, or they may even have aged beyond their expected design life. Health monitoring can be utilised for tracking the responses of a structure along with inputs, if possible, over a sufficient duration to determine anomalies, to detect deterioration and to assess damage for decision-making. Thus, one can assess the performance of civil structures in a proactive manner using measured data and data interpretation algorithms, in order to correctly evaluate the current condition and to predict the remaining service life.

1.2.1 SHM Aims

SHM uses sensing systems and associated hardware and software facilities to control the structural performance and operational environments of engineering structures. By means of the observed data and of periodically sampled structural response, it allows the evaluation of the current state and future performance of the structures.

The output of this process is periodically updated information regarding the capability of the structure to perform its intended function, by considering the inevitable aging and degradation resulting from environmental factors. SHM aims to identify structural damage and evaluate the health of the structure using monitored data. Damage is defined here as changes to the material and/or geometric properties of a structure, which affects the current state.

In addition, SHM strategies offer useful information for optimising maintenance planning during service life. In order to guarantee a reliable operation and to schedule maintenance

and repair work in a cost-effective manner, it is necessary to continuously monitor and assess the structural performance.

1.2.2 SHM Research Development

Nowadays, SHM is a popular and still growing research field, which is progressively more becoming a focus of the civil engineering community. The reasons why increasingly more attention is given to this sector are several and concern with technological developments, as well as public safety issues.

The main technological advancements, which are accredited to the increase in implementation and research, are: the increases in cost effective computer memory, advances in sensor technology such as smart sensors and wireless sensors, and advancement of finite element modelling techniques (Doebling, et al., 1998).

The use of wireless sensor networks have the potential to increase SHM deployments. These networks can dramatically reduce the cost of implementation of SHM, in comparison to tethered sensor networks (Lynch, et al., 2006). The reduction in cost of these systems increases their viability in the eyes of structure owners/managers, who must balance the cost of SHM technologies with the benefits expected. The reduced cost per sensor also enables deployments with increased sensors density. This is particularly useful for global SHM distributions on bridges. An increased sensor density can obviously lead to improvements in monitoring reliability (Lynch, et al., 2006).

Another reason that led to an increasing research in this field is the growing pressures of managing ageing infrastructures, mainly coming from American infrastructure management issues. A tangible example is the I-35W Bridge collapse across the Mississippi river in Minneapolis, in 2007.

Figure 1.1. I-35W Bridge collapse (thorntontomasetti.com)

This event highlighted public safety issues related to the ageing infrastructures management, since the catastrophic failure occurred during the evening rush hour and causing the death of 13 people and a total amount of 145 injured. Since 1993, the bridge was inspected annually by Mn/DOT, although no inspection report was completed in 2007, due to the construction work. In the years prior to the collapse, several reports cited problems with the bridge structure. In 1990, the federal government gave the I-35W Bridge a rating of "structurally deficient", citing significant corrosion in its bearings. However, approximately 75000 other U.S. bridges had this classification in 2007 (Anderson, et al., 2007). In 2001, a report drafted by the civil engineering department of the University of Minnesota concluded that although the bridge should not have any problems with fatigue cracking in the near future, regular inspection, structural health monitoring, and use of strain gauges had been suggested. In 2005, federal bridge inspectors rated the bridge at 50 (on a scale from 0 to 100), indicating that replacement may have been in order. On a separate measure, the I-35W bridge was rated "structurally deficient", but was deemed to have met "minimum tolerable limits to be left in place as it is" (Dedman, 2007). In January 2007, periodic safety inspections were prescribed but 7 month later the bridge came down. Needless to point out how the presence of sensors real-time monitoring the structure would have been lifesaving.

Finally, regulatory requirements in Asian countries such as in China are driving current research and commercial development of SHM systems for civil engineering structures, since companies that build bridges are obliged to periodically certify their health (Farrar, et al., 2007).

These were the reasons that led to an increasing of attention to Structural Health Monitoring by the community in the last decades.

1.2.3 SHM Monitoring Systems and Methods

Health monitoring systems for civil structures require a proper number of sensing systems collecting data and data interpretation algorithms evaluating registered data. Generally, damage identification and safety assessment depend on the control of both local and global effects.

SHM system generally consists of many key components, including:

- *Sensors*: the choice of the type, number and location of the sensors is essential to obtain the right data to be analysed and interpreted;
- *Data Acquisition*: selection of the excitation methods, signal conditioning and data acquisition hardware;
- *Data Transmission*: once data are measured, they need to be transmitted by wired or wireless networks;
- *Data Processing & Management*: data are processed by validation, normalisation, cleansing, fusion and compression procedures, and then properly stored and managed;
- *Health Evaluation & Decision Making*: the final phase involves the health assessment and the consequent decision about the possible intervention.

The selection of SHM system and method of course depends on both structure disposition and what we want to analyse. SHM strategies can be categorised in global and local monitoring strategies.

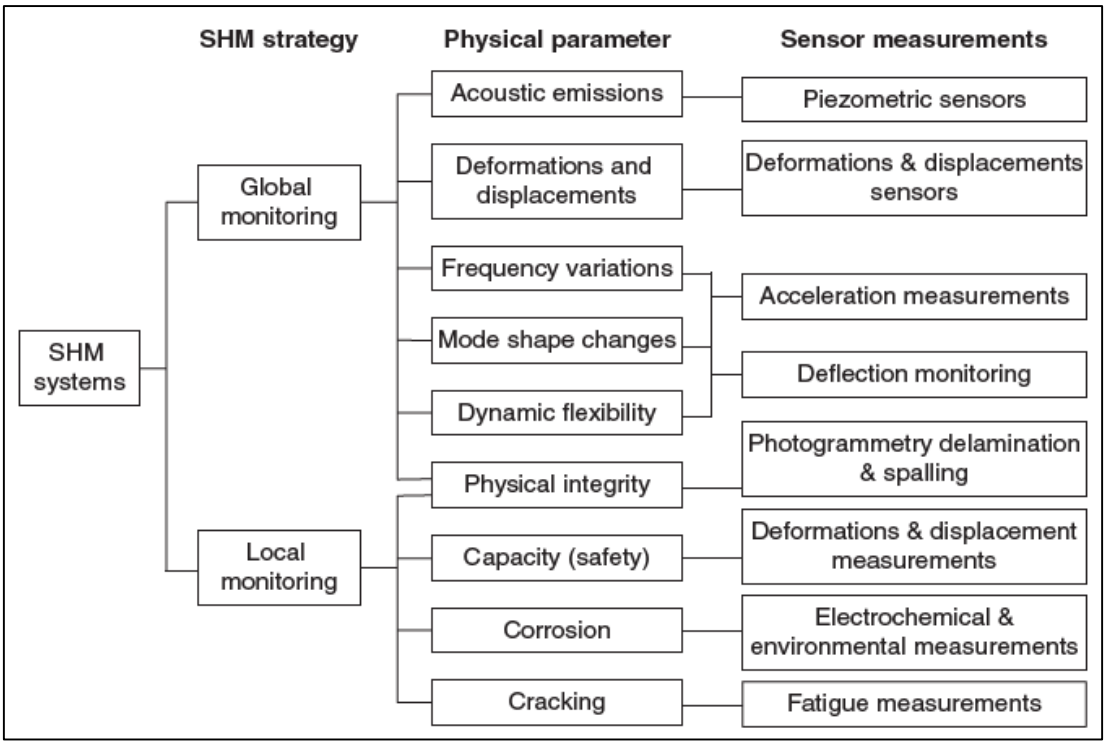

Figure 1.2. Structural health monitoring strategies for civil engineering structures (Frangopol & Messervey, 2009)

Global monitoring strategies have been the traditional tool used to assess the safety of civil engineering structures such as bridges. Ideally, by use of measured parameters, health monitoring of civil structures has the ability to identify the location and severity of damage in the structures when damage occurs. However, existing global SHM methods, such as some vibration based damage detection methods, may only determine whether or not damage is present somewhere in the entire structure. Once damage presence is detected, local SHM methods, such as guided waves to measure the state of stress or eddy current techniques to locate cracks, are adopted to determine the exact location and extent of the damage.

1.2.4 Potential benefits of SHM and Motivation for progress

The uncertainties that cover the design and the construction of the major civil structures, together with environmental factors affecting their in-service behaviour, and potential changes in use (in terms of load applied), make lifetime monitoring necessary to the safety of their users.

In many cases, because of on-site construction restraints, the structure may not be constructed strictly according to the archived design. Accuracy of implementation and

uncertainty of workmanship are often an issue. Total uniformity of material can never be achieved when concrete materials are used. Physical models based on idealised behaviour such as perfect pin or rigid connections can never reflect what is achieved in practice. Availability of data to obtain an accurate analytical model is often not possible. This problem makes model-based health monitoring of civil infrastructure a challenge (Chang, et al., 2003).

Furthermore, civil structures deteriorate with time because of operational loads, environmental effects, fatigue and exceptional events such as earthquakes. Deterioration of structures may be accelerated by increasing loads that were not expected at design stage. This has been identified as one of the reasons of the *Viadotto Polcevera* (Genova, Italy) decay and then its partial collapse in August 2018 that caused the death of 43 people. This structure was particularly affected by corrosion and premature aging during its lifetime, since lots of maintenance and strengthening interventions were executed on it. The prevention or early warning of such an event is one reason for the implementation of SHM.

It is expected that the further development of SHM systems in civil engineering will lead to the establishment of a comprehensive methodology for automated health monitoring of civil structures, so that true condition based inspection and maintenance would become a reality (Karbhari, 2009). In addition, the use of an appropriately designed SHM system would enable further understanding of structural response through data analysis and interpretation.

Innovations in SHM technologies would positively affect civil structures design and management in several ways (Frangopol, et al., 2009; Ko, et al., 2005). Both public safety and owners' economy would benefit from the use and the innovation of these technologies, including:

- No unnecessary economic losses due to unpredicted downtime, for instance due to bridge repairs or inspections;
- Longer service life, as safe operation beyond design service life can be made possible;
- Any inaccessible areas of a structure can be assessed to increase safety, while these areas may have been neglected in a visual inspection routine;

- Routine inspections carried at specific time intervals don’t allow to detect any unexpected faults occurring in between scheduled inspections, putting in danger people’s lives, while SHM technologies would be continously working;
- On the other hand, it would be possible to draw up a cost-effective maintenance program, since SHM enables condition-based/corrective maintenance, that is maintenance is only carried out when damage is detected (instead for example of a periodic substitution of elements that actually are in perfect conditions).

All of these reasons could be useful to lead to an increasingly more research and innovation in this field.

2. Case study: The Queensferry Crossing

The Queensferry Crossing, built between 2011 and 2017 and opened to traffic the 30th August 2017, represent the longest three-tower, cable-stayed bridge in the world and it is considered one of the major Scottish infrastructure project and the biggest undertaken for a generation (Watt, 2017). The total cost reached £1,35 billion, although the estimated cost was initially set between £3,2 and £4,2 billion. It is the third bridge across the Firth of Forth, connecting Edinburgh, at South Queensferry, and Fife, at North Queensferry, standing along the other two iconic bridges: the *Forth Bridge* (FB) (the famous nineteenth-century cantilever rail bridge) and the *Forth Road Bridge* (FRB) (the suspended road bridge built in the 60s).

Figure 2.1 Geographical position of the Queensferry Crossing

Figure 2.2. The three bridges over the Firth of Forth *(BBC, 2017)*

Behind this project for a new bridge crossing the Firth of Forth was the need to lighten road transport from the FRB, since it began to show deterioration issues during the early 2000s. The Forth Road Bridge, opened in 1964, carried around 4 million vehicles per year, at the beginning of its life, while half a century later it was carrying around 24 million vehicles per year. This dramatic vehicles traffic increase is considered one of the main reasons that brought significant wear and tear (Shackman, et al., 2016). Therefore, the detected warning corrosion of the main suspension cables (an estimated 8% loss of their total strength was identified in 2004, 10% in 2008) together with other maintenance issues resulted in the need for a replacement crossing of the estuary. Moreover, the failure of a truss-end link in December 2015, which caused a 3-week closure to traffic with the consequent inevitable inconveniences and traffic disruption, remarked that the new bridge was not only just a necessity but also essential to keep alive this important transport link (Watt, 2017). The new infrastructure had also to improve the reliability of travelling across the Forth by addressing issues which frequently affected the FRB, including the lack of hard shoulders to manage vehicle breakdowns and maintenance activities, and lack of wind shielding, which results in closure for certain types of vehicles during high winds (Shackman, et al., 2016).

As a consequence of the problems highlighted by the FRB conditions, in 2006 Transport Scotland commissioned the Forth replacement crossing (FRC) study to determine the best solution.

2.1 Forth Replacement Crossing Study and development

Within the project study, eight transport-planning objectives were established based on: capacity, accessibility, environment, maintainability, connectivity, reliability, increasing travel choices and sustainable development. A key objective was that traffic capacity should generally remain at 2006 levels and any replacement crossing should not result in a marked increase in cross-Forth traffic levels (Shackman, et al., 2016). A total amount of 65 crossing options were identified at an early stage, including tunnels, bridges and barrages, but only five potential crossing corridors satisfied the requirements.

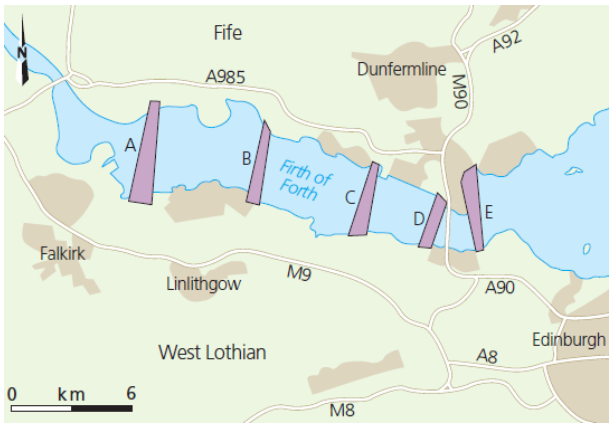

Figure 2.3. The five potential corridors *(Shackman, et al., 2016)*

Corridors A and B were ruled out due to the length of the crossing and the major infrastructure works that would be required to connect to the road network on the North side of the bridge. Corridors C and E were deemed to be unsuitable for bridge construction due to their proximity to Special Protected Areas, which are important habitats for migratory birds (Shackman, et al., 2016). Therefore four options were left to be considered, a tunnel at corridor C, D, E or a bridge at D.

Option	Length	Construction time	Capital cost 2006 Q4 prices
Corridor C – tunnel	8.5km	7.5 yrs	£2.3bn
Corridor D – suspension bridge	1.4km main span	6 yrs	£1.7bn
Corridor D – cable stayed bridge	1.3km main span	5.5 yrs	£1.5bn
Corridor D – tunnel	7.3km	7.5 yrs	£2.2bn
Corridor E – immersed tube tunnel	7.3km	7.5 yrs	£2.5bn

Figure 2.4. Options cost assessment table *(Scherie, 2010)*

Measure	Tunnel C	Tunnel D	C-S Bridge D	Spn Bridge D	Tunnel E
Present value of benefits	4,655	5,303	6,026	6,026	6,317
Present value of costs	-2,087	-1,968	-1,397	-1,575	-2,172
Net present value	2,568	3,335	4,629	4,451	4,145
Benefit to cost ratio	**2.2:1**	**2.7:1**	**4.3:1**	**3.8:1**	**2.9:1**

Figure 2.5. Costs and benefits of each option (£ million) *(Scherie, 2010)*

At the end of a cost-benefit analysis, the cable-stayed bridge option along the corridor D resulted the best fitting solution. This alignment makes use of Beamer Rock, a natural dolerite outcrop in the middle of the Forth, providing a apposite foundation for the central tower of a three-tower cable-stayed bridge. A wide range of design issues were addressed including the following (Shackman, et al., 2016):

- Stabilisation of the central tower: the large deflections and the instability of the central tower that a three-tower cable-stayed bridge implicates led to the adoption of a length of crossed cables at mid-span, which also helped to provide a slender deck and towers (see also aesthetics);
- Navigation clearances: at least equivalent to that provided by the FRB and FB;
- Wind shielding: to provide almost guaranteed possibility to cross in high winds and to maintain views by using transparent barriers;
- Ship impact: investigations on the type of navigation over the Forth were made in order to study the risk of boat crashing on towers or piers, resulting in an increased protection to the south tower and adjacent pier;
- Tower foundations: design extensive ground and marine investigations were undertaken, resulting that both caissons and piles were considered to be acceptable solutions;
- Deck type/shape: a trapezoidal-shaped deck (aerodynamic box with smooth surfaces) was preferred to minimise future maintenance, assist with wind loading and improve aesthetics, while choice of materials (orthotropic or composite) was left open;
- Aesthetics: the proximity to the FRB and the FB influenced the design, since no visual conflict should have been.

As a result, the general arrangement consisted of a three-tower, cable-stayed bridge with southern and northern approach viaducts, for a total length of 2,64 km.

2.2 Design and Structural scheme

The total length of the bridge is exactly 2638 m and it is divided into a central cable-stayed bridge (about 2,02 km long), a southern and a northern approach viaduct (respectively 543 m and 75 m long). The structure is continuous from abutment to abutment with no intermediate movement joints. Longitudinal fixity is provided by a monolithic connection at the central tower founded on Beamer Rock, while transverse support to the deck is provided at all towers and piers (Carter, et al., 2010).

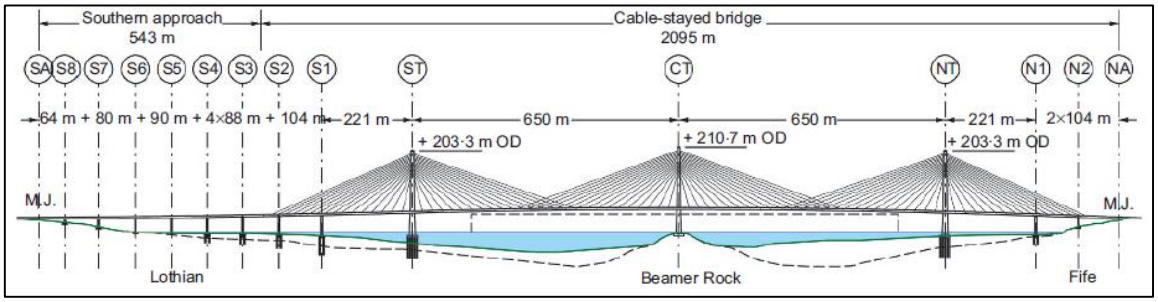

Figure 2.6. Queensferry Crossing scheme *(Carter, et al., 2010)*

The slender towers are vertical, reinforced concrete structures tapering with height, located in the middle of the road deck with two planes of stay cables anchored centrally. The cable-stayed deck is an aerodynamic-shaped (trapezoidal) composite box girder (almost 40 m wide) supported by a total amount of 228 cable, while for the two approach viaducts a twin-box section providing continuity with the cable-stayed bridge, supported by V-shaped piers, was chosen.

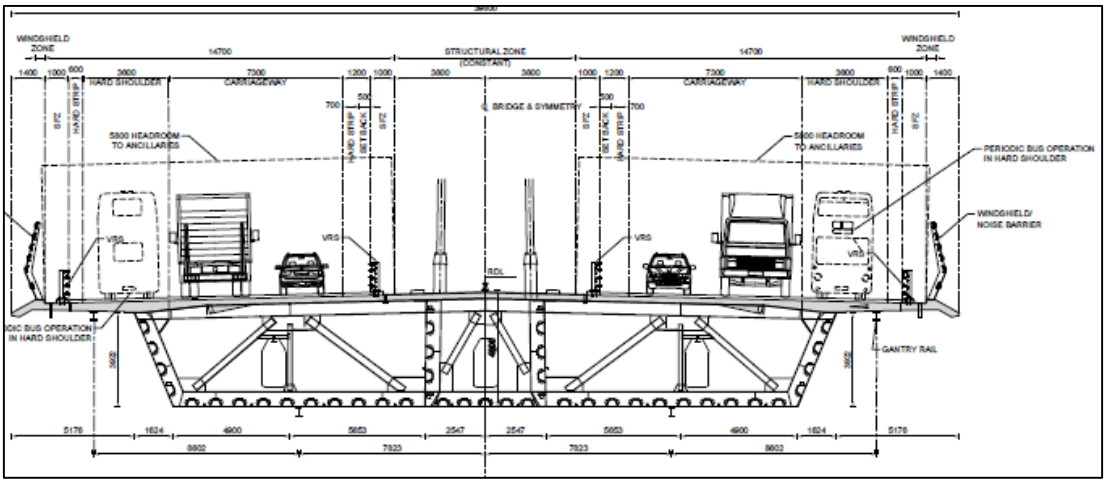

Figure 2.7. Single box deck section (cable-stayed bridge) *(Transport Scotland, 2015)*

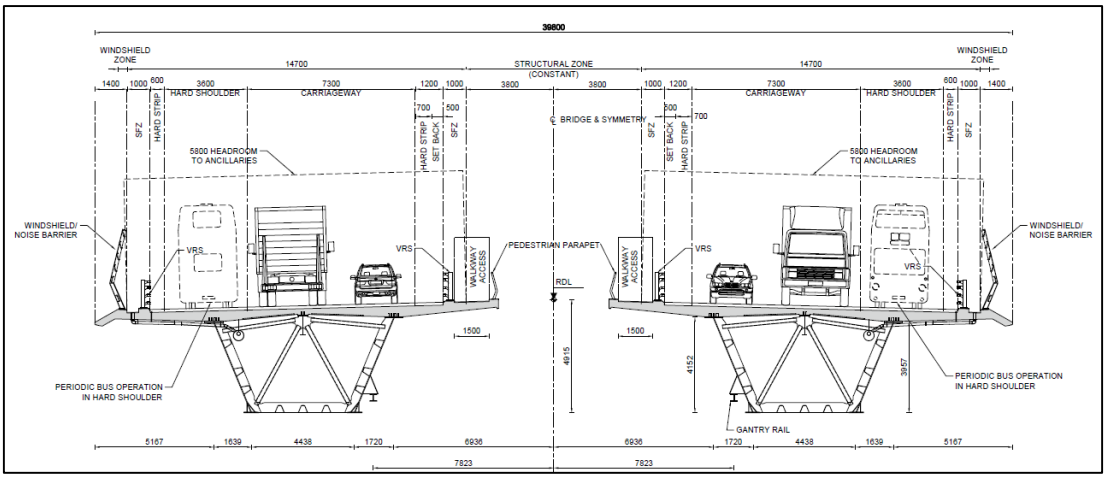

Figure 2.8. Twin-box deck section (viaducts) *(Transport Scotland, 2015)*

The main challenge of the design process was the stabilisation of the central tower. This tower cannot be directly supported by being tied back to anchor piers so that out-of-balance live load on one of the main spans would induce a significant sway of the central tower, resulting in large deflections and large bending moments in the tower and deck. (Carter, et al., 2010). Several solutions were developed, mostly inspired by already existing bridge. The finally adopted method consisted in overlapping or crossing the stay cables over approximately 25% of each main span in order to create a virtual truss-system.

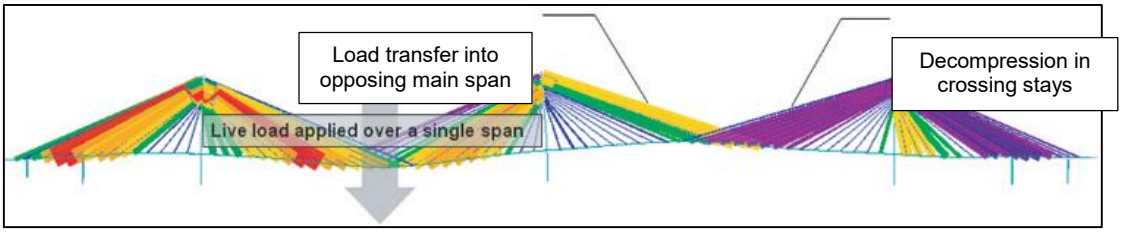

Figure 2.9. Crossing stay cable system *(Carter, et al., 2010)*

The virtual truss system of the crossing stay cables provides overall global stiffness, improving both the static and dynamic performance, as explained in ***Figure 2.10*** and ***2.11***, where deflections in the two cases (crossing and non-crossing cables) are displayed with a comparison between composite and orthotropic deck.

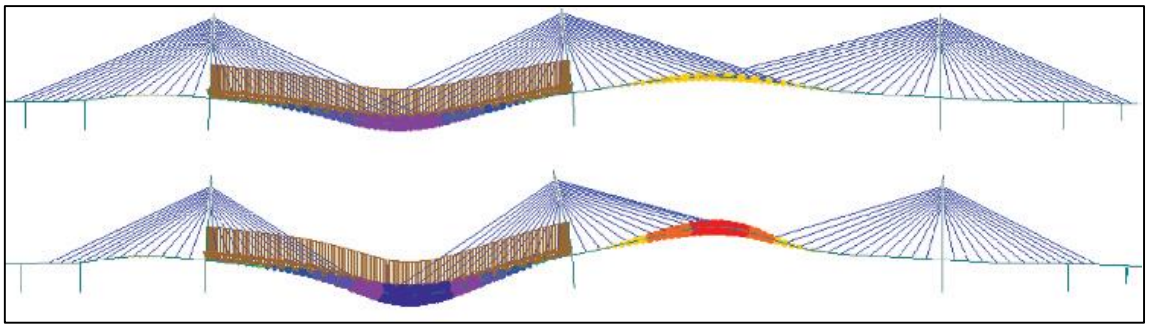

Figure 2.10. Bridge deflections for live load on one span with (above) and without (below) crossing cables *(Carter, et al., 2010)*

	Maximum live load deflection: m	
Cable-stayed bridge variant	With crossing stay cables	Without crossing stay cables
Orthotropic deck	3·5	4·7 (35% higher)
Composite deck	2·4	3·0 (25% higher)

Figure 2.11. Maximum live load deflections *(Carter, et al., 2010)*

A more flexible orthotropic deck would have needed the presence of crossing cables, since deflections without them would have caused concerns over serviceability performance. Although the composite deck did not show the same issues, overlapping cables were in any case adopted since bending moment was much bigger without them, as shown in ***Figure 2.12***.

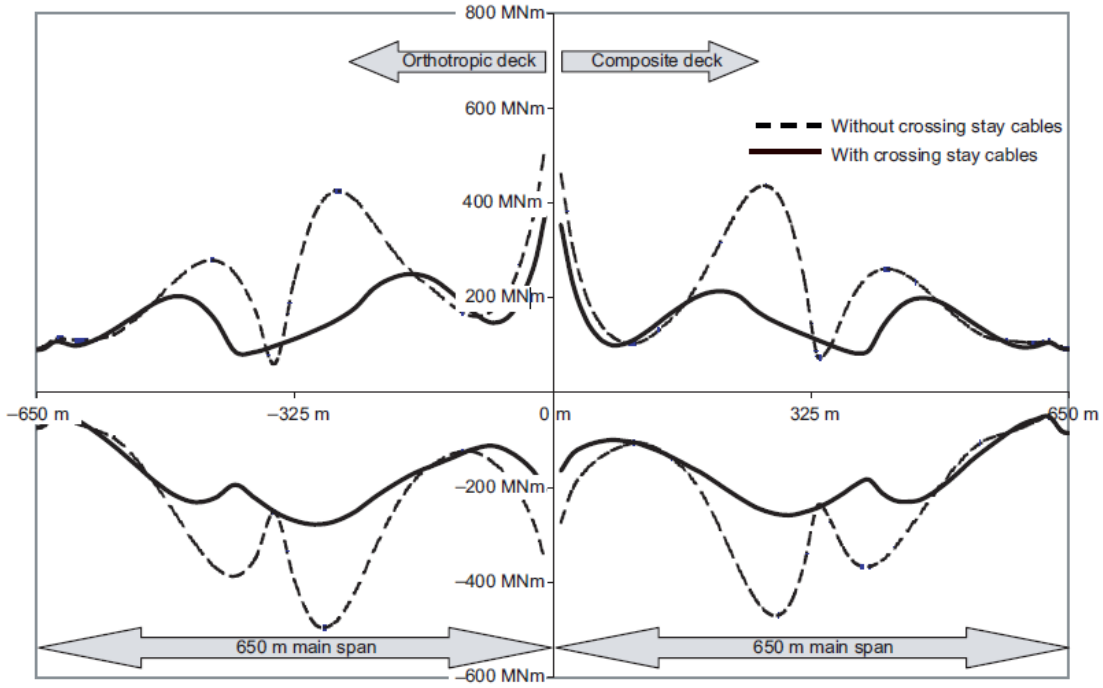

Figure 2.12. Live load moment envelopes in the cable-stayed bridge main spans *(Carter, et al., 2010)*

Another significant advantage provided by the implementation of crossing cables concerns the longitudinal overturning moment at the base of the central tower, since it was reduced by 30%.

2.3 Main structural elements and their construction

As already mentioned, the construction of this huge infrastructure has involved several construction operations and phases to realize the different structural components that both the substructure (foundations, towers, piers and abutments) and the superstructure (deck,

stay-cables and viaducts). The whole bridge is supported by a total of ten V-shaped piers, three towers up to 210 m high and two abutments on the north and south ends of the bridge deck. The substructures are founded on a variety of footings constructed by means of open-pit excavations, prefabricated and in situ sheet pile cofferdams and three deep-water caissons.

Beside the in-service conditions, the substructures had to be designed for the governing erection stages. The deck launching activities governed the design of the approach piers and abutments; while, for the towers, the free cantilevering erection of the deck represented the governing design stage. In addition to the structural needs, there were also high functional requirements such as accessibility and installations for an intelligent traffic management and structural health monitoring system (Romberg, et al., 2018).

In this section, the main structural elements will be described with the key design features being highlighted. A detailed mention will also be given of their construction operation systems.

2.3.1 Foundations

One of the most important elements in the long-term viability of any bridge structure has always been the foundations. In a cable-stayed bridge, the quality of this component is critical to the stability of the tower, which house the anchors for the cables that hold on the bridge. The main task was the construction of foundations in the challenging marine environment of the Firth of Forth. In total the bridge has 15 foundations, ten in the estuary and five on land. The foundations in the estuary clearly presented the greatest challenge. This was due to the depth of water, significant currents, depth of superficial soils and the potential for large ship impact loads (Johnston, et al., 2015).

The main issue was to keep the water out when pouring concrete for those foundations that had to be in the sea. In this case, two different solution were adopted: *caissons* (used for the North and South Tower and the pier S1, see ***Fig.2.6***), where the water level was deeper, and *cofferdams* (for the Central Tower and piers S2 to S6 and N1), in shallow water. A third method – *open excavation* – was used for the piers S7, S8 and N2, located on dry land, as well as for the two abutments. Towers foundation construction systems will be illustrated.

Caissons

The three caissons were fabricated by Polish fabricators and their scale was remarkable (diameters ranging from 25 to 30 m). The largest one, used for the ST foundation was 30 m high by 32 m in diameter, with a total weight of 1200 tonnes (Watt, 2017). Once completed, the caissons were moved on to specially designed barges and transported to the Firth of Forth, where they were off-loaded in Rosyth Docks. Here, final preparations and checks were made, then they were taken out to their final destinations and finally installed with a horizontal accuracy of 200 mm, thanks to the use of the latest GPS satellite technology.

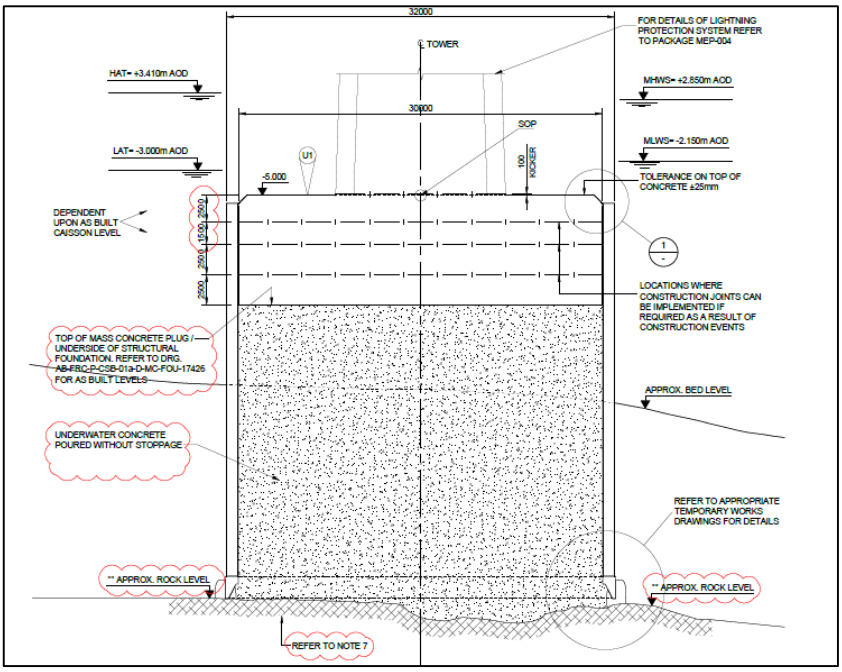

Figure 2.13. South Tower foundation general arrangement drawing, detailing steel caisson with mass concrete plug *(Ramboll ii, 2015)*

Caissons installation was a difficult process, since it consists of several operations. Once each caisson was close to the final position, concrete was poured into the annulus (a one-meter void between the inner and outer skins of the caisson) to provide strengthening of the cutting shoe; then a huge floating sheerleg crane, specially designed for the purpose, guided the steel structure into the position. The sinking operation for each main caisson was a complex and sensitive procedure. Sinking was achieved by water ballasting, this operation was monitored using piezometers and flowmeters.

Figure 2.14. Caissons positioning with floating cranes *(Transport Scotland, 2014)*

The lowering operations were aided by excavations taking place inside the caissons. Excavation of the inner layers of soil allowed the cutting toe of the caissons to displace soil around the outer ring, resulting in the sinking of the caisson. To complement this, bentonite slurry was injected at pressure through the nozzles on the cutting toe, thus lubricating the outer walls and assisting sinking (Johnston, et al., 2015). As they descended, the caissons were monitored to ensure they were going down vertically, any tilt being constantly corrected by ballasting and further excavation. Once the caisson was at formation level a continuous ring of jet grouted columns were formed around the outside of the base of the caisson, to prevent sea water and sediment seeping in (Watt, 2017). The inside walls could then be cleaned, using a jet car system, to ensure sufficient bond strength would be able to develop between the concrete plug and the steel caisson. To enable the completion of the nonstop pours for each concrete plug a batching plant for concrete was constructed at the Roysth docks, which ensured a constant supply of concrete. Four specially designed barges were also developed and used to deliver and pour the concrete in a continuous cycle (FRC, 2013). The dewatering of the caissons was carried out seven days after completion of the concrete plug pour. This was achieved using riser pipes and pumps attached to the temporary caissons. Upon completion of dewatering, construction of the tower base begins in the temporary caisson.

Cofferdams

The foundation of the Central Tower is an octagonal cofferdam anchored deep in the Beamer Rock, a dolerite rock outcrop in the middle of the Forth, which is exposed during low tide. In order to create a watertight cofferdam, it was necessary to remove the navigation light (present until then on Beamer Rock) and to blast a hole 6 m deep, removing a total of 5000 cubic meters of rock. Pre-formed, 10,7 m high, L-shaped panels with reinforced concrete base and steel sheet pile walls were transported to the site by means of barges and then lifted into position. The panels were then laid down to the desired level and underwater concrete was placed to fill the gap between the precast unit and the rock. The gaps in the sheet pile cofferdam were infilled with individual sheet piles and the joints sealed. Then the cofferdam was dewatered and then reinforced concrete was poured in to form the CT foundation.

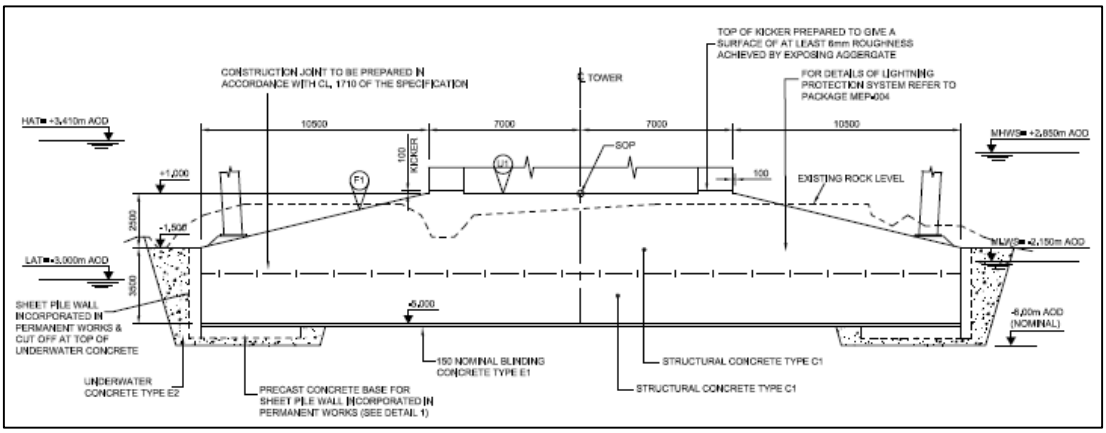

Figure 2.15. Central Tower foundation drawing *(Ramboll i, 2015)*

Main structural features

All three of the towers required reinforced concrete foundations, the dimensions, depths and construction methods varied for each tower.

Central tower foundation is an octagonal shape footprint, which dimension are 35 m in the longitudinal direction and 25 m in the transverse direction, with a height that grows from 3,5 m to 6 m inwards. Its base level is fixed at -5 m AOD (above Ordnance Datum).

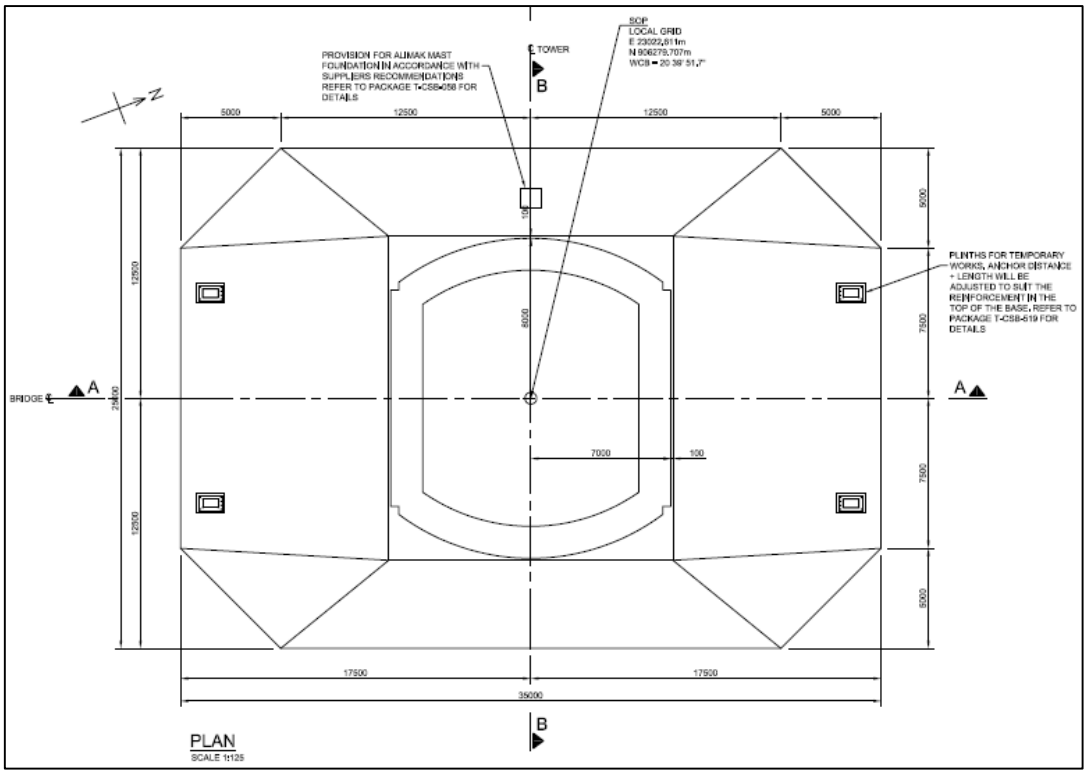

Figure 2.16. Central Tower foundation, Plan *(Ramboll i, 2015)*

The foundations for both the ST and NT are circular and have dimensions Ø30m×9m and Ø24m×9m respectively.

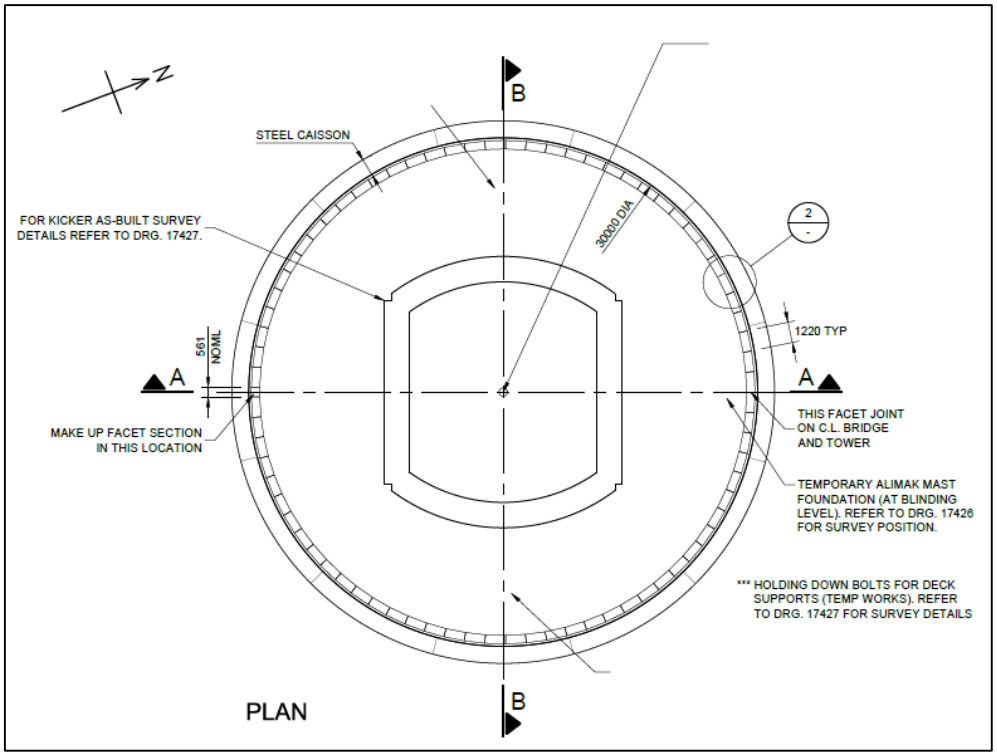

Figure 2.17. South Tower foundation, Plan *(Ramboll ii, 2015)*

2.3.2 Towers

The central tower (CT) is the highest point of the bridge at +210,7 m above Ordnance Datum (AOD), compared with +202,3 m AOD for both of the flanking towers (FTs) (i.e. the north and south tower).

The bridge is monolithically connected to the CT (full restraint in longitudinal and transverse directions), while the deck is transversally fixed to the FTs by wind bearings, in order to reduce restraint forces due to temperature movements. Any deck torsion from eccentric traffic configurations is only restrained at the CT and the anchor piers with a torsion span of 870 m (Romberg, et al., 2018). During construction, temporary bearings were placed at the FTs to provide longitudinal and torsion restraints to the deck.

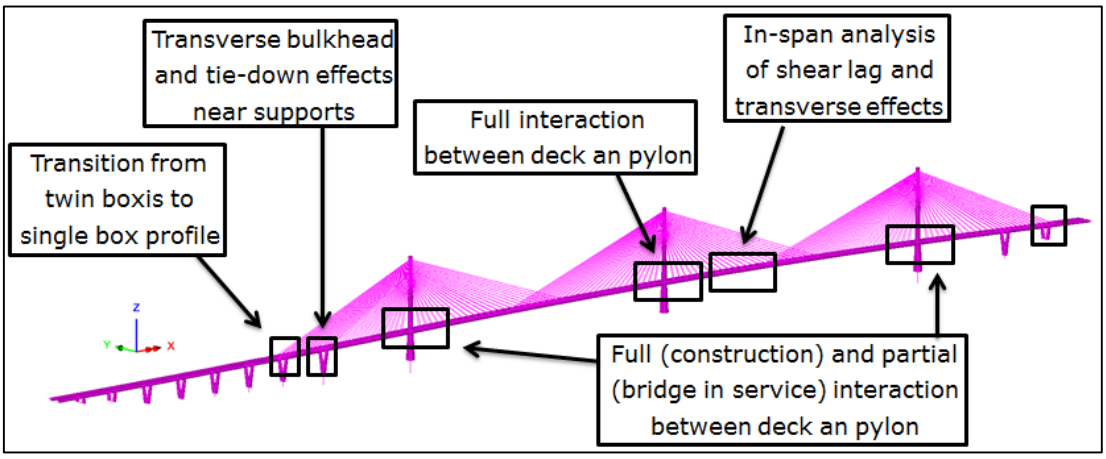

Figure 2.18. Overall structural model *(Kærn, et al., 2017)*

For the design of all three towers, special attention had to be paid to the construction conditions as the construction stages corresponding to the maximum free deck cantilevers led to greater stresses than in the final state.

Figure 2.19. CT with maximum deck cantilever *(Romberg, et al., 2018)*

Structural and main design features

The towers cross section is a box shaped reinforced concrete section with outer dimensions equals for every tower. In longitudinal direction, the width is 14 m at the base, tapering to 10 m at deck level and 7,5 m at the top. In transverse direction, it is 16 m at the base, 8 m at deck level and 5 m at the top. The concrete used is a C55/67 grade concrete. The main differences between the CT and FTs is in wall thickness, since CT required thicker walls to resist to the higher bending moments, achieved during free cantilevering. Wall thicknesses vary from 1,5 m to 2,4 m below the deck and from 1,5 m to 0,85 m above the deck. All towers have 400mm×400mm recess at each of their four corners to prevent vortex shredding.

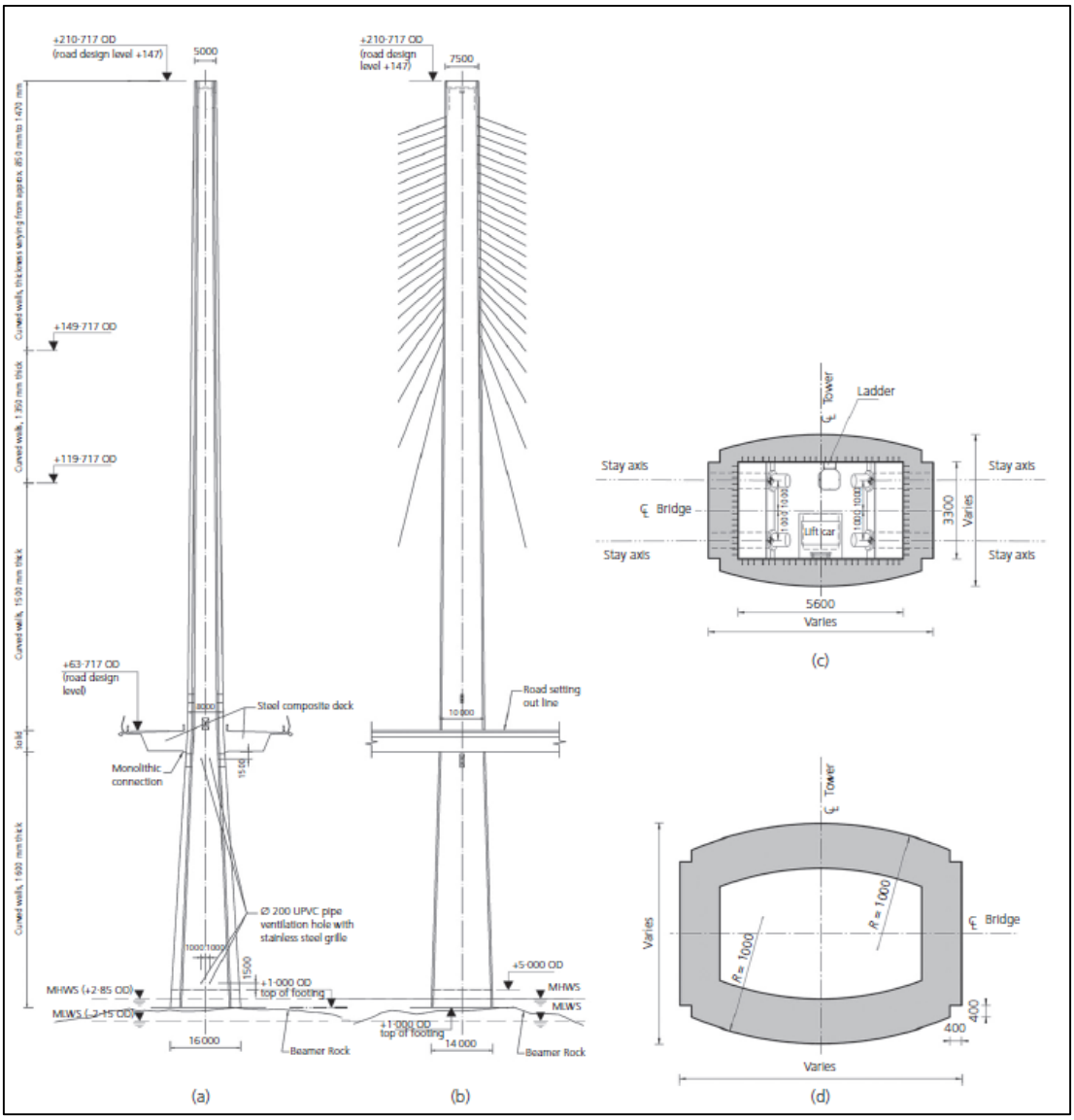

Figure 2.20. CT elevations and sections: (a) front elevation; (b) side elevation; (c) section at tower head (d) typical section *(Romberg, et al., 2018)*

At the base, temporary tie-down cables, anchored in a 6 m high solid mass concrete block, were required to reduce the moments in the deck construction stages when unbalanced configurations were to be experienced. This arrangement caused the bending stresses in the tower to remain at a level that prevented the concrete from cracking even with a maximum cantilever arm. Nevertheless, the tower tips deflected by approximately 1·50 m and the superstructure cantilever by about 3,50 m when lifting the last segment on the CT.

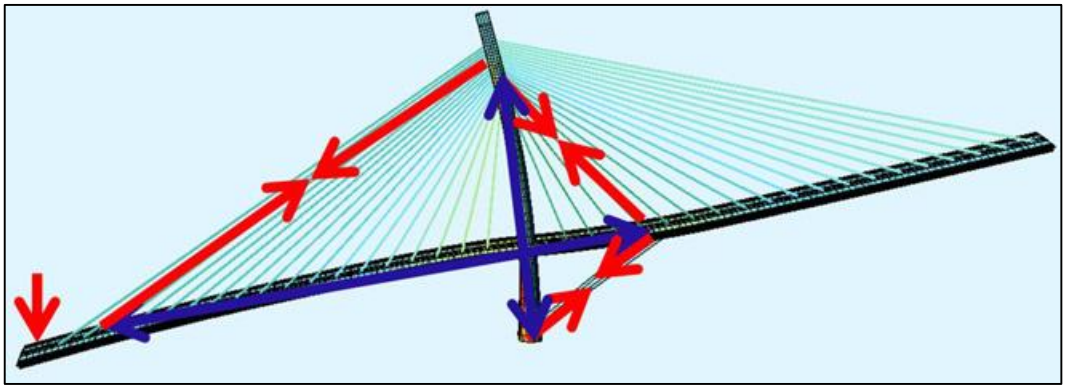

Figure 2.21. Force flow for unbalanced cantilevering configuration *(Romberg, et al., 2018)*

The monolithic connection between the deck and the CT had to be designed for large bending moments. At the ultimate limit state (ULS), the 'power joint' has to resist to: a bending moment of 1430 MN/m from the deck into the tower, a deck torsion of 1000 MN/m and a transverse bending of 450 MN/m (Romberg, et al., 2018). The monolithic connection is achieved through concrete on the bottom flange of the steel deck and post tensioned reinforcement running in both the longitudinal and transverse directions through the tower.

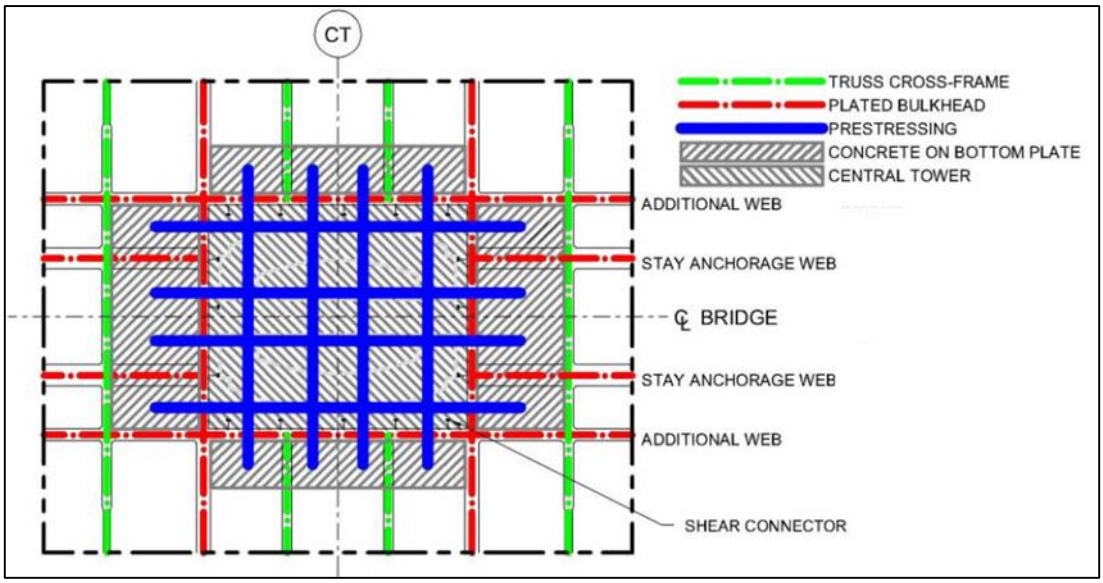

Figure 2.22. Plan view of the monolithic connection between deck and CT *(Kærn, et al., 2017)*

The function of the transverse plated bulkheads is to transfer the vertical forces from the webs to the CT. The shear connections between the bulkheads and additional webs are all welded to allow shear forces to be transferred from the steel deck to the concrete tower (Kærn, et al., 2017).

As mentioned before, the FTs provided longitudinal and torsional restraint only during the construction phases, while deck is permanently fixed in the transverse direction there. Both temporary and permanent supports are illustrated in ***Figure 2.22.***

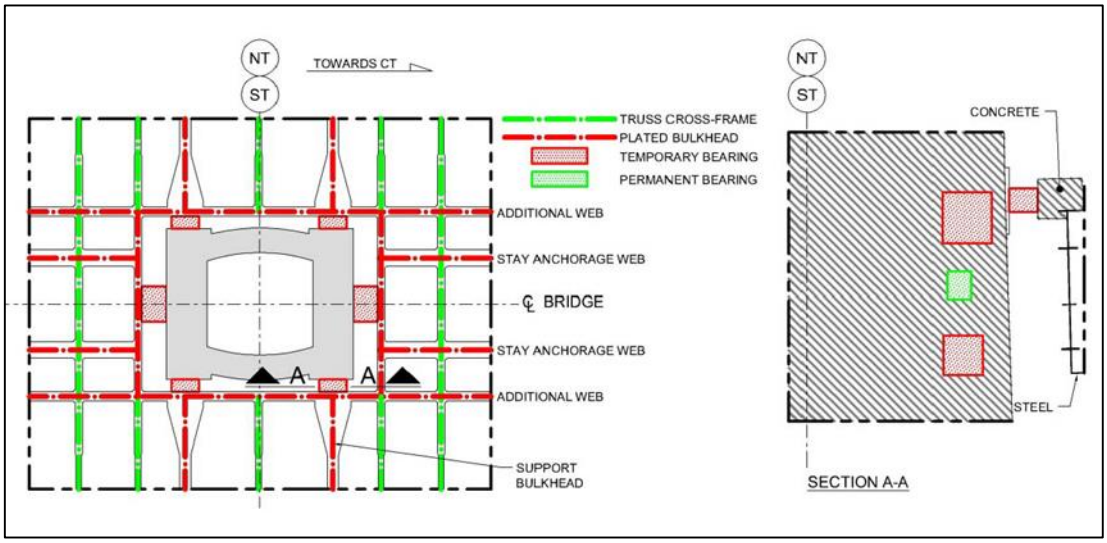

Figure 2.23. Plan view of permanent and temporary supports around FTs *(Kærn, et al., 2017)*

Four temporary bearings are provided in the transverse direction, two each side. In the longitudinal direction, one bearing a side is provided. The only permanent bearing is

located eccentrically on the side closest to the CT; this provides transverse restraint during the operational phase of the bridge.

The towers have various sensors installed to monitor the structure. These sensors comprise: cast-in strain gauges (static), corrosion sensors, temperature (concrete and air) monitors, post-fixed strain gauges (dynamic), tiltmeters, accelerometers, global positioning system and anemometers.

Construction

Work began first on the CT in July 2013, followed in the autumn by the NT and finally, at the end of the year, by the ST (Watt, 2017).

Towers were built in 4 m high sections, called "lifts", creating a hollow ring capable of bearing the next lift above. In total, each tower had 54 lifts. Towers construction was a rapid process and used bespoke fabricated self-climbing formworks. Jump-form construction was used instead of slip form due to the changing profile of the towers, and it helped construction, since workers could operate also in wind speeds up to 30 m/s. The birdcage consisted of four levels each used for different purposes during the tower construction. The top level ("upper frame") was used for storage and as access to install reinforcement. Below this is the "mid frame" was used for preparing shuttering and finishing of the stripped pour. Next is the "jacking frame" which provided guide rollers and attachment points for the jacks. Finally, at the lowest level of the frame there is the "trailing deck" which was used for any concrete finishing works (Romberg, et al., 2018).

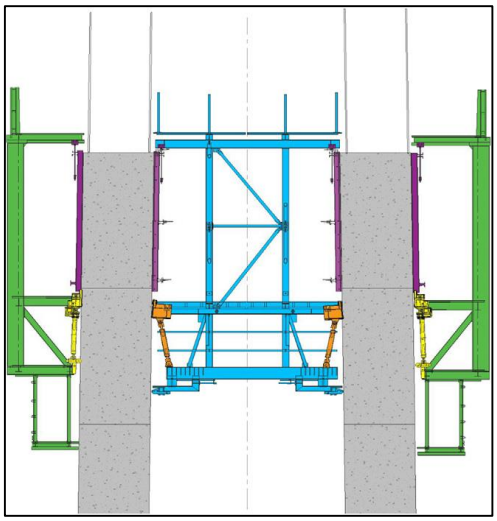

Figure 2.24. Climbing formwork scheme *(Romberg, et al., 2018)*

All the construction materials had to be delivered by barge and lifted into position by tower crane. Thus if wind speed was too high construction could be held up. The concrete was pumped using a pump on the tower crane platform. Once the concrete in each lift had hardened enough to support itself, generally 36 hour, the shutters could be jacked up in preparation for the next concrete pour. The cycle time for each lift, considering the moving and the setting up of the formwork, the rebar installation, the concrete pour and setting, was typically about 12 days.

Once the deck level (about +55 m OD) was reached, the deck starter segments were lifted into position by a floating crane and supported by a temporary falsework. Once above deck level self-climbing tower cranes were positioned so as to be unaffected by deck construction activities. These cranes were founded on structural steel piles driven to rock head. The cranes were also laterally supported with connections to the tower to ensure stability.

The steel anchorage boxes in the CT begin at +147 m OD and stop at +204 m OD. The anchorage boxes are located at similar heights on the flanking towers. The anchor boxes were installed in 5m segments, which are not connected to each other to ensure they do not act in a composite manner vertically. In addition to this each 5m section had come in two parts, due to the weight of the full section being too much for the crane to lift.

All three towers were completed on schedule within just a few weeks from each other. The first to top out in October 2015 was the NT, while the ST and the CT reached their top in the next two months respectively.

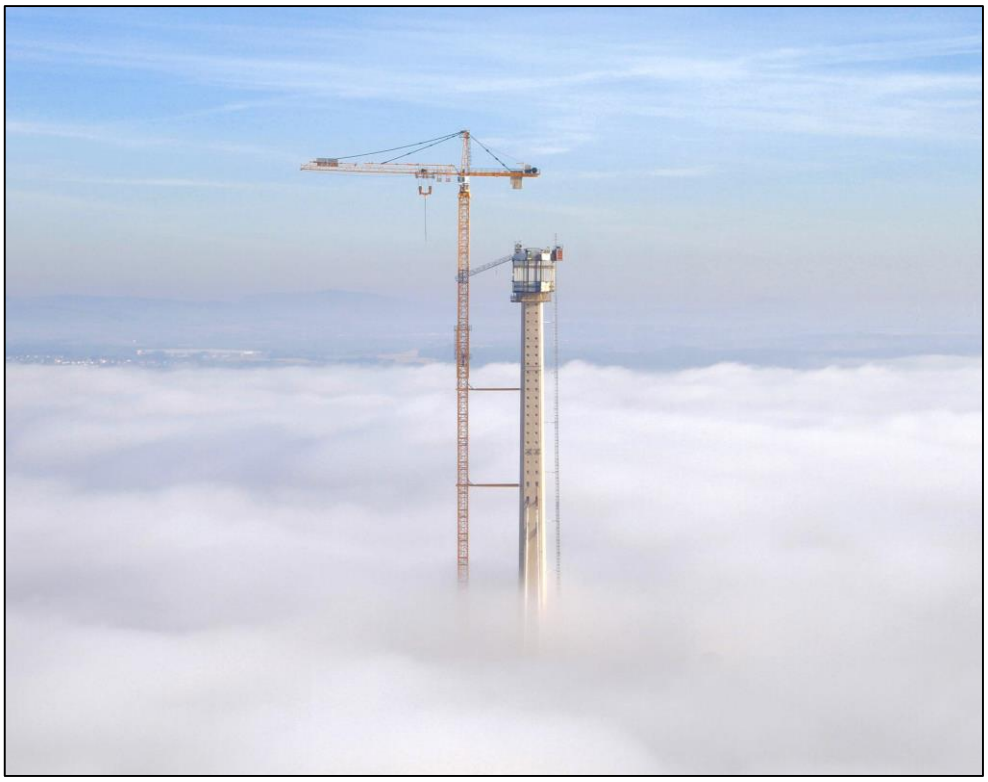

Figure 2.25. CT standing over the clouds from its 210 m height *(Broughton)*

2.3.3 Piers

A total amount of ten piers were required to support the two approach viaducts, eight of which are located on the south side (S1 to S8, see ***Figure 2.6***) and the other two sustaining the northern viaduct (N1 and N2).

Structural and main design features

A C50/60 graded concrete mix was used to build piers, resulting to be very resistant to chloride ingress. Stainless steel reinforcement was also used in the outer layers of the pier section which would be in the splash zone. Both these measures were taken to ensure service life in the aggressive saline environment.

The concrete piers are V-shaped to carry the twin-box sections of the approach viaduct decks. A cross tie is provided between the pier legs to restrain lateral movement from the bridge loading, but it was not used during the construction phase. The rectangular hollow section is formed from a series of walls, varying in thickness from 0,4 m to 1,2 m. The uppermost section under the bearing plinth is solid, approximately 3,5 m thick.

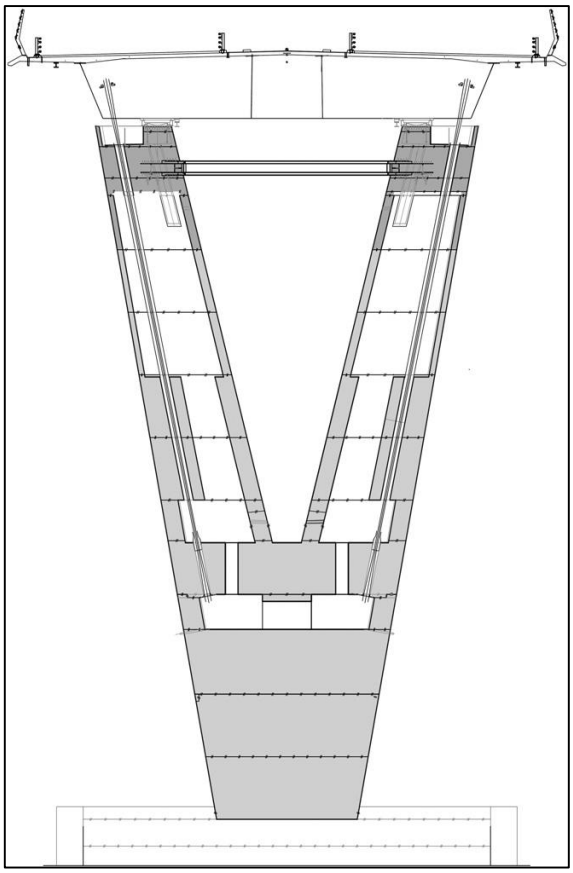

Figure 2.26. V-shaped piers layout *(Romberg, et al., 2018)*

Piers height ranges from 10,3 m (S8) to 49,4 m (S1). The piers in-service are designed to support spans varying from 87 m to 104 m. during the construction, they were designed as unrestrained at the top and with several live loads acting on the legs. The pier did not perform in its final condition until the steel cross-tie connecting the legs was installed. It helps to minimise forces in the legs by restraining lateral movement caused by bridge loading on the top.

Ship impact force was a governing load case for the design of the piers. Depending to the proximity to the main navigational channel, the required ultimate resistance of the piers was calculated between 10 and 75 MN. As a consequence, piers were designed to be fully functional with a section loss due to the impact. Another important load case considered for piers design, especially for pier N2, was the accidental exceeding of bearing friction (between bearing pads) during approach viaducts launching over the piers. Therefore, careful monitoring of the pier head deflections during the launching event was undertaken to ensure that the design friction was not exceeded and that significant cracking did not occur (Romberg, et al., 2018).

Construction

Adjustable sliding formworks were also used for piers construction, as legs taper with the height.

The bearings are designed to take vertical ULS loading varying from 27 MN to 96 MN and horizontal loads up to 13 MN. So, a 2,15x2 m plinth was required, for instance, on pier S1. Moreover, as bearings had to allow large displacement ranges (up to 2,4 m at ULS at pier S8), a baseplate with a series of cast-in studs in addition to holding-down anchors was required. The installation of these resulted to be a challenging operation, since the superstructure box was already in place, temporarily supported on jacks.

Figure 2.27. South Approach viaduct being launched on South Piers *(Transport Scotland, 2014)*

2.3.4 Abutments

The final components of the substructure are the abutments, two-storey reinforced concrete structures set into the sloping ground at the start of the approach viaducts. As well as providing vertical and lateral support for the bridge, they act as retaining walls, they carry bearings and movement joints, allowing the bridge to expand and contract

under temperature, wind and traffic loads. They also contain maintenance equipment, offices and stores, providing an internal access to the inside of the road deck.

Load from the RC base is transferred to mass concrete fill cast onto rock. The retaining walls have back-of-wall drainage and low level ingress of water is resisted by a 1,4 m thick base slab.

Construction

The two abutments were built in two phases to suit the construction method of the approach viaducts. The first phase provided the anchorage for jacking equipment used to pull the deck from the prefabrication area behind the abutment onto the supporting piers. The second phase consisted in closing the structure around the ends of the twin decks (Romberg, et al., 2018)

In each abutment there are two pedestals supporting the ends of the deck. In order to allow the launching operations without stopping other works, it was needed to cast the perimeter walls as high as possible, so the west and east walls were constructed to their full height since the beginning.

2.3.5 Bridge deck

The 2,7 km long road deck is configured as a three-corridor arrangement with the towers e stay-cables in the middle area. It carries two general lanes in each directions and two hard shoulders, useful to prevent traffic congestion due to maintenance work, breakdowns or incidents and to accommodate any public transport displaced from the FRB in case of high winds. The surface is completely smooth with no expansion joints along the way, providing certainly a more comfortable driving experience but also less joints to be inspected and maintained (there are expansion joints only at both the ends of the two carriageways).

As already mentioned, the deck is vertically supported by stay cables, piers and abutments, while it is totally fixed to the CT, transversally at the FTs, being free to move longitudinally.

The cable-stayed part of the deck consists of 122 composite segments, typically 16,2 m long, 110 of which were “standard” segments, while the other 12 were used as “starter” sections, initially put in position around the three tower, “starting” the balanced cantilever

operation (Curran, et al., 2018). Each box section averagely weighed about 750 tonnes when lifted up into position at approximately 60 m above water level (Watt, 2017).

Structural and design features

The typical section of the cable-stayed deck is a three-cell composite cross section, 39,8 m wide and 4,8 m high. The concrete slab has a thickness of 250 mm and it cantilevers for 5 m on both sides of the section. It is transversally pre-stressed in order to overcome the tensile stresses due to the suspension of the deck in the central zone, where the cables are located. This solution also helps torsional rigidity, which would come out dramatically reduced in case of slab cracking. The steel box is stiffened with longitudinal trapezoidal stiffeners and with transverse frames positioned every 4.05 m. The transverse frames carry the loads from the two external inclined webs to the inner webs which are supported by the cables. The stay-cable anchorages for CT are positioned on the inner side of the inner webs, while those the FTs are located on the outer side of the webs to allow the stays to overlap at the centre of the main spans (Curran, et al., 2018).

The two approach viaducts deck is instead a twin separate box sections, built in order to maintain road continuity.

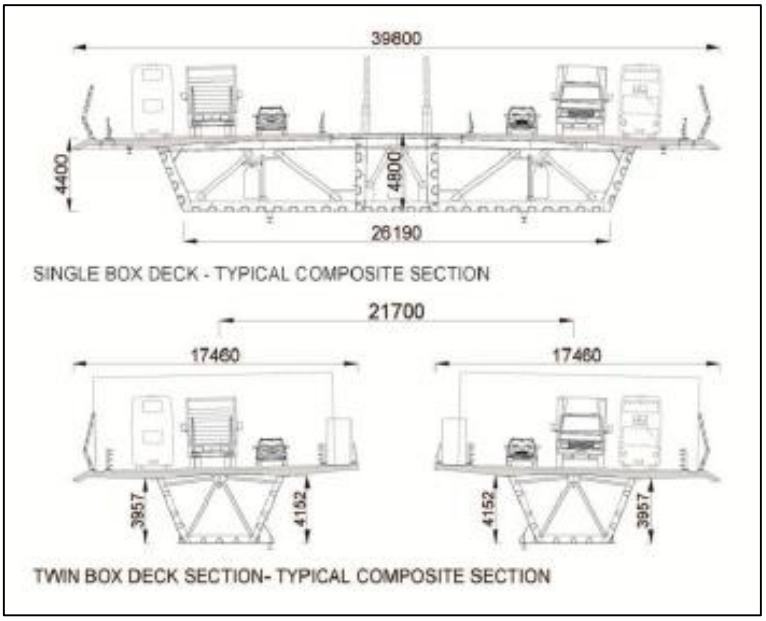

Figure 2.28. Bridge deck typical sections: single box (above) and twin box (below) composite *(Curran, et al., 2018)*

Construction

All 122 steel deck sections were fabricated the ZPMC steel fabrication plant, near Shanghai in China, and then shipped to the Port of Rosyth, 3 km far from the bridge site.

Upon completion and before leaving the fabrication centre, every deck segment was trial fitted to its neighbours to ensure that no problem would be encountered during the assembly phases on the site (Watt, 2017). After a six weeks sailing journey, the steel boxes arrived at Rosyth Docks and then were transferred into sheds for fixing of rebar, post-tensioning ducts and concreting of the deck slab. Once the concrete had reached adequate strength, the slab was post-tensioned using lateral steel cables, firstly at 30% of the post-tensioning force and, later, up to the 100% (Curran, et al., 2018). At that moment, the average weight of the sections was increased to 750 tonnes, while initially the only steel boxes weighed about 250 tonnes.

The installation of the deck segments resulted to be a delicate lifting operation, given the strong winds and the bad weather conditions in that area. Before the balance cantilevering phases could take place, the 12 starter segments had to be put in position around the three towers.

During the summer of 2014, towers height had reached above road deck level. This triggered the start of work to prepare for the installation of the first deck sections. So, a huge steel temporary falsework (7200 tonnes in total) was installed on each tower. Each tower falsework consisted of two triangular trestles 60 m high, fixed to both sides of the tower from the foundation to deck level, and of two platforms, placed on the trestles, which had to be the support basement for the 4 starter segments. Between September and October 2014, the starter steel boxes were lifted into position, without the concrete slab to save weight. At the Central Tower the steel segments were monolithically connected to the pylon and pre-stressed both longitudinally and transversally. Then, once welded and bolted together, the reinforced concrete slab was cast in situ and pre-stressed. When the towers had reached the height to engage the first stay cables, they were attached to the sections and tensioned. The first stay cables carried deck weight for the first time in August 2015 (Watt, 2017). After the starter segments were suspended from the stay cables, the erection travellers, hydraulically powered cranes weighing typically 250 tonnes, were placed at either end of the emerging road deck cantilevers on each tower.

Figure 2.29. Deck erection system *(Broughton)*

They used a strand jack system to lift all the following deck sections from barges on the sea (Watt, 2017).

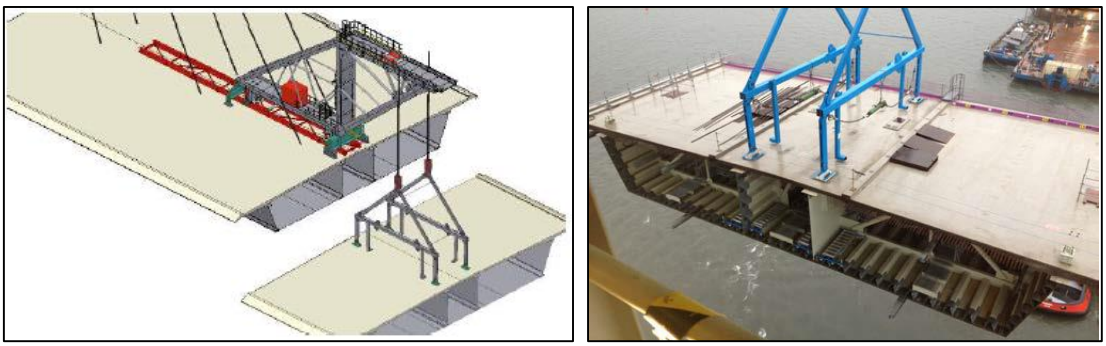

Figure 2.30. Scheme of the erection traveller crane *(Lamb, 2018) (Kærn, et al., 2017)*

By September 2015, the remaining 110 deck sections were ready to be lifted up and placed in their permanent position on the sides of each tower. The erection of the deck lasted until February 2017, following a balanced cantilever construction method.

Once ready, sections were loaded two by two onto barges capable of carrying them (about 1500 tonnes) and transported towards the towers. Then barges were anchored and the cranes lifted up the sections until deck level (up to 60 m above sea level), in an operation that lasted about 4 hours. Because of the different deformation of the already installed

segment and of the lifted one, the two segments were aligned with pre-attached alignment devices.

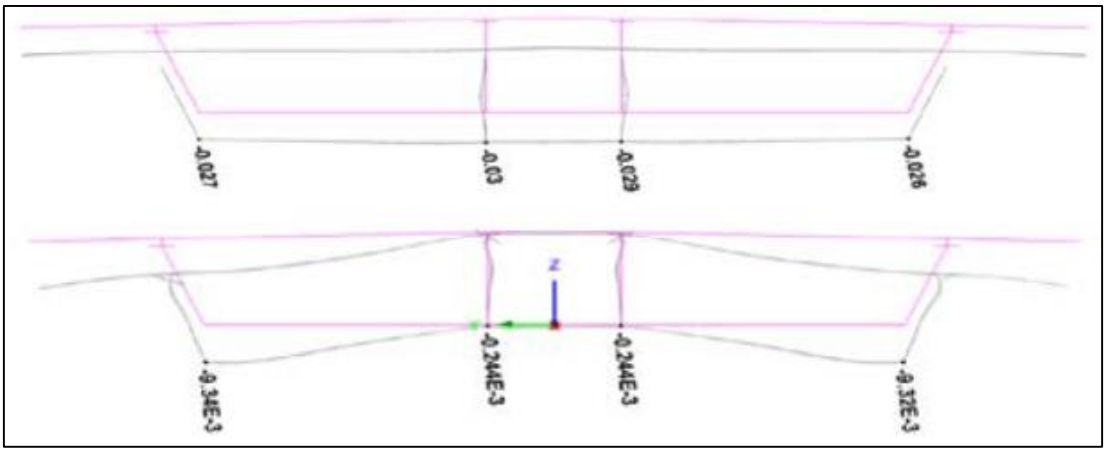

Figure 2.31. Deck deformations: already positioned (above) and lifted (below) segments *(Kærn, et al., 2017)*

Special attention was given to the sequence and extension of the welding and bolting during this assembly and during stressing of the cables in order to control and minimize any locked in stresses in the steel box (Kærn, et al., 2017).

In this way, deck sections were installed one at a time on alternate sides of each tower creating a balance in the growing cantilevers on either side. Obviously, as one deck section was installed on one side, the cantilever structure would deflect under the increased weight on that side, before equilibrium being restored with the next lift on the opposite side. So temporary tie-down cables were installed in order to reduce this effects and the strain on the base of the towers.

In October 2016, the free-standing Central Tower span reached the maximum length of 644 m (composed of 36 separate steel sections), which was recognised as the longest, free-standing, balanced cantilever structure ever built in the world.

Figure 2.32. The CT free-standing balanced cantilever before the closure *(Martin, et al., 2017)*

A total of four closures had to be made: the two gaps in the main spans and the other two ones with the launched approach viaducts. The closure sections between the CT and the FTs measured a length of 6,1 m and, to maximize the available gap, the FTs deck was pushed back 300 mm using hydraulic jacks and allowing the positioning of the closure section.

To install the superstructure across Piers S1 and S2 the erection traveller firstly lifted segments and positioned them on a supporting structure located on the pier head. These segments could then be moved in the longitudinal direction on the support structure to leave the necessary space for the closure segment. After the closure segment was connected to the cantilever arm in the same way as a typical segment, the pier segment could then be moved into its final position on the pier head and then connected to the closure segment (Curran, et al., 2018).

Figure 2.33. Closure segment on pier S1 *(Curran, et al., 2018)*

2.3.6 Stay-cables

The deck is vertically supported by a total number of 144 pairs of stays, the longest of which is 420 m long. Every cable is composed of a number of strands (between 45 and 109) protected by a High Density Polyethylene (HPDE) pipe each. The strands have a cross section area of 150 mm^2 and a minimum guaranteed breaking stress of 1860 MPa (Curran, et al., 2018). The design service life is 60 years for the stays, and strands were required to be replaceable individually.

The stay cable system used for the Queensferry Crossing is built up of individually anchored parallel strands encapsulated in a continuous pipe system offering a multi-barrier protection system. The protection system is achieved in the free length of the cable by individually covered waxed galvanized strands within the protective HDPE outer stay pipe. The protection is maintained in the anchorage assembly by a flexible injected filler

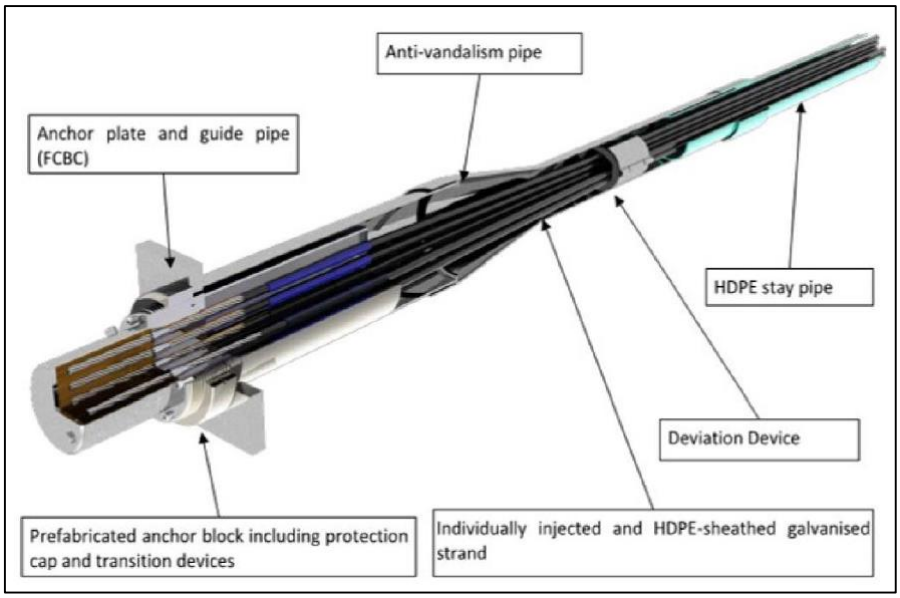

Figure 2.34. Stay-cable arrangement scheme *(Curran, et al., 2018)*

Each of the three towers has 96 cable stays. The cables are connected to the tower using steel anchorage boxes. Tower anchorages are active allowing tensioning adjustment of the cable, while anchorages in the steel boxes of the deck are fixed

The cable stays overlap at the centre of the main spans, resulting in structurally helping (see ***2.2***) as well as aesthetically pleasing. One of the challenges posed by the use of the overlapping cables at the centres of the main spans was the connections to the single box. To allow for the overlapping cable arrangement the cables from the CT are anchored on the inside of the stay anchorage web. The cables from the NT and ST are anchored on the outside of the stay cable web.

In addition, this innovative feature had to consider the different "structural phases" of the deck. Actually, the ten central segments in the main spans are supported, in the permanent state, both by the stay cables installed during the free-cantilevering erection and also by the overlapping stay cables coming from the other tower and installed after the main span closures. Therefore, during the construction stage the five longest cables of a cantilever were stressed to a higher force then that required for the final condition, since they had to support deck segments weight without the "help" of the overlapping cables. Only once that these were installed, they could effectively be de-tensioned.

Aerodynamic forces, such as vibration or vortex, acting on the stay cables are generally induced by dynamic forces like traffic. On the Queensferry Crossing these effects are

limited by using helical ribs on the HDPE pipes and applying friction dampers as additional damping devices.

Figure 2.35. Friction dampers *(Curran, et al., 2018)*

These devices are intended to dissipate energy through the friction generated between two friction partners. The force acting on the damper has firstly to exceed the static friction between the two friction partners before they start moving. The damping characteristics of the dampers can be adjusted and they are initially set in order to obtain no movement in the damper arising from the non-critical continuous vibration of the cable with the small displacements that traffic and other effects cause. However, once the cable vibration has reached a level that is critical for the cable to which it has been tuned the friction damper achieves its maximum performance almost immediately. In case of cables displacements exceeding service limit state, a mechanical blocker transfers the force to the guide pipe connected to the deck slab.

2.3.7 Approach viaducts

The two viaducts complete the deck structure spanning from the approach roads on land to the cable-stayed bridge. They are supported from beneath by the piers and their construction methods are quite different from those used for the cable-stayed deck. Indeed, viaducts are situated in shallow water, inaccessible by barge. Therefore, it was

impossible to lift separate sections from barges, as well as done for the bridge deck. A different solution was adopted and it required the viaducts to be pre-assembled on land and then to be launched out incrementally over the supporting piers (Watt, 2017).

Construction

The South Approach Viaduct (SAV) consisted of two separate 543 m long stretches of steel box girders, trapezoidal in cross-section, each divided into 19 sections. The 28,5 m long sections were fabricated in Darlington by Cleveland Bridge UK. Once arrived on site, the sections were welded and bolted together to create two separate box girders with the aid of an overhead gantry crane. When the first two sections were assembled together, they were ready to be launched out towards the piers. The launching activity was helped also by the use of two *king posts*, installed 85 m back from the leading edge, which prevented girders to deflect and lifted their nose up and over the piers. In this way, the front edge was able to meet the guides positioned on the top of each pier to ensure that the viaduct sections were in the right position during the launch. Powerful strand jacks attached to the abutment pulled out the girders alternatively.

Figure 2.36. The incremental launching phase of the South Approach Viaduct *(Carter, et al., 2017)*

The first launch took place in December 2013 and then six launches for each length were needed, taking 18 months (until June 2015) to complete the viaduct (Watt, 2017). At the end of this process, the reinforced concrete deck slab was cast in-situ. This took the average weight of each section up to 600 tonnes.

Similarly, to the SAV, the North Approach Viaduct (NAV) steel sections are pre-assembled in a temporary welding shed. In this case a single 221 m long box girder, weighing 6000 tonnes, was constructed. The NAV comprised a length of two 76 m long separate box girders (8 twin box sections) and a remaining 145 m long single box stretch (12 sections). The single box sections became an integrated part of the cable-stayed bridge deck once in position, but they were unable to be lifted as the other deck sections. The launching process was again aided by a king post.

Figure 2.37. North Approach Viaduct launch *(Lamb, 2018)*

Before the launch (taken place in February 2016), 40 m of reinforced concrete deck was cast on top of the twin-box sections (at the back) as a counterweight to provide balance during the process. The strand jack system pulled out the NAV up to a point just beyond the first pier N2. Then, as the leading edge had to be lifted up of about 2 m, in order not to strike the following pier N1, a difficult rotating operation was carried out. The trailing edge was attached to skid shoes that, as the structure continued its steady journey, travelled down two temporary ramp walls, located at the north abutment, creating a pivot on pier N2. This allowed the nose to be lifted 2 m upwards and to be positioned at the correct angle to clear the top of pier N1.

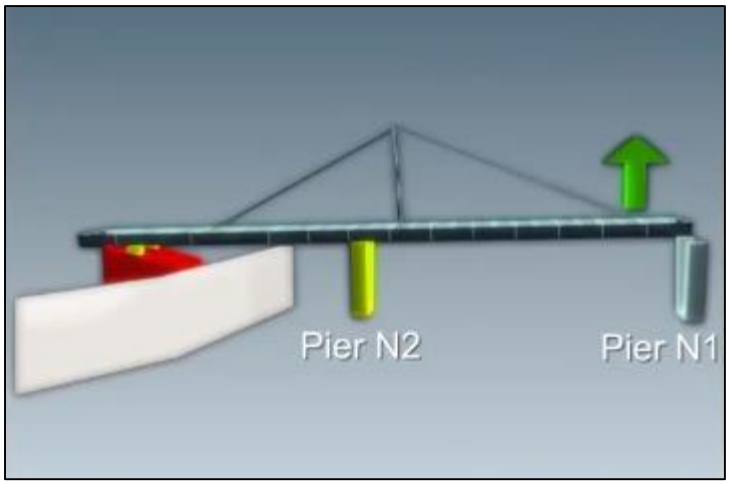

Figure 2.38. Scheme of the pivoting operation *(Transport Scotland, 2018)*

The NAV construction work totally took 15 months, while the launching operation lasted 4 weeks.

3. SHM deployment on the Queensferry Crossing

The Queensferry Crossing is one of the most advanced infrastructure in the world because of not only the innovative construction and design technique adopted, but also due to the extensive use of SHM systems, which allow the bridge to be kept safe and lifelong monitored. The system has been designed to enable an effective maintenance planning, rapid response to incidents and early intervention to keep maintenance costs sustainable. It comprises approximately 2000 sensors that measure in real-time both environmental actions and bridge response (Carter, et al., 2017).

3.1 How it works

The system designed by *Amey* includes four subsequent steps to follow, consisting in:

1. *Collect Data*: collecting data automatically by remote sensors present on the structure, relating with the effects (wind, vehicle, temperature, etc.) on the bridge and its response;
2. *Build Understanding*: analysing, integrating and visualising multiple big data sets, investigate correlations between variables, evaluating historic patterns, trends and events, understanding relationships and behaviours;
3. *Monitor & Predict*: real time monitoring and prediction of future behaviour, threshold levels establishment and automated alerts and reports;
4. *Decide*: confirming safety or responding to alerts deciding intervention methods and priorities according to the budget defined.

The model is implemented in two bespoke integrated systems, called *Mercury*, which is the data analytics platform, and *Pearl*, which is the bridge information and condition database.

Mercury elaborates the SHM sensor data with the structural effects and capacities in order to understand and interpret data and bridge behaviour, and actively monitor with intelligent alerts and lifecycle records. The *Pearl* system collects bridge information and condition creating a Cloud Database and thus providing automated inspection and bridge condition reports and maintenance budgets.

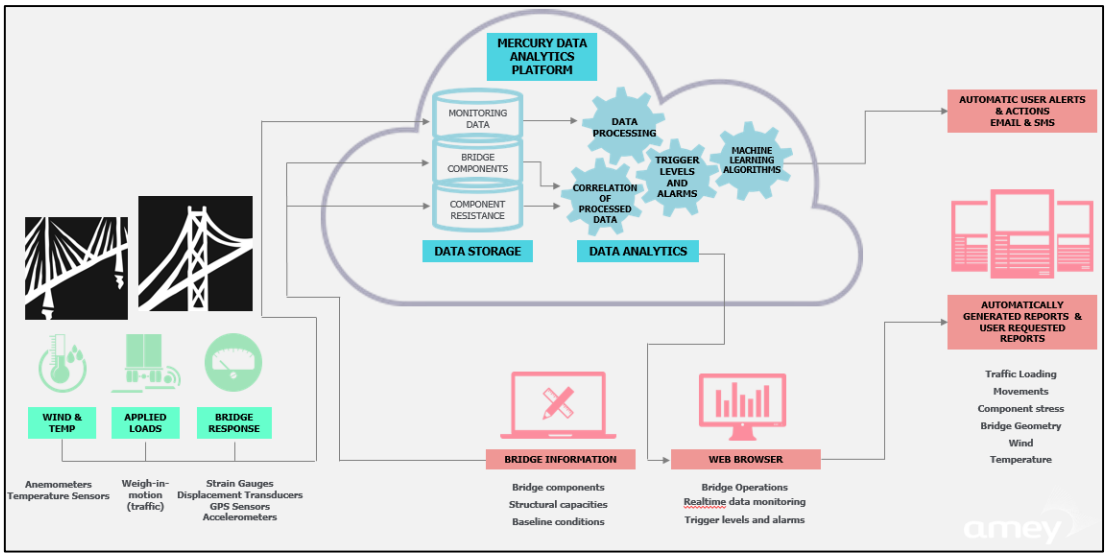

Figure 3.1 SHM system process *(Angus, 2018)*

3.2 Sensor types and arrangement

The SHM deployment on the Queensferry Crossing is extensive and makes use of a large variety of sensors, as Table 1 shows below:

SHM sensor type	Number of sensors
Accelerometers	102
Air temperature sensors	13
Anemometer	11
Asphalt temperature sensors	40
Barometers	2
Bearing gauges	16
Concrete deck temperature sensors	70
Concrete tower temperature sensors	46
Corrosion sensors	360
Displacement transducers	32
Dynamic weigh-in-motion sensors	96
GPS location	21
Rainfall gauges	2
Stay cable temperature sensors	96
Strain gauges	887
Steel surface temperature sensors	158
Tiltmeters	48

Table 3.1.SHM sensor types and relative quantities on the Queensferry Crossing *(Kitching, 2017)*

In the following, a selection of sensors will be described, providing their functions and some drawings and showing their locations on the structure. A detailed study on the strain gauges will be provided, since strains are the principal objects of this thesis.

3.2.1 Environmental Sensors

This category includes temperature sensors (air, asphalt, concrete deck, concrete tower, stay-cables, steel surfaces), barometers, anemometers and rainfall gauges.

Temperature sensors

As stated in Table 1, this kind of sensors are used to monitor the temperature of the asphalt, concrete road deck, stay cables, steel surface, concrete tower and air.

Temperature sensors record the temperature of the stated element in their description. One of the key reasons to record the temperature is that it effects the material properties of bridge elements. This can result in changes in structural behaviour of elements of the bridge. The data from these environmental sensors can be used to clean the data from the kinetic sensors, which measure the structural responses of the element in question. In particular, temperature is used to compensate the measured strains and to understand the thermal induced stresses on the structure.

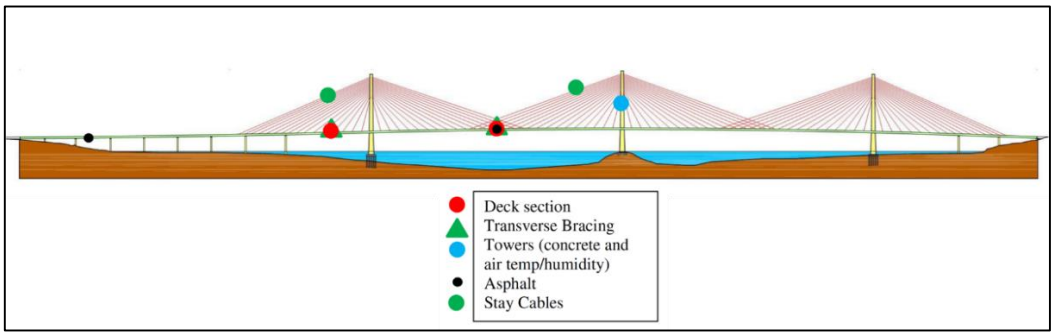

Figure 3.2. Temperature sesnsors arrangement on the Queensferry Crossing *(Angus, 2018)*

Figure 3.3. Some photos of the Temperature Measurement Units (TMUs) located on the asphalt, concrete deck, steel structure and stay cable *(Angus, 2018)*

Wind and Weather sensors

Two barometers, eleven anemometers and two rainfall gauges belong to this category of sensors. The first ones measure air pressure and they are located at mid-span of the two main spans attached to the windshields, as well as the rainfall gauges, which, on the contrary, monitor rainfall rate and total rainfall.

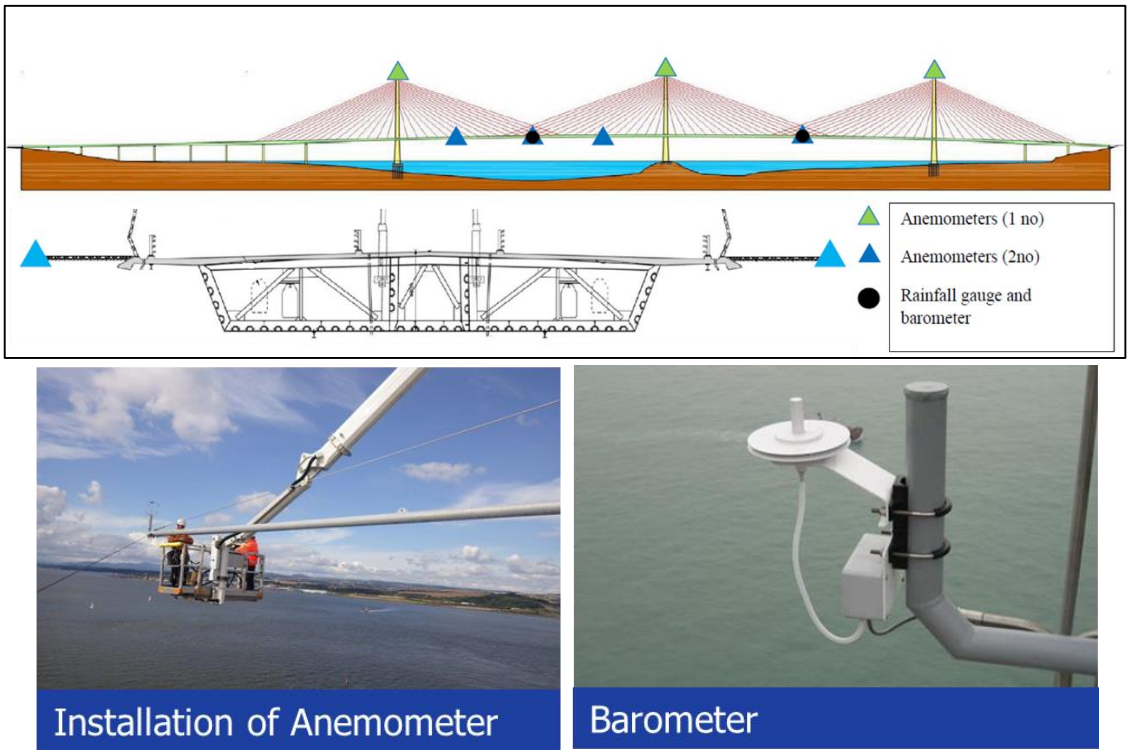

Figure 3.4. Wind and Weather monitoring sensors on the Queensferry Crossing *(Angus, 2018)*

These sensors help to follow the development of storms, or to better understand the interaction between the structure and the wind, also in presence of vehicles. As high wind speed can result in the bridge being closed to high sided vehicles or in extreme conditions closed to all traffic. The windshields have greatly increased the protection for traffic on the bridge. However there is still a need to monitor wind speeds to ensure they are within acceptable ranges, if wind speed is above 70 mph bridge may have to be closed.

3.2.2 Corrosion Sensors

The corrosion sensor's purpose is to provide information which can be used to predict the time at which corrosion will begin in the reinforcement. This information can be used to adjust the predicted service life of the most exposed/at risk reinforced concrete bridge elements.

Corrosion ladders are the type of sensor that are used for this deployment. They consist of six steel rods and a temperature sensor, the rods are in a ladder arrangement. It should be noted the steel rods will be the same material as that used for the steel reinforcement. The ladder frame is made of two u shaped stainless steel bars, see ***Figure 3.5***, it should be noted that for areas of concrete with construction joints, larger anodes are used.

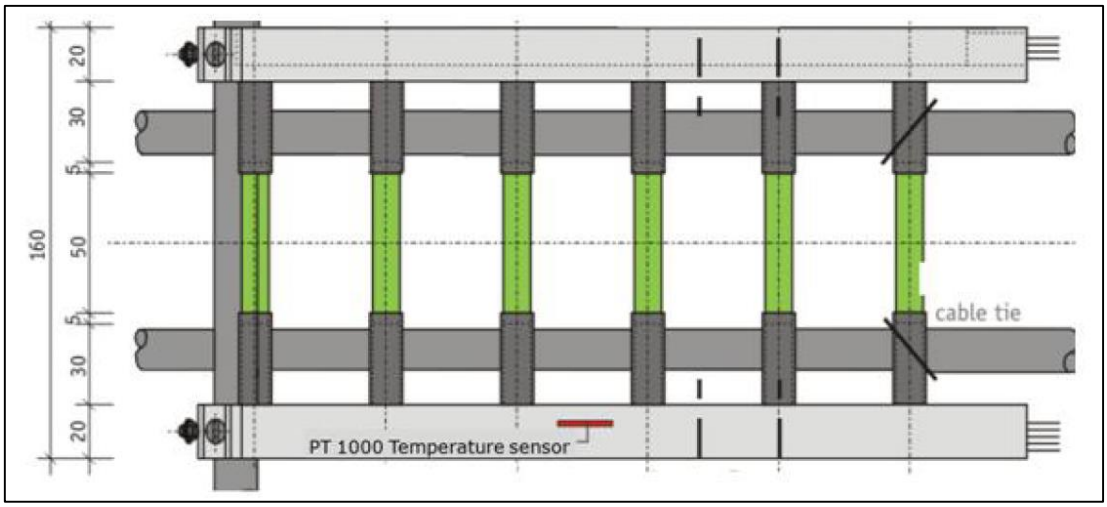

Figure 3.5. Principle arrangement drawing of the corrosion ladder sensor to be used on the Queensferry Crossing *(Ramboll, 2013)*

In addition to the ladder and anodes, there are several individual sensor parts, cathode bar, reference cell, reinforcement connection bracket and relative humidity sensors.

In the required positions, the corrosion ladder will be located so that the outer anode has 20mm of cover and the inner will have 80mm, the same as the reinforcement. The length

of time taken for each anode to corrode will be measured, this figure will be extrapolated to estimate the length of time for corrosion of the reinforcement to begin, for reinforcement with full cover.

The level of corrosion at each anode is determined by measurement of four parameters:

1. open circuit potential;
2. corrosion current;
3. resistivity;
4. linear polarisation resistance.

(Ramboll, 2013)

The corrosion ladders are located in all three towers and piers S1/N1. The sensors are located near the base of these elements as this is the area most at risk from corrosion, due to the seawater.

The Data Acquisition Units (DAU) that will be used are Corrosion Monitoring Data Loggers (CMDL). The corrosion ladders will be wired to their own individual cable box, these boxes will be connected to the CMDL, each pier and tower will have one CMDL. The CMDL will be able to carry out the simple measurements described previously and log them. The sampling rate at which these measurement are to be carried out at is still to be determined, this will occur during the testing phase (Ramboll, 2013).

3.2.3 Kinetic Sensors

This category includes all the other kinds of sensors present on the bridge whose measurements relate with the structural response and behaviour: Dynamic Weigh-in-Motion (DWIM), accelerometers, dynamic and static strain gauges, GPS receivers, tiltmeters, bearing gauges and displacement transducers.

Dynamic Weigh-In-Motion

The dynamic weigh-in-motion sensor consists of a bending plate type sensor, able to measure the whole tyre print length (250-400mm) on top of the sensor surface for real data weight. The DWIM sensors are used for traffic modelling and to draw trends of HGV loadings.

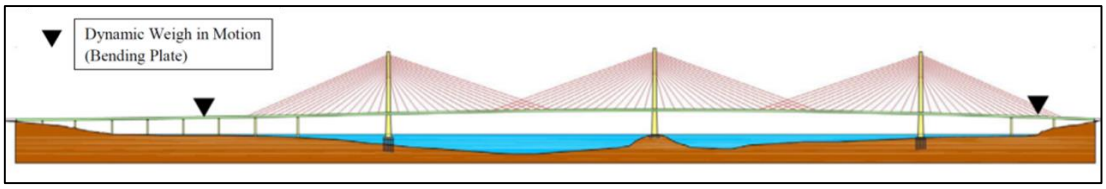

Figure 3.6. DWIM sensors location on the Queensferry Crossing *(Angus, 2018)*

For each of the traffic lanes and hard shoulders, the dynamic weigh-in-motion sensor consist of four bending plate sensors installed in line in two rows and with wheel detectors (induction loop for vehicle detectors) in between and low power recording electronics to obtain wheel load/unbalance data. The whole sensor is covered with a neoprene rubber film hot vulcanised on.

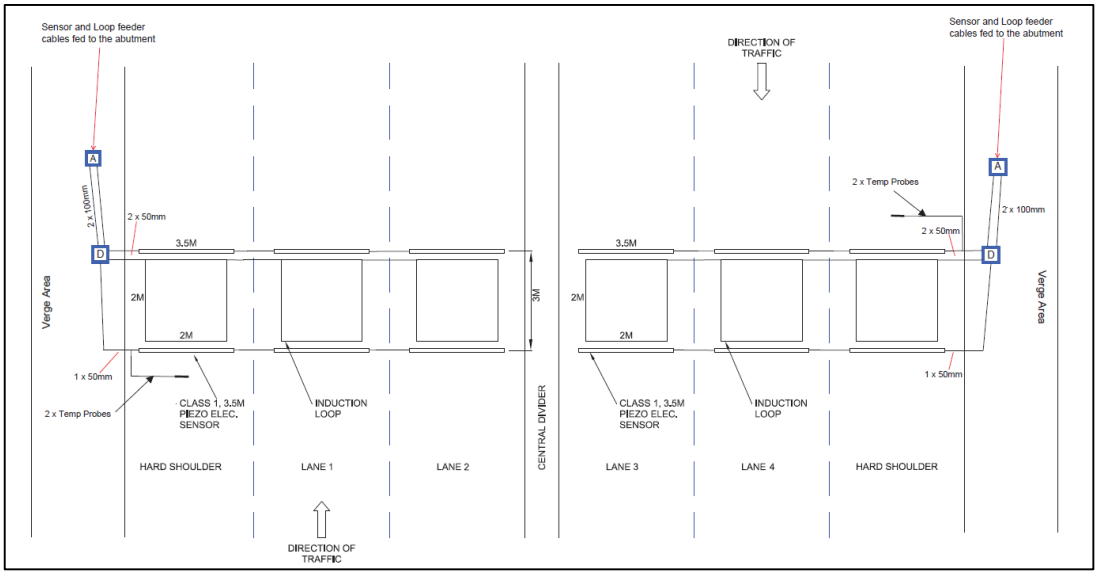

Figure 3.7. DWIM design (above) and realization (below) *(Angus, 2018)*

Accelerometers

There are 102 accelerometers deployed on the Queensferry Crossing. They are deployed: in the road deck, at the base of the piers, in the towers and on selected stay cables. Tri-axial servo-type accelerometers have been used on the structure, measuring accelerations in three orthogonal directions, X, parallel to the bridge alignment, Y, perpendicular to the bridge deck alignment in the horizontal plane, and Z, perpendicular to the horizontal plane formed by X and Y.

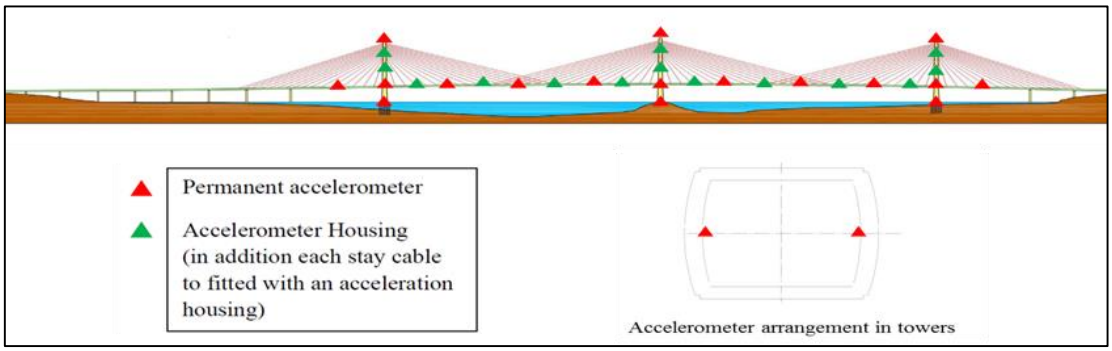

Figure 3.8. Accelerometers deployment on the Queensferry Crossing *(Angus, 2018)*

The data gathered from accelerometers can be processed to provide the dynamic behaviour of deck, towers and cables.

Figure 3.9. Some pictures of the accelerometers and their housing *(Angus, 2018)*

For each of the accelerometers, a robust protective casing has been provided to protect the instrument from sudden damage or from weather. The completed device are fixed on the bridge in a rigid manner so that the accelerometers and the bridge are in one absolute motion, and there is no relative motion between the bridge structure and the accelerometers.

GPS and Displacement Sensors

This kind of sensors are generally used to monitor bridge articulation and geometry, navigational clearances, and responses to the applied loads and extreme events. They are GPS systems, tiltmeters, bearing gauges and displacement transducers.

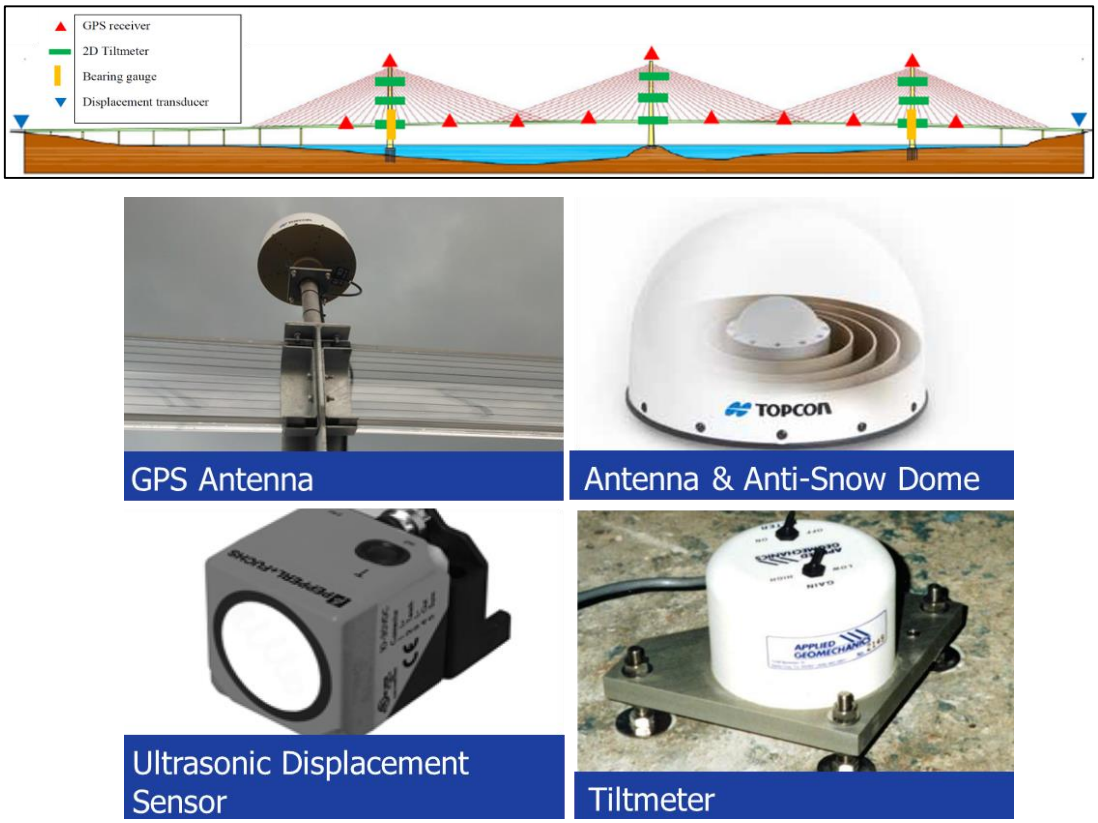

Figure 3.10. GPS and Displacement sensors and their arrangement on the Queensferry Crossing *(Angus, 2018)*

The field equipment of GPS installed at each of the base reference stations and rover stations basically consists of a GPS antenna, a GPS receiver and all necessary signal and power connecting cables. The GPS antennas of the rover stations are permanently installed at the top of the three towers and at required sections on both sides of the bridge deck, and securely fixed to brackets on the bridge structure, and equipped with permanent cabling to be connected to the GPS receivers. The GPS receivers of the GPS base

reference stations are housed in stainless steel cabinets, securely fixed inside the interior of building and accessible for inspection and maintenance. They shall be equipped with permanent signal and power cabling for displacement (in X, Y and Z directions, see *Accelerometers*) data transmission.

The bi-axial tiltmeters are installed along the height of the three towers for monitoring flexural deflection from the vertical alignments.

Displacement sensors are used to measure the displacement of key elements of the bridge. The displacement transducers are clustered in four deployments in four key sections of the bridge structure, in terms of movement. There are deployments at the expansion joints at both abutments and there are deployments at both flanking towers. The deployments in the flanking towers are next to the bearings. The displacement sensor deployment at the abutments are on each of the two single box viaduct sections, the deployment in one of these section at the North abutment is shown in ***Figure 3.10***.

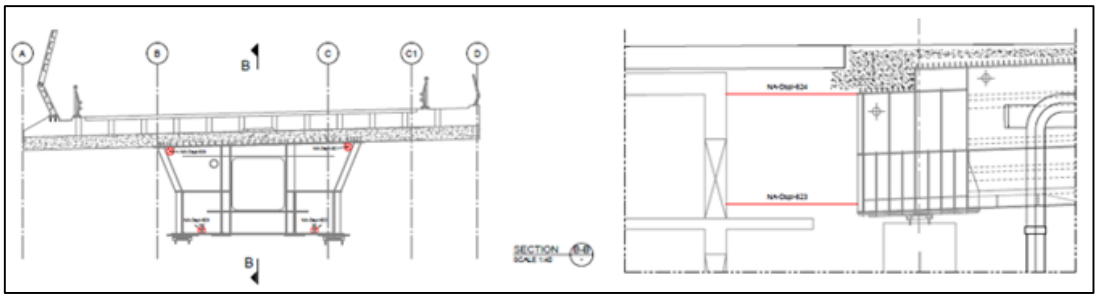

Figure 3.11. Section view of displacement sensors deployments at the North abutment expansion joint *(Ramboll f, 2015)*

These areas have been selected as the design of the structure dictates that movement will be allowed at these locations. These movements should however be closely monitored to ensure there are within expected ranges and there is no unexpected structural behaviour, which may indicate damage.

Strain gauges

Two types of strain gauges are employed on the Queensferry Crossing, static and dynamic strain gauges. The first ones measure the strain inside the structural concrete of towers, piers and road deck. The latter ones monitor the strain in the structural steel sections of the deck and in towers cables anchorages.

The strain measurement system has to be capable of processing the outputs from the gauges to provide the following information:

a) Stresses (principal and shear) on the monitored elements;
b) Global effects (forces and bending moments) derived from a);
c) Stresses due to thermal effects;
d) Correlation of extreme events with predicted design values;
e) Calibration of fatigue models.

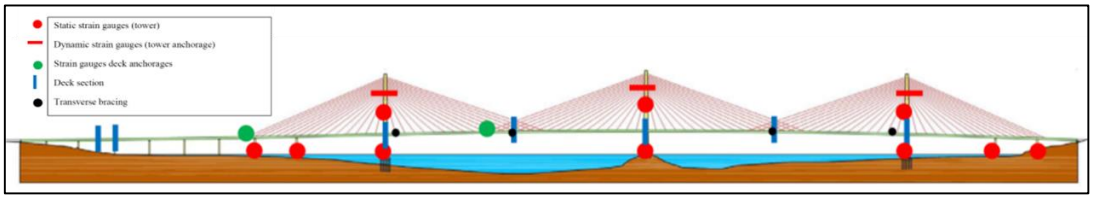

Figure 3.12. Static and Dynamic Strain-gauges location on the Queensferry Crossing *(Angus, 2018)*

The strain gauges can be used in two arrangements, single gauge and rosette according to what it is required to be measured. The difference between the two arrangements is that the rosette arrangement, used only in the road deck, can measure strain in different directions, whereas the single can only measure in one. The rosette arrangement achieves this functionality by using two or more single strain gauges orientated in different directions. The principle arrangement of the rosette static strain gauges for the road deck slab is shown in ***Figure 3.13***.

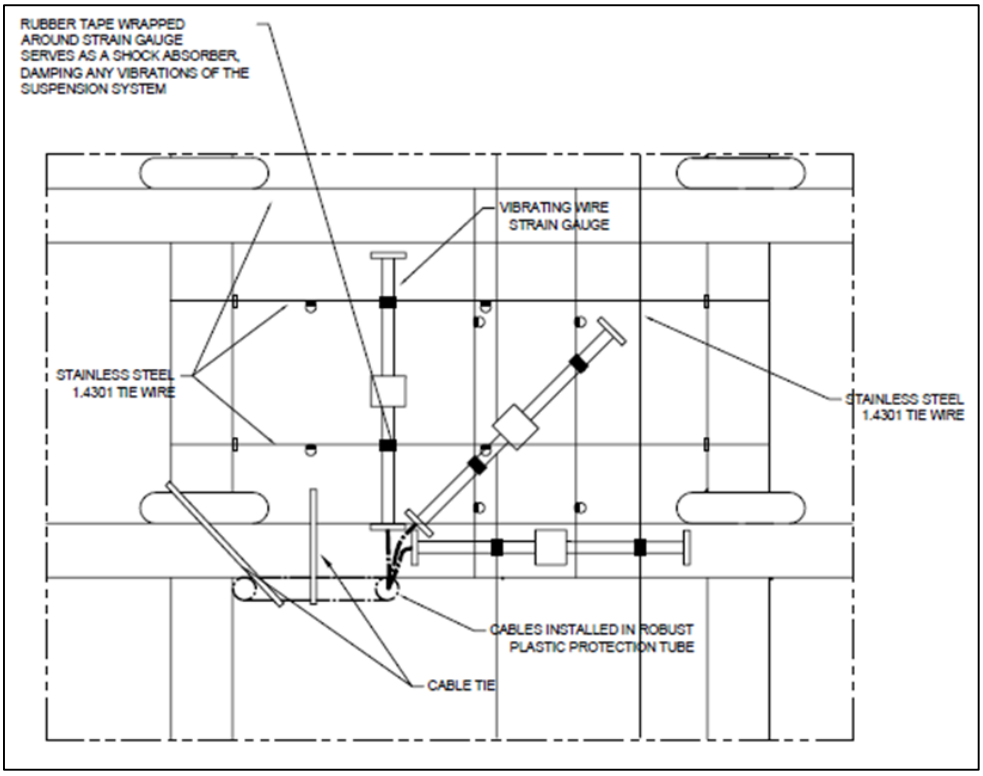

Figure 3.13. Principle arrangement of the rosette static strain used in the road deck slab *(Ramboll a, 2015)*

The single gauge arrangement used in the towers is the system from which the data for this thesis has been obtained. Therefore this system will be explained in more detail than the rosette.

The type of single strain gauge used is a vibrating wire, which measures strain in one direction. Strains are measured using the vibrating wire principle. A length of steel wire is tensioned between two end blocks that are firmly in contact with the mass concrete. Deformations in the concrete will cause the two end blocks to move in relation to each other, altering the tension in the steel wire. This change in tension is measured as a change in the resonant frequency of vibration of the wire. Two coils, one with a magnet insert, the other with a pole piece insert, are located close to the vibrating wire. In use, a pulse of varying frequency is applied to the coils causing the wire to vibrate primarily at its resonant frequency. Portable readouts and dataloggers provide the necessary voltage pulses to pluck the wire.

All vibrating wire strain gages are equipped with a thermistor for reading temperature. The thermistor gives a varying resistance output as the temperature changes.

The purpose of these gauges is to measure the strain in the concrete; these measurements can be used to help:

1. predict the lifespan of the bridge or component;
2. verify the structural model;
3. validate the design assumptions;
4. structural health diagnosis through the bridge's lifespan;
5. analyse the effect of construction activities on the towers.

The static strain gauges are located on each tower at +7,5 m OD (base) and at +135 m OD (top) and on piers S1, S2, N1 (at +9 m OD) and N2 (at +20 m OD). The principle arrangement for the static strain gauges installed in the towers is shown in ***Figure 3.14***.

The static strain gauges are housed in stainless steel and are embedded in the concrete, fixed to the reinforcement. These connections are made by rubber tape and wire ties, see ***Figure 3.15***.

These strain sensors are used during the service life of the bridge as well as during construction. The DAU and signal conditioning systems to be used during construction

are standalone systems. This is necessary as the local and global networks that will be used during the service life of the bridge were not be in place.

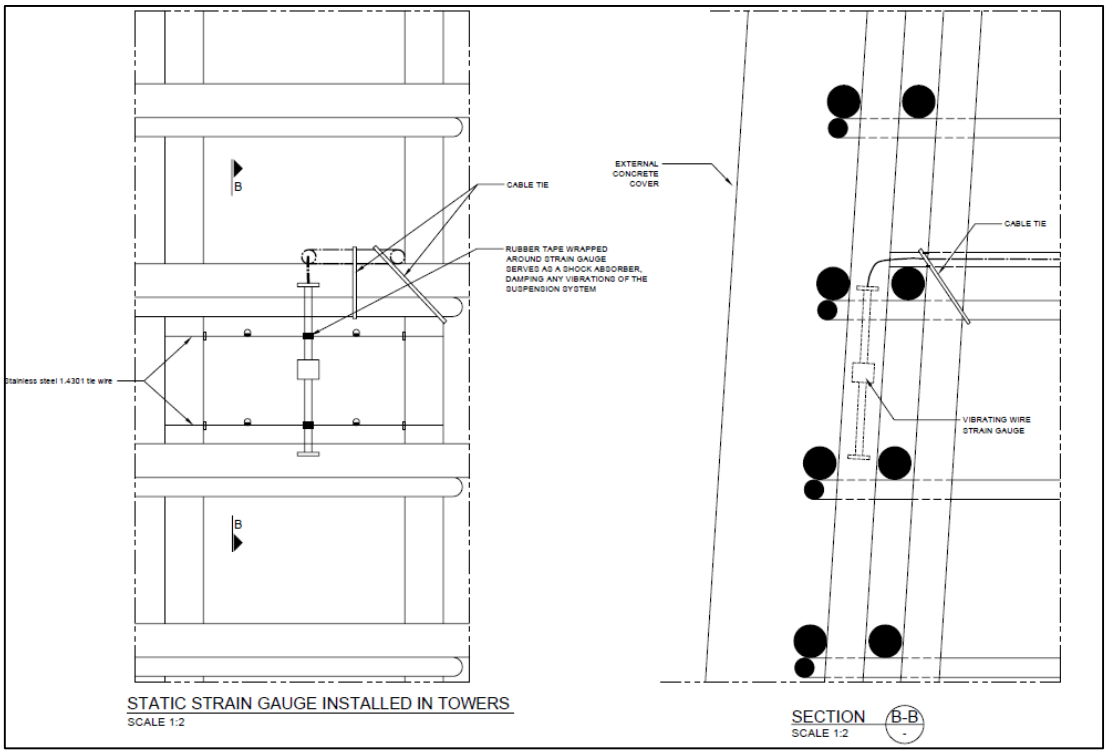

Figure 3.14. Principle arrangement of a static strain gauge *(Ramboll b, 2015)*

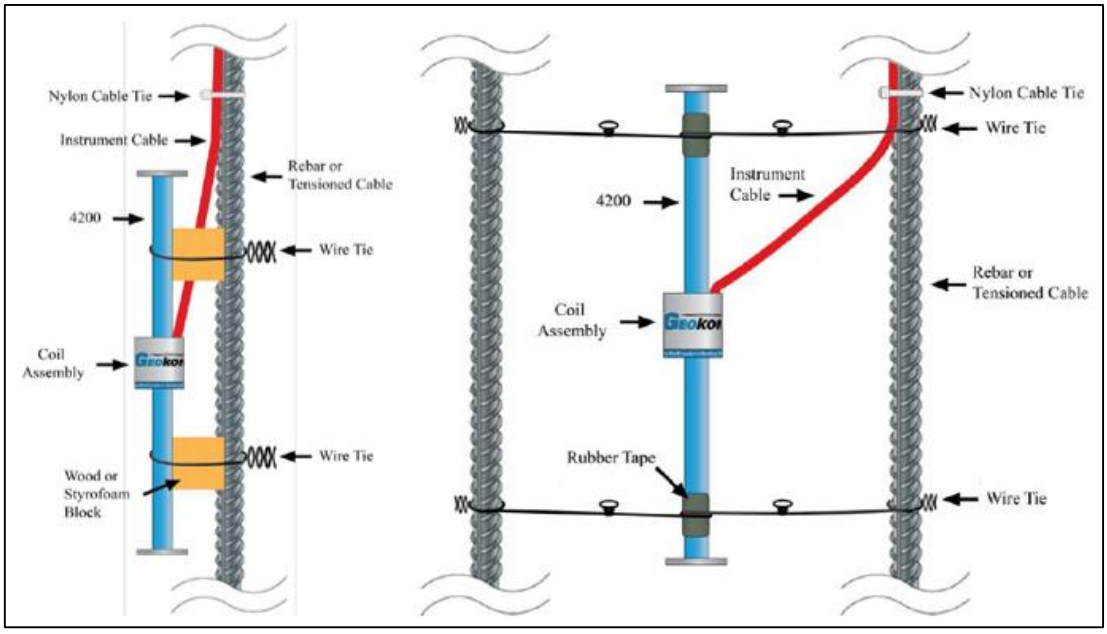

Figure 3.15. Strain gauge connections detail: attached to rebar (left) and suspended between rebar (right)

Strain data used in the analysis developed in the thesis were collected at the base of all three towers during the construction time period of the bridge, starting from February 2014 up to June 2017.

At the base of each tower there are 8 static strain gauges, measuring strain in vertical direction. Their location is shown in ***Figure 3.16***.

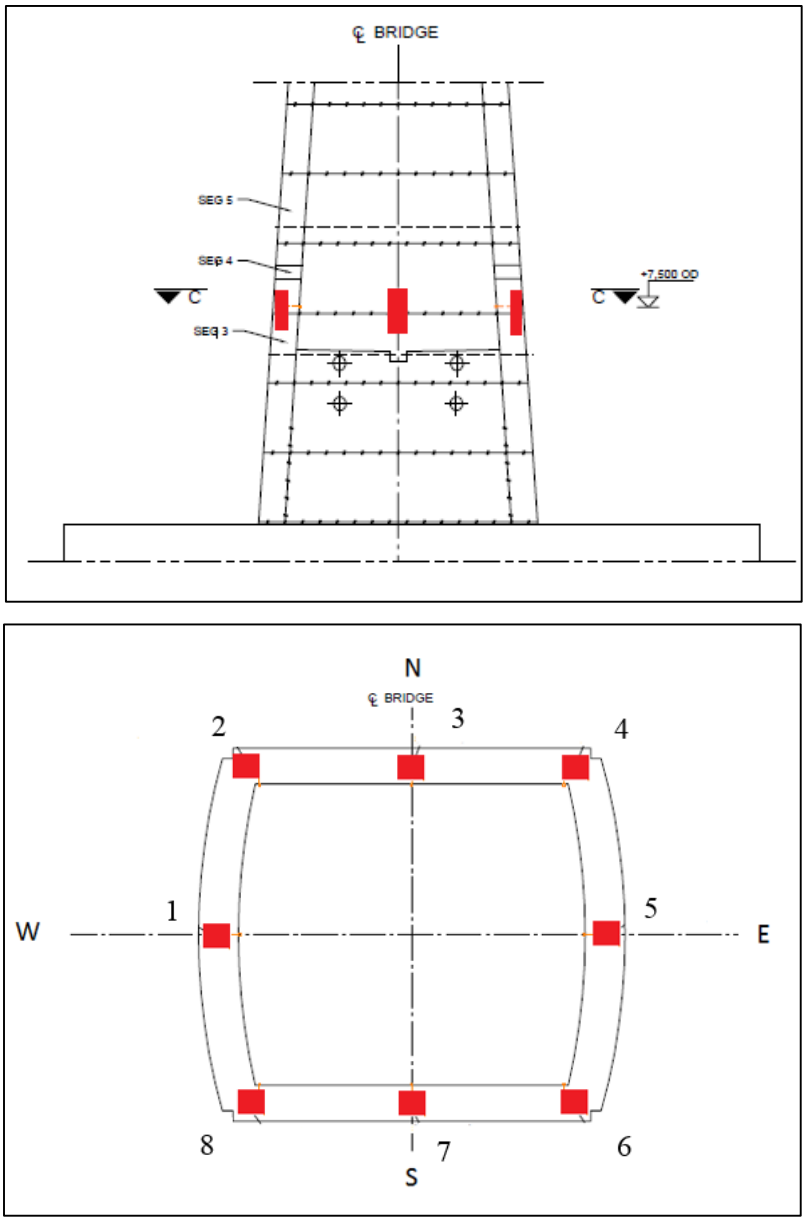

Figure 3.16. Towers base strain gauges general arrangement

Each sensor has a name that changes for each tower according to its location on the sides of the section. The table below shows their identification code:

	SOUTH TOWER	CENTRAL TOWER	NORTH TOWER
1	ST-OD7.5-S-STR-S-1076	CT-OD7.5-S-STR-S-1192	NT-OD7.5-S-STR-S-1340
2	ST-OD7.5-S-STR-S-1077	CT-OD7.5-S-STR-S-1193	NT-OD7.5-S-STR-S-1341
3	ST-OD7.5-S-STR-S-1078	CT-OD7.5-S-STR-S-1194	NT-OD7.5-S-STR-S-1342
4	ST-OD7.5-S-STR-S-1079	CT-OD7.5-S-STR-S-1195	NT-OD7.5-S-STR-S-1343
5	ST-OD7.5-S-STR-S-1080	CT-OD7.5-S-STR-S-1196	NT-OD7.5-S-STR-S-1344
6	ST-OD7.5-S-STR-S-1081	CT-OD7.5-S-STR-S-1197	NT-OD7.5-S-STR-S-1345
7	ST-OD7.5-S-STR-S-1082	CT-OD7.5-S-STR-S-1198	NT-OD7.5-S-STR-S-1346
8	ST-OD7.5-S-STR-S-1083	CT-OD7.5-S-STR-S-1199	NT-OD7.5-S-STR-S-1347

Table 3.2. Towers base (+7,5 m OD) static strain gauges identification codes

Every device has its own built-in temperature sensor in order to execute the temperature compensation. Therefore, temperature is measured in the same positions where the strain gages are located:

	SOUTH TOWER	CENTRAL TOWER	NORTH TOWER
1	ST-OD7.5-S-TMP-S-1076	CT-OD7.5-S-TMP-S-1192	NT-OD7.5-S-TMP-S-1340
2	ST-OD7.5-S-TMP-S-1077	CT-OD7.5-S-TMP-S-1193	NT-OD7.5-S-TMP-S-1341
3	ST-OD7.5-S-TMP-S-1078	CT-OD7.5-S-TMP-S-1194	NT-OD7.5-S-TMP-S-1342
4	ST-OD7.5-S-TMP-S-1079	CT-OD7.5-S-TMP-S-1195	NT-OD7.5-S-TMP-S-1343
5	ST-OD7.5-S-TMP-S-1080	CT-OD7.5-S-TMP-S-1196	NT-OD7.5-S-TMP-S-1344
6	ST-OD7.5-S-TMP-S-1081	CT-OD7.5-S-TMP-S-1197	NT-OD7.5-S-TMP-S-1345
7	ST-OD7.5-S-TMP-S-1082	CT-OD7.5-S-TMP-S-1198	NT-OD7.5-S-TMP-S-1346
8	ST-OD7.5-S-TMP-S-1083	CT-OD7.5-S-TMP-S-1199	NT-OD7.5-S-TMP-S-1347

Table 3.3. Towers base (+7,5 m OD) temperature sensors identification codes

In the following part of the thesis, the methodology used for strain data analysis collected on the three towers and their processing will be described.

4. Inference method

The purpose of the research carried out in this thesis was to determine if monitoring data from the SHM deployment on the Queensferry Crossing could be used to infer when key construction operations were taking place. Moreover, another key point of the research was to point out if it is possible to reconstruct the deformative history of the concrete used for the three towers (linear elastic, shrinkage and creep deformation).

The research methodology applied throughout this project has been both qualitative and quantitative in nature.

The qualitative research included a review of selected SHM literature. This provided the author with a grounding in the subject area and allowed for suitable introduction to this topic to be provided for the reader. Following this, a detailed review of the Queensferry Crossing was carried out, focusing on the development of the project, the structural scheme, the construction phases and finally the SHM deployment.

This provided the author with the required level of understanding of the structural behaviour of the bridge, the construction process and the SHM deployment to discuss the monitoring data and offer qualitative comments on the results of data analysis.

The quantitative process of this research involved analysing and processing data from selected sensors of the SHM system deployed on the Queensferry Crossing. All data analysis was carried out using Microsoft Excel and Matlab.

4.1 Data acquisition

The data analysed in this project were registered by selected SHM sensors on the Queensferry Crossing throughout the construction process and then collected by The Forth Crossing Bridge Constructors. These data were then acquired by the authors' supervisor Prof. Daniele Zonta.

The acquired information consisted of strain and temperature data, some technical drawings of piers, towers and sensors location and construction data, reporting towers and deck segments lift dates and weights. Strain and temperature data were registered by static strain gauges located at the base of the three tower, on the top of the Centre Tower and on some of the deck segments. The sampling frequency of the sensors was one per

minute. For each sample, from each sensor, strain, temperature, time and date of the sample was recorded. Due to the large volume of data, each spreadsheet contained data from a one-month period only.

4.2 Data analysis and processing methods

Firstly, all the spreadsheet provided were combined using Matlab, in order to create a unique time vector from the starting sample to the ending one, with the relative strain and temperature registered data. Then a selection of the data to be processed was required, because of the magnitude of the volume of data available. Therefore, strain measurements collected at the base of each tower were used, since deck construction process (balance cantilevering) should have highlighted a peculiar strain trend due to the alternating deck segment lifts. Moreover, these data were the fullest datasets, including a large period of time (almost 3 years of measurements). A bigger detail was given to the CT, since it supported the longest ever free standing cantilever bridge deck during the construction process (Watt, 2017). Due to this the CT would experience the largest moments and deformations compared to the FTs. The author speculated that this would have a noticeable impact on the strain signals of the CT. Which would enable identification of deck erection operations in the SHM data.

Finally, a further selection had to be made about which of the sensor should be analysed. At the base of each tower, there are eight strain gauges, as mentioned before (see *Strain gauges,* **Figure 3.16**). In order to obtain a complete picture of what is happening on the towers during construction, one sensor data for each side of each tower were analysed. Thus, you can see the strain trend both on the two sides that experienced the largest changes in strain (those on the Centre Line of the bridge, North and South, due to balance cantilevering) and on the 'neutral axis' (West and East sides).

After selection of data, processing methodology has been developed in order to achieve the aims of the thesis. Firstly, in order to have a clear idea of the overall change in strain from the beginning of the measurements, the first strain and temperature signals were subtracted from all subsequent signals. Then, a temperature correction was needed as reported on the strain gauges instruction manual. Temperature can affect not only the concrete but also the strain gauge. Increasing temperature will cause the vibrating wire to elongate and thus go slack, indicating what would appear to be a compressive strain in

the concrete. This is due to the different coefficient of expansion of concrete. The actual strain undergone by the concrete is given by the formula:

$$\mu\varepsilon_{actual} = (R_1 - R_0)B + (T_1 - T_0)C_1$$

where:

- R_0 is the initial reading,
- R_1 is the current reading from the readout box,
- B is the batch gage factor supplied with each gage,
- T_0 is the initial temperature,
- T_1 is the current temperature,
- C_1 is the coefficient of expansion of steel.

The sensors used in the towers are Geokon 4200, so the batch gage factor is equal to 0,98 and C_1=12,2 με/°C.

Then, after the strain data correction, the analysis and interpretation has been carried out, trying to understand the different components influencing the strain registered. In particular, a deformation model dependent on four different components has been built:

1. *Linear elastic strain*, due to the incremental loading on the concrete segment where the sensors are embedded in;
2. *Creep*, due to the same loading;
3. *Shrinkage*, natural concrete volume reduction after its casting;
4. *Temperature*, which is cause of the daily and seasonal strain variation.

The model has been studied and built in order to extrapolate the different parameters of the concrete related to each of the strain components:

1. Modulus of elasticity *E*;
2. Creep coefficient φ_∞;
3. Shrinkage strain at time t=∞, $\varepsilon_{s,\infty}$;
4. Thermal coefficient α.

The estimation of these parameters was carried out using two different methods of data analysis: *Least Squares Analysis* (LSA) and the *Bayesian multi-parameter estimation*.

4.3 Least Squares Analysis

The least squares analysis (LSA) is a standard regression analysis technique. LSA was applied to the recorded data to ultimately compute the mean and standard deviation of each of the unknown parameters. Carl Friedrich Guass constructed the LSA based on the principle that "the most probable value of the unknown quantities will be that one for which the sum of the squares of the differences between the actually observed and computed values multiplied by numbers that measure the degree of precision is a minimum" (Strejc, 1980). Thus, application of a LSA technique ultimately produces a least squares vector; the following equation defines the least squares criterion:

$$Q = \sum_{i=1}^{n} [y_i - f(x_i, \theta)]^2 = min$$

where:

- Q represents the least squares vector;
- y_i represents the observations from sensors ($\Delta\varepsilon_i$);
- f represents the parametric model considered;
- x_i represents the variables of the model;
- θ represents the unknown parameters to be estimated.

The estimated parameters are established by computing suitable values to result the minimum sum of squared deviations between the observed results and the functional output, i.e. the minimum least squares vector (Q) (NIST/SEMATECH, 2012).

The vector of the estimated least squares parameters is $\boldsymbol{\theta}$:

$$\boldsymbol{\theta} = \begin{bmatrix} \theta_1 \\ \vdots \\ \theta_p \end{bmatrix}, \text{ where p is the number of parameters.}$$

Considering a general model depending on time:

$$f_1 = \theta_1 \cdot x_{11} + \ldots + \theta_j \cdot x_{j1} + \ldots + \theta_p \cdot x_{p1} + e$$

$$\vdots$$

$$f_i = \theta_1 \cdot x_{1i} + \ldots + \theta_j \cdot x_{ji} + \ldots + \theta_p \cdot x_{pi} + e$$

$$\vdots$$

$$f_N = \theta_1 \cdot x_{1N} + \ldots + \theta_j \cdot x_{jN} + \ldots + \theta_p \cdot x_{pN} + e$$

with:

- $i = 1, \ldots, N$ number of measurements,
- $j = 1, \ldots, p$ number of parameters to estimate,
- e = error term;

the system can be written in matrix form:

$$\begin{bmatrix} f_1 \\ \vdots \\ f_i \\ \vdots \\ f_N \end{bmatrix} = \begin{bmatrix} x_{11} & \cdots & x_{j1} & \cdots & x_{p1} \\ \vdots & \ddots & \vdots & \ddots & \vdots \\ x_{1i} & \cdots & x_{ji} & \cdots & x_{pi} \\ \vdots & \ddots & \vdots & \ddots & \vdots \\ x_{1N} & \cdots & x_{jN} & \cdots & x_{pN} \end{bmatrix} \cdot \begin{bmatrix} \theta_1 \\ \vdots \\ \theta_i \\ \vdots \\ \theta_N \end{bmatrix}$$

$$\boldsymbol{f} = \boldsymbol{D} \cdot \boldsymbol{\theta}$$

where $D_{ij} = \frac{\partial f(x_i, \boldsymbol{\theta})}{\partial \theta_j}$.

Then the residuals vector $\mathbf{Y}$, which includes the deviation of the measured data y_i from their expected values (Kutner, et al., 2005), and the covariance matrix $\boldsymbol{\Sigma}$ of the estimated parameters can be calculated as follows:

$$\boldsymbol{Y} = \boldsymbol{y} - \boldsymbol{D} \cdot \boldsymbol{\theta}$$

$$\boldsymbol{\Sigma} = \frac{\boldsymbol{Y}^{\mathbf{T}} \boldsymbol{Y}}{\boldsymbol{N} - \boldsymbol{p}} (\boldsymbol{D}^{\mathbf{T}} \cdot \boldsymbol{D})^{-\mathbf{1}}$$

The method aims to minimize the sum of the squared residuals:

$$Q = \sum_{i=1}^{n} [y_i - f(x_i, \boldsymbol{\theta})]^2$$

$$Q = \boldsymbol{Y}^{\mathbf{T}} \boldsymbol{Y} = (\boldsymbol{y} - \boldsymbol{D} \cdot \boldsymbol{\theta})^{\mathbf{T}} \cdot (\boldsymbol{y} - \boldsymbol{D} \cdot \boldsymbol{\theta})$$

Q can be minimized by calculating the derivatives of $f(x_i, \boldsymbol{\theta})$ with respect to each parameter θ_j, and setting them equal to zero:

$$\frac{\partial Q}{\partial \theta_j} = \sum_{i=1}^{n} -2[y_i - f(x_i, \boldsymbol{\theta})] \cdot \left[\frac{\partial f(x_i, \boldsymbol{\theta})}{\partial \theta_j} \right] = 0$$

which is in matrix form:

$$\frac{\partial Q}{\partial \theta_j} = \sum_{i=1}^{n} -2\left[D_{ij} \cdot \theta_j - y_i\right] \cdot D_{ij} = 0$$

$$(\boldsymbol{D} \cdot \boldsymbol{\theta} - \boldsymbol{y})^{\mathbf{T}} \cdot \boldsymbol{D}^{\mathbf{T}} = 0$$

$$\boldsymbol{D}^{\mathbf{T}}\boldsymbol{D} \cdot \boldsymbol{\theta} = \boldsymbol{D}^{\mathbf{T}} \cdot \boldsymbol{y}$$

From this formulation, we can calculate the parameters vector $\boldsymbol{\theta}$ as follows:

$$\boldsymbol{\theta} = (\boldsymbol{D}^{\mathbf{T}}\boldsymbol{D})^{-\mathbf{1}}\boldsymbol{D}^{\mathbf{T}} \cdot \boldsymbol{y} = \boldsymbol{D}^{*} \cdot \boldsymbol{y}$$

where $\boldsymbol{D}^{*} = (\boldsymbol{D}^{\mathbf{T}} \cdot \boldsymbol{D})^{-\mathbf{1}} \cdot \boldsymbol{D}^{\mathbf{T}}$ is the Pseudo Inverse matrix of **D**.

4.4 Bayesian approach

Bayesian inference is a method of statistical inference in which Bayes' theorem is used to update the probability for a hypothesis as more evidence or information becomes available. Bayes' theorem describes the probability of an event, based on prior knowledge of conditions that might be related to the event (Bolstad, 2010):

$$p(\boldsymbol{\theta}|\boldsymbol{y}) = \frac{p(\boldsymbol{y}|\boldsymbol{\theta}) \cdot p(\boldsymbol{\theta})}{p(\boldsymbol{y})}$$

where:

- p (**θ**|**y**) = *posterior* probability, that is the probability of **θ** given **y.** This tells us what we want to know: the probability of a hypothesis given the observed evidence (available data);
- p (**y**) = *evidence*, that is the sampling distribution of the observations.
- p (**y**|**θ**) = *likelihood function*, that is the distribution of the observed data marginalized over the parameter(s). It indicates the compatibility of the evidence with the given hypothesis;
- p (**θ**) = *prior* probability, that is the distribution of the parameter(s) before any data is observed, based on *a priori* knowledge of the parameter(s).

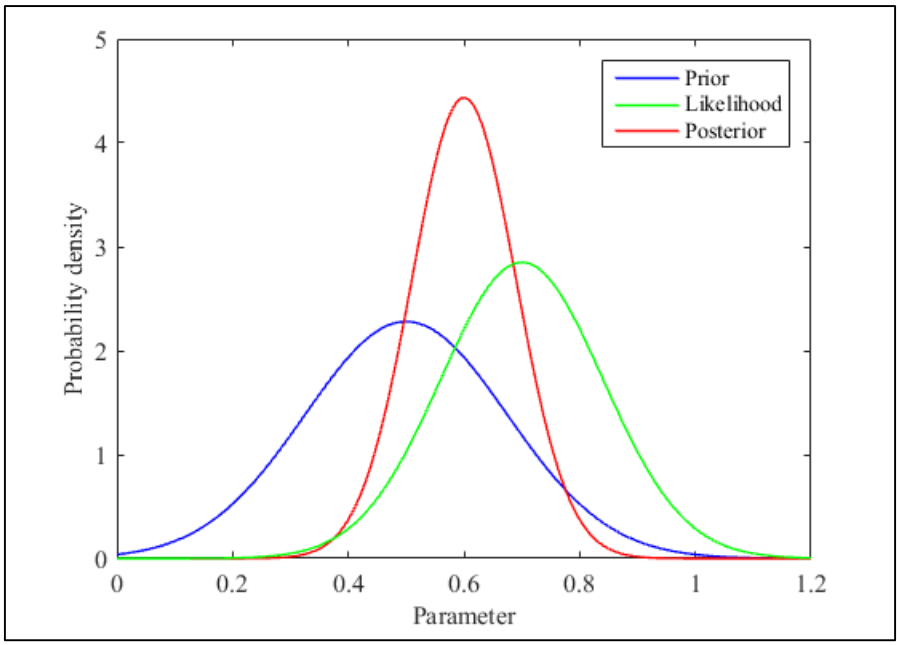

Figure 4.1. Graphic representation of the Bayes' theorem

In the field of continuous variables, the calculation of the posterior distribution is computationally difficult because of the evidence:

$$p(\boldsymbol{y}) = \int_{-\infty}^{+\infty} p(\boldsymbol{y}|\boldsymbol{\theta}) \cdot p(\boldsymbol{\theta}) \cdot d\boldsymbol{\theta}$$

However, the posterior probability is proportional to the product between the likelihood function and the prior distribution:

$$p(\boldsymbol{\theta}|\boldsymbol{y}) \propto p(\boldsymbol{y}|\boldsymbol{\theta}) \cdot p(\boldsymbol{\theta})$$

$$p(\boldsymbol{y}|\boldsymbol{\theta}) = \prod_{i=1}^{N} p(y_i|\boldsymbol{\theta}), \quad p(\boldsymbol{\theta}) = \prod_{j=1}^{\boldsymbol{p}} p(\theta_j)$$

i = 1, … N number of measurements,

j = 1, …, p number of parameters.

As a consequence, in order to implement the Bayes' theorem, it is necessary to use a specific numerical method.

In this case, the Markov Chain Monte Carlo (MCMC) methods can be applied to generate samples from the posterior distribution. These methods do not allow to draw our sample from the posterior distribution directly. Rather we set up a Markov chain that has the posterior distribution as its limiting distribution. We let the Markov chain run a long time until it has approached the limiting distribution. Any value taken after that initial run-in time

approximates a random draw from the posterior distribution. Values taken from the Markov chain at time points close to each other are highly correlated, while, values at widely separated points in time are approximately independent. An approximately random sample from the posterior distribution can be found by taking values from a single run of the Markov chain at widely spaced time points after the initial run-in time (Bolstad, 2010).

In particular, the Metropolis–Hastings (MH) algorithm can draw samples from any probability distribution P(x) (in this case $p(\boldsymbol{\theta}|\boldsymbol{y})$), provided that the value of a function f(x) proportional to the density of P(x) can be calculated (in this case the product $p(\boldsymbol{y}|\boldsymbol{\theta}) \cdot p(\boldsymbol{\theta})$). All we know is the unscaled target given by the prior times the likelihood. This gives the shape of the desired function, but not the scale factor needed to make it an exact density (Bolstad, 2010).

4.4.1 Metropolis-Hastings Algorithm

The Metropolis–Hastings algorithm works by generating a sequence of sample values in such a way that, as more and more sample values are produced, the distribution of values more closely approximates the desired distribution P(x). These sample values are produced iteratively, with the distribution of the next sample being dependent only on the current sample value (thus making the sequence of samples into a Markov chain). Specifically, at each iteration, the algorithm picks a candidate for the next sample value based on the current sample value (*random walk*). Then, with some probability, the candidate is either accepted (in which case the candidate value is used in the next iteration) or rejected (in which case the candidate value is discarded, and current value is reused in the next iteration). The probability of acceptance is determined by comparing the values of the function f(x) of the current candidate sample values with respect to the desired distribution P(x) (Bolstad, 2010).

In this case, suppose we have p parameters θ_1, ..., θ_p, and then the following parameter vector:

$$\boldsymbol{\theta}=(\theta_1, ..., \theta_p)$$

The steps of the algorithm are:

1. Start at an initial value $\boldsymbol{\theta}^{(0)}$;
2. For n = 1, …, N:

- Draw $\boldsymbol{\theta}$**'** from $q(\boldsymbol{\theta}^{(n-1)}, \boldsymbol{\theta}') = q(\boldsymbol{\theta}' | \boldsymbol{\theta}^{(n-1)})$ which is the probability of $\boldsymbol{\theta}'$ given $\boldsymbol{\theta}^{(n-1)}$: this is a multivariate normal distribution with mean $\boldsymbol{\theta}^{(n-1)}$, and covariance SIGMA that can be set as it represents a research function;
- Compute the ratio $r = \frac{g(\boldsymbol{\theta}'|y)}{g(\boldsymbol{\theta}^{(n-1)}|y)}$, where $g(\boldsymbol{\theta}|y)$ is the posterior density;
- Calculate the probability $\alpha(\boldsymbol{\theta}^{(n-1)}, \boldsymbol{\theta}') = \min(1, r)$;
- Draw a random number u from the uniform distribution U defined in (0,1);
- If $u < \alpha(\boldsymbol{\theta}^{(n-1)}, \boldsymbol{\theta}')$, then let $\boldsymbol{\theta}^{(n)} = \boldsymbol{\theta}'$, else let $\boldsymbol{\theta}^{(n)} = \boldsymbol{\theta}^{(n-1)}$.

3. At the end of the cycle (n=N), we have N samples $\boldsymbol{\theta}_1, \ldots, \boldsymbol{\theta}_N$, however the initial "burn-in" values (N_1<N) have to be discard, that is a first sampling period after which the algorithm becomes stable.

In conclusion, the MH algorithm provides a set of parameter vectors with the same probability. Then, we state that the final parameter vector $\boldsymbol{\theta}$ is the mean values of the samples.

5. Data analysis

The strain measurements that are object of this thesis are embedded in one of the concrete tower segments, located at +7,5 m OD. Here the main features of the sections analysed will be reported, in order to give the reader a clear knowledge of the geometry and the materials.

Centre Tower

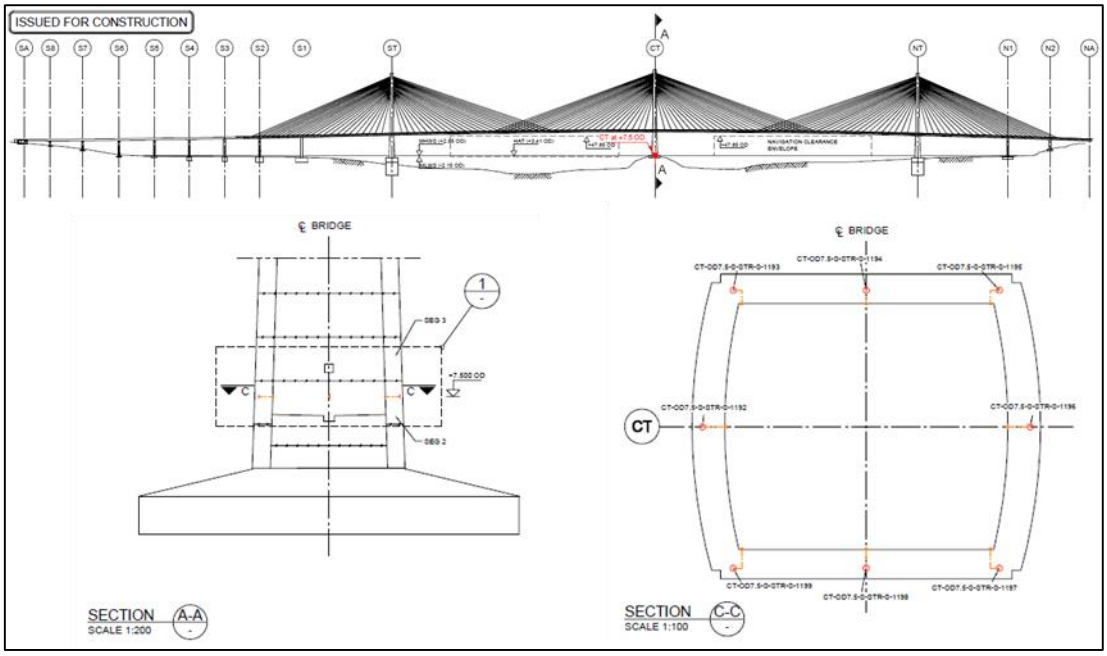

Figure 5.1. Centre Tower strain gages disposition *(Ramboll e, 2013)*

The strain gages are embedded in the segment No. 2 that has the following features:

Height [m]	North-South dimension [m]	West-East dimension [m]	Wall thickness [m]	Section [m^2]	Concrete
4	13,47	14,93	1,6	75	C55/67

South and North Tower

The sensors are located in the segment No. 4 that has the following features:

Height [m]	North-South dimension [m]	West-East dimension [m]	Wall thickness [m]	Section [m^2]	Concrete
4	13,21	14,40	1,5	73	C55/67

5.1 Full-time history of uncompensated strain and temperature

Firstly, the full-time history of the raw data, in the form they were received, have been plotted. Strain has been registered from the 20th February 2014 on the CT, while data start from the 17th June 2014 on the NT and from the 18th August 2014 on the ST. Data are available until June 2017 for each tower. Below, the full raw strain datasets of the CT sensors are reported. For completeness, the plots concerning the two FTs have been reported in *Annex 1*. The same reporting method will be used for all the following analysis carried out in this Section.

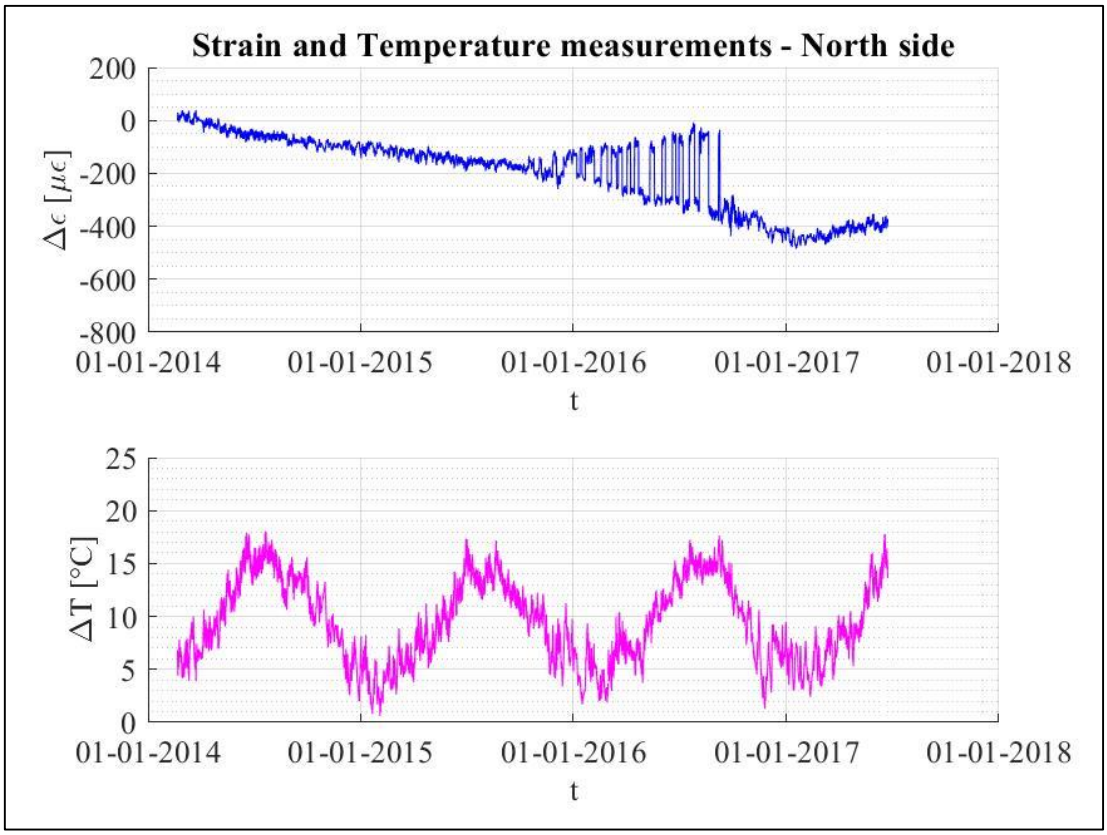

Figure 5.2. Raw strain measurements and temperature data from CT-OD7.5-S-STR-S-1194 (North side)

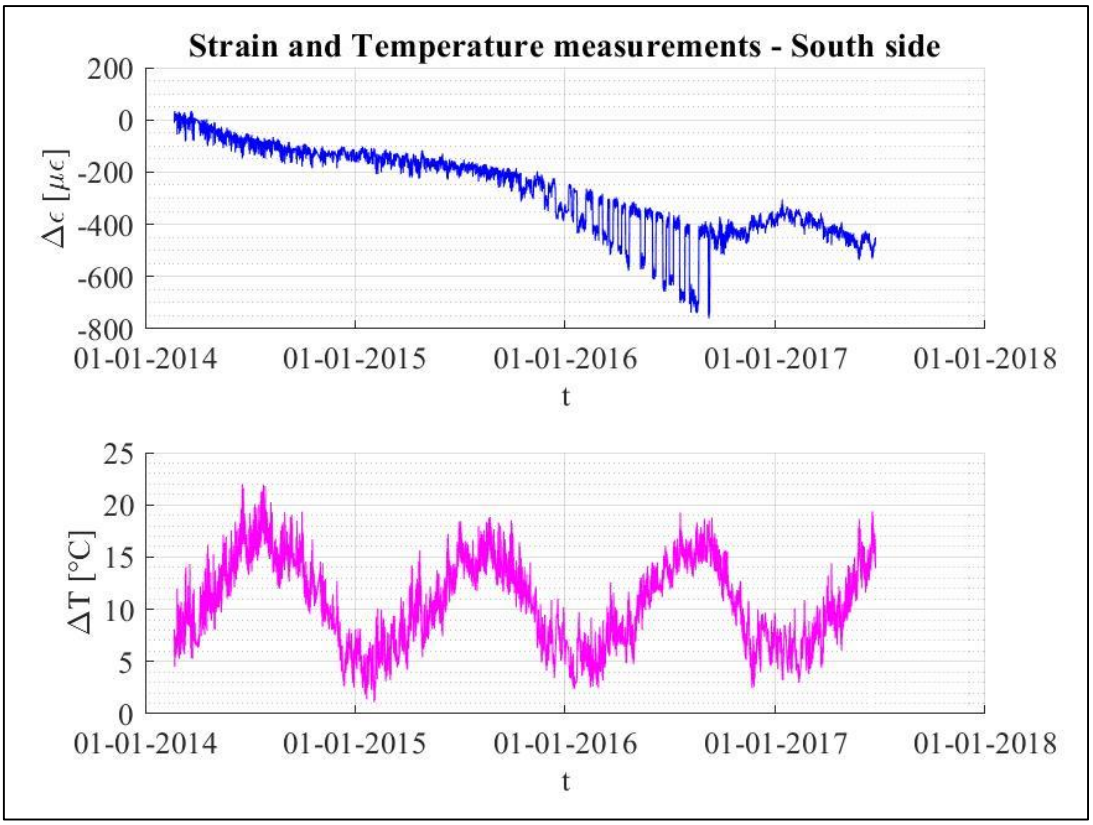

Figure 5.3. Raw strain measurements and temperature data from CT-OD7.5-S-STR-S-1198 (South side)

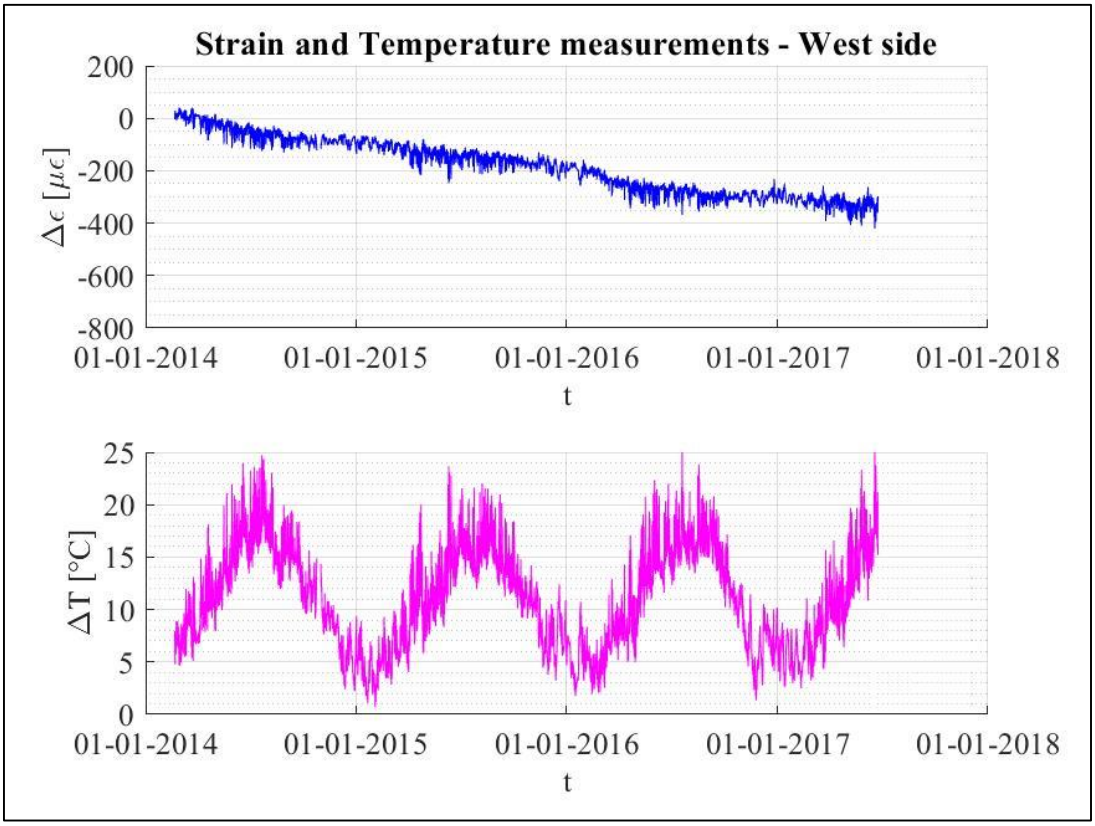

Figure 5.4. Raw strain measurements and temperature data from CT-OD7.5-S-STR-S-1192 (West side)

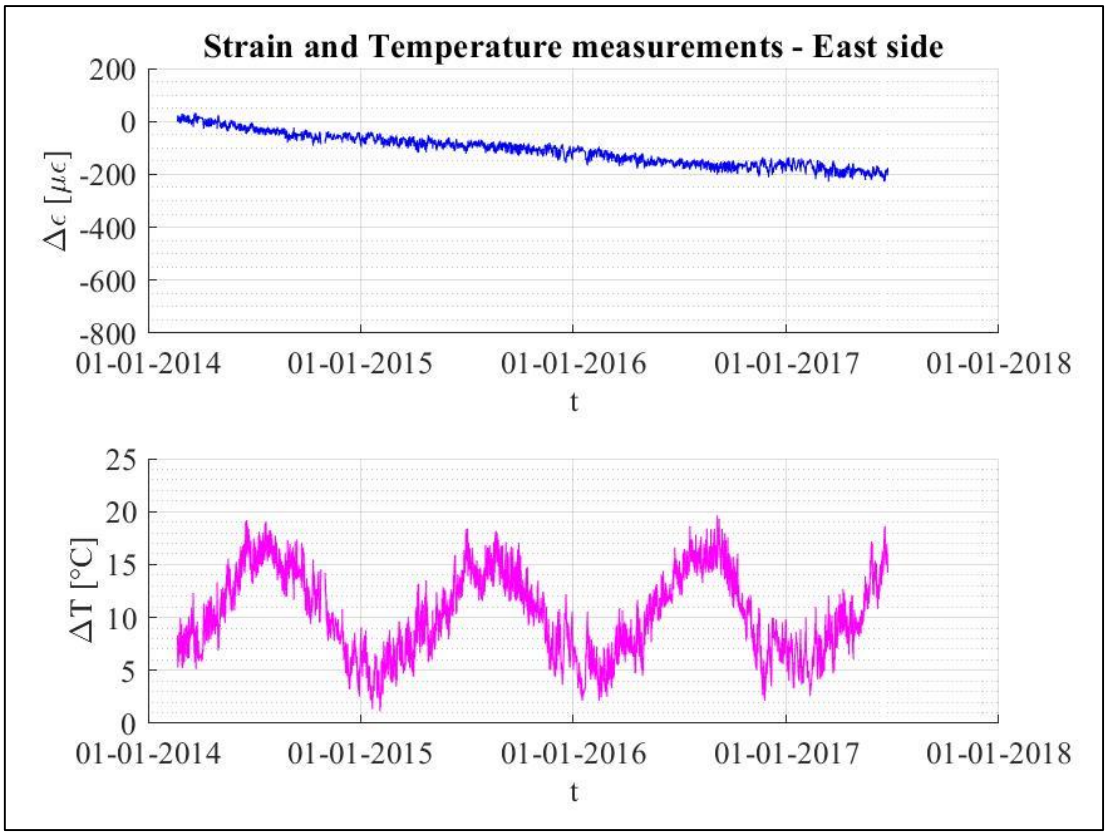

Figure 5.5. Raw strain measurements and temperature data from CT-OD7.5-S-STR-S-1194 (East side)

5.1.1 Full-time history of the corrected measurements

Because of the temperature influence on the registered strain signals that affects the measures, a temperature correction was needed in order to clean them up, as already mentioned in *4.2*. According to the *Eq. 1*:

$$\mu\varepsilon_{actual} = (R_1 - R_0)B + (T_1 - T_0)C_1$$

the registered signals (R_1-R_0)B have to be corrected by adding a term dependent on temperature and proportional to the thermal coefficient of the steel. In order to explain this correction, assume, as an example, that the strain gage is inside a concrete slab that is perfectly restrained at its ends. If the temperature rises by 1°C, then the vibrating wire undergoes an expansion of +12,2 με and the signal (R_1-R_0)B would be -12,2 microstrains, therefore the result of Eq.1 would be 0 actual strain in the concrete slab. On the other hand, if the concrete slab is free of all restraint and experiences a change of +1°C, the concrete would expand about 10 με, while the vibrating wire would still expand 12,2 με. The value of (R_1-R_0)B would be then -2,2 με, and then Eq.1 would yield a value of +10 με, that is the actual change in strain of the concrete slab.

Following, the corrected measurements have been reported.

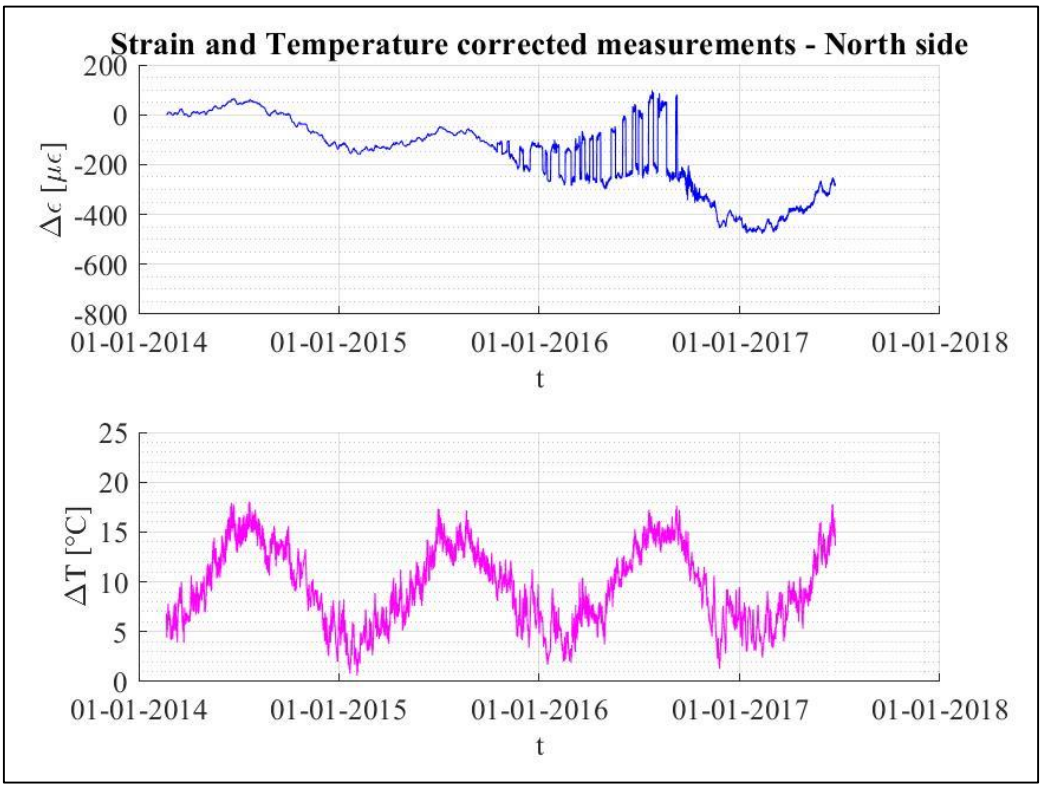

Figure 5.6. Corrected strain measurements and temperature data from CT-OD7.5-S-STR-S-1194 (North side)

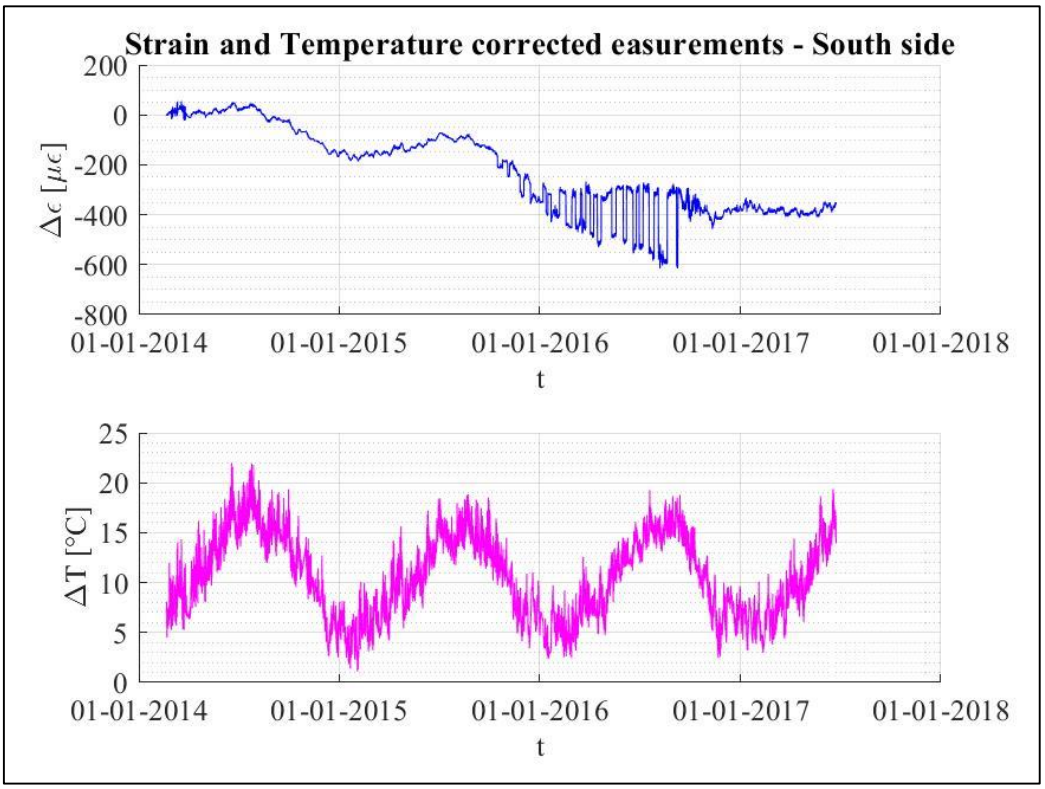

Figure 5.7. Corrected strain measurements and temperature data from CT-OD7.5-S-STR-S-1198 (South side)

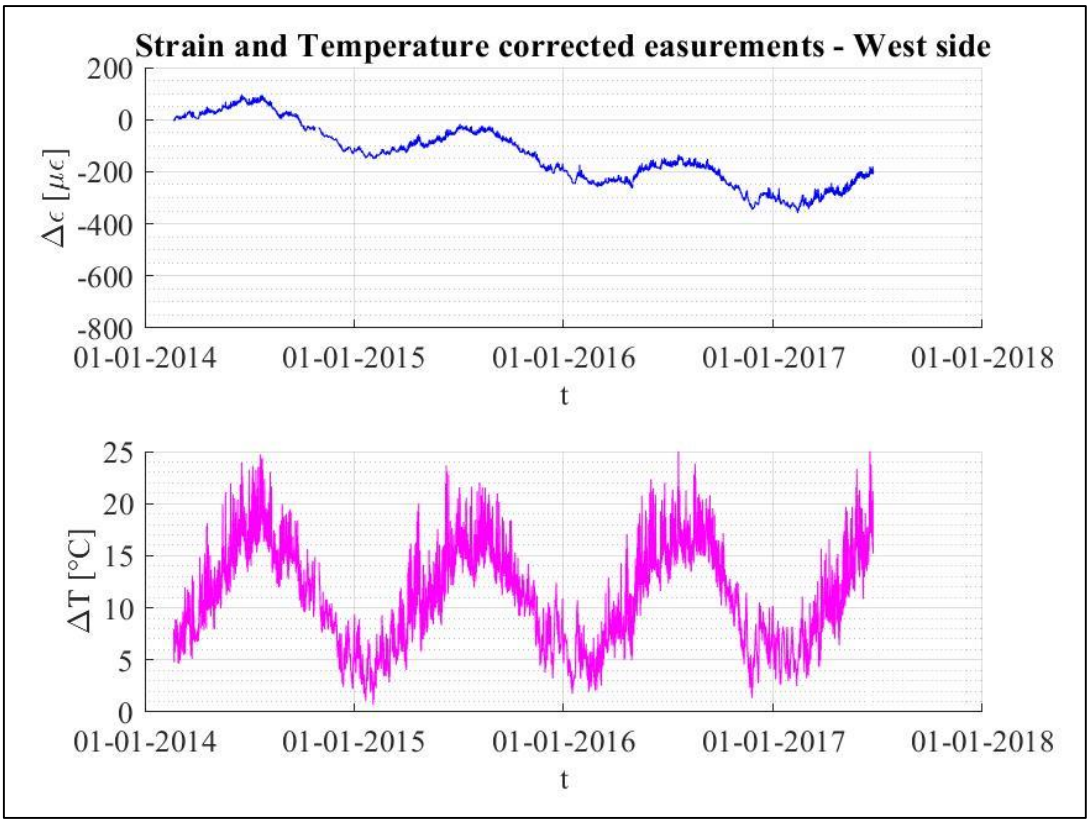

Figure 5.8. Corrected strain measurements and temperature data from CT-OD7.5-S-STR-S-1192 (West side)

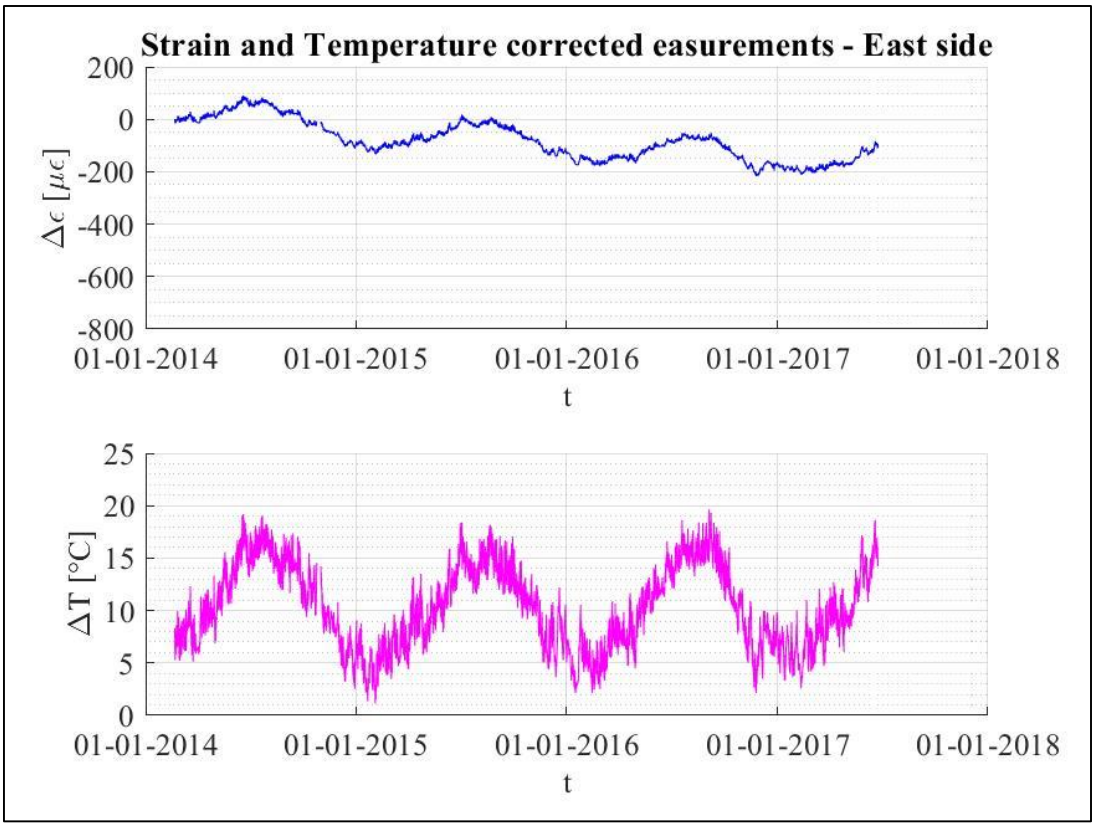

Figure 5.9. Corrected strain measurements and temperature data from CT-OD7.5-S-STR-S-1196 (East side)

5.1.2 Results and discussion

The first clear feature that comes out from these plots is the different trend of the strain signals in the period between October 2015 and October 2016. In fact, while the sensors that are located on the centre-line of the bridge (North and South) registered large alternatively increasing and decreasing changes in strain during this period, the East and West sensors continue their fluctuations with the temperature. Therefore, these large jumps of the strain cannot be clearly attributed to a temperature variation.

This statement can be corroborated by considering the data before the mentioned time period. Analysing the change in strain signal until October 2015, all 4 sensors don't register any large jump roughly following the temperature trend. The changes in temperature signal throughout this time period are broadly same shape as those throughout the full time period, including the period with large jumps in the change of strain measurements. This indicates that temperature change is not the cause of these jumps in strain measurements. Hence, only operational factors would be the cause of the strain jumps. As a matter of fact, due to previous knowledge of the construction process, the author could state that the bridge deck erection is the cause of the large changes in strain signals.

The bridge erection methodology as explained previously is a balanced cantilever construction. Using this method of construction, it would be expected that as a deck section is fitted to one side of the CT fan this would cause an increase in compression at the base of the tower on that side, while at the other side there would be an increase in tension. At the same time, this change of stress (and strain) would not affect the 'neutral axis' of the section. In this case, as the deck segments are aligned on the North-South direction, the neutral axis corresponds to the West-East direction.

In terms of strain signal, the side of the tower to which the deck section was being attached would have an increase in negative strain, while at the same time the other side would have a decrease in strain. Thus the changes in strain signal from both the sensors should oppose each other. When one signal spikes up the other should spikes down, see **Figure 5.10**.

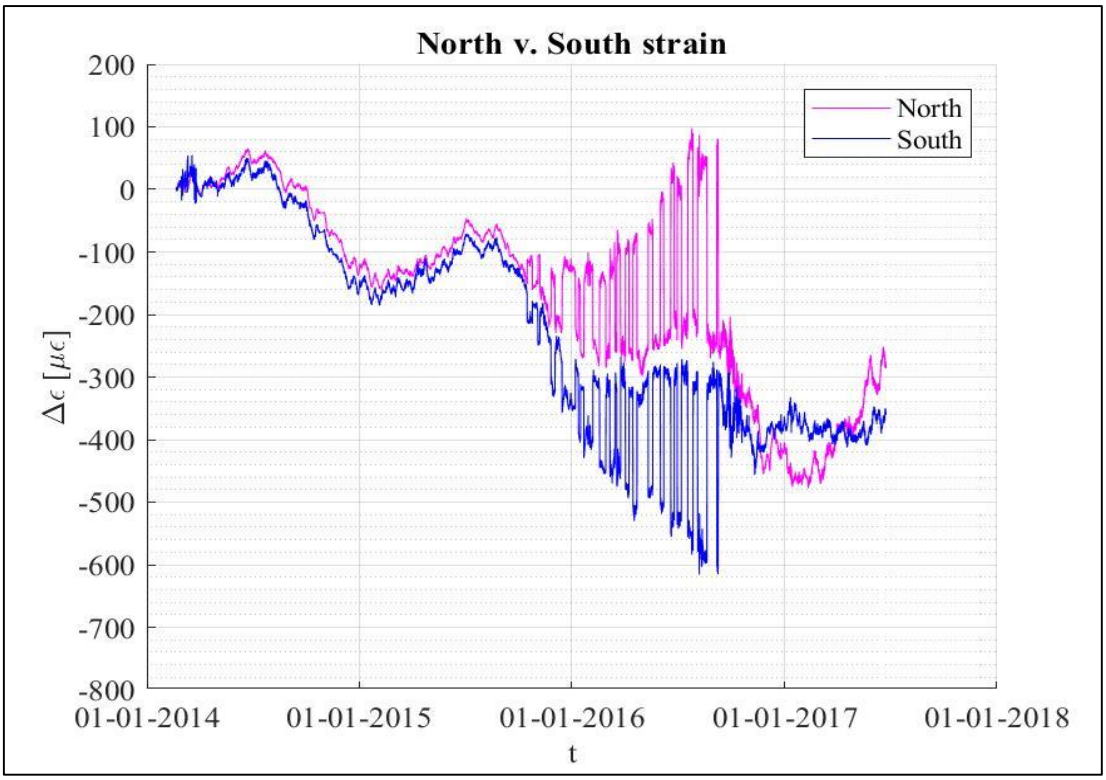

Figure 5.10. Strain signal comparison between North (CT-OD7.5-S-STR-S-1194) and South (CT-OD7.5-S-STR-S-1198) sides

5.1.3 Daily temperature effect

Following the analysis of the uncompensated strain and temperature across the full-time history of the dataset, three-day time spans were chosen for further analysis. In particular, winter and summer solstice were analysed, since during these days the temperature effect should be more evident.

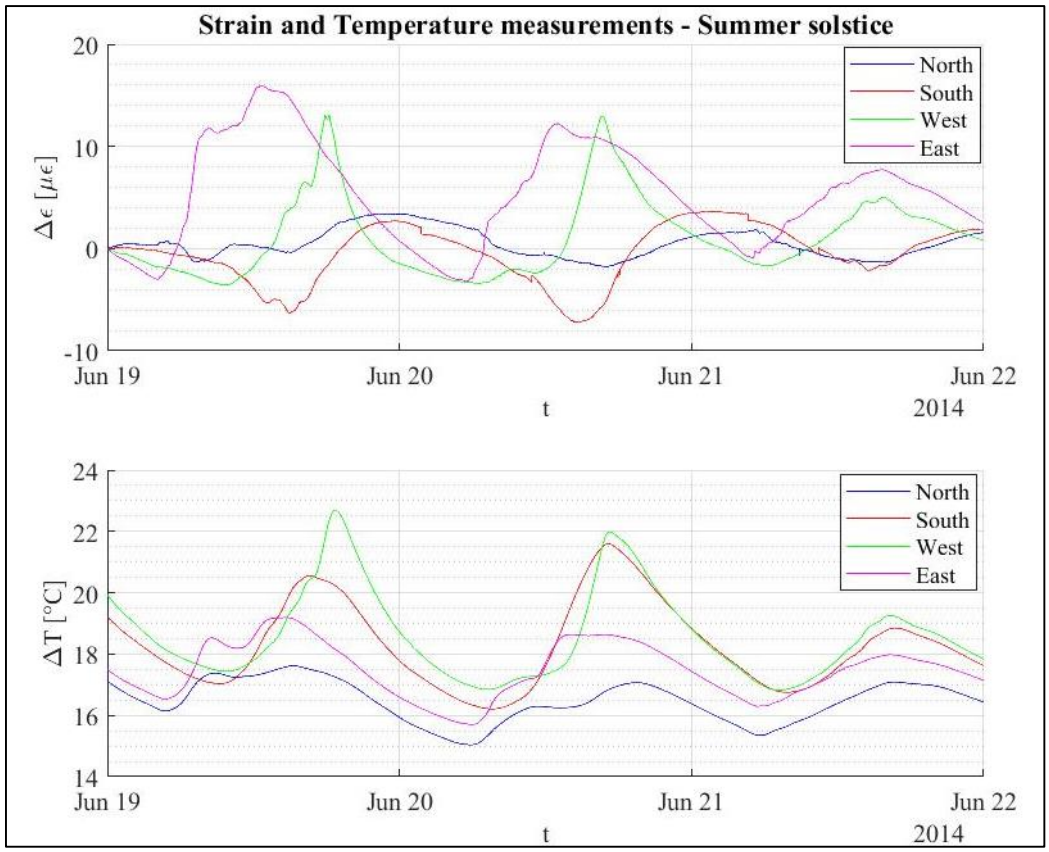

Figure 5.11. Summer solstice (June 2014) uncompensated strain and temperature from the 4 sensors

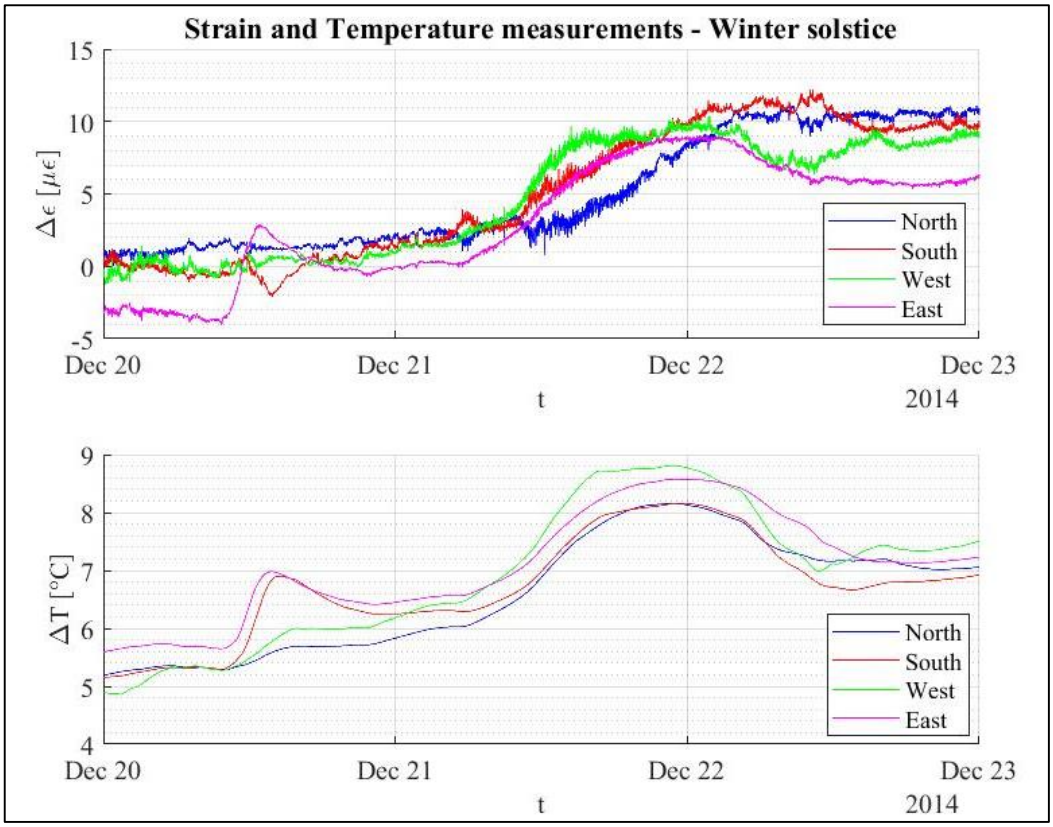

Figure 5.12. Winter solstice (December 2014) uncompensated strain and temperature from the 4 sensors

Firstly, it is interesting to point out how the measured temperature follows the sun path during the day. It is clear that the East side sensor is the first one that sees the temperature increasing, followed by the South side and, finally, the West side sensors. On the contrary, the North side seems not to be affected by this kind of phenomenon. The theory is confirmed just by looking at the path of the sun illustrated in the following picture.

Figure 5.13. Sun path from 21th June 2014 with sunrise and sunset angles *(Torsten Hoffmann)*

The strain pattern is clearly affected by temperature, even if, observing the South and North strain trends in **Figure 5.12**, they seem not to strictly follow the temperature. There is not a clear and immediate explanation to this occurrence. One might think about other unknown factors that influence the strain measured on the North and South sides. One of these can likely be a wind blowing in a North-South direction, so as to "dirty" the measurements. However, since no wind data is available, it is not possible to corroborate this hypothesis.

The next step of the analysis aims to delete the daily temperature effect, in order to work with a less amount of samples and to see the seasonal temperature effect.

5.2 Reduced dataset

The full dataset signals are noisy due to the daily temperature variation and the number of measurements from each sensor for each day (one per minute, that is 1440 signals per day). The dataset was reduced to one significant sample per day, so that reduced plots of strain and temperature can be produced. By doing so, the daily temperature effect can be removed.

The time chosen for a daily sample to be picked was that of 5 AM, just before sunrise. The reason for appointing 5 AM as the time during the day when the samples will be picked is that at this time the tower concrete will have been for almost 12 consecutive hours under absence of light. This absence of sunlight will therefore lead to lower temperature and lower strains due to it. Isolating the daily sample to a time when the temperature effect is minimal will help measure strains that derive from all the other factors that can cause it.

The full-time history of reduced strain and temperature dataset was plotted for the daily sample of 5 AM for each of the sensors. The generated plots are presented in **Figure 5.14**, **Figure 5.15**, **Figure 5.16** and **Figure 5.17**.

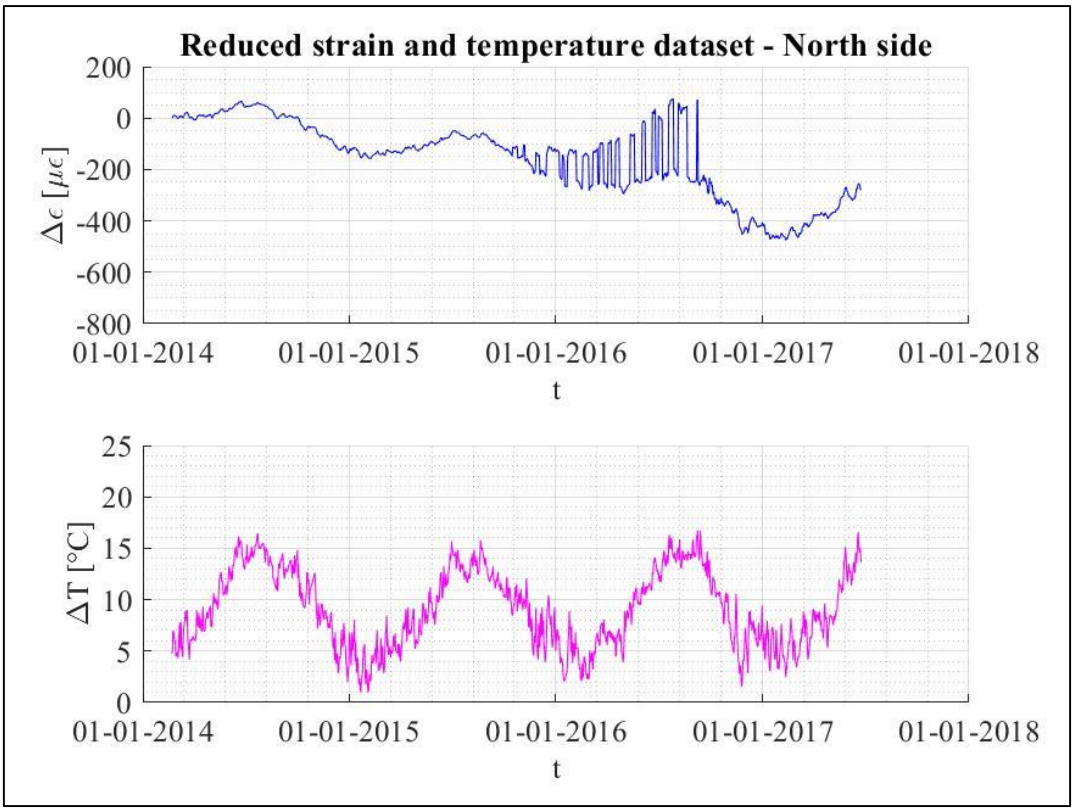

Figure 5.14. Reduced strain and temperature dataset from CT-OD7.5-S-STR-S-1194 (North side)

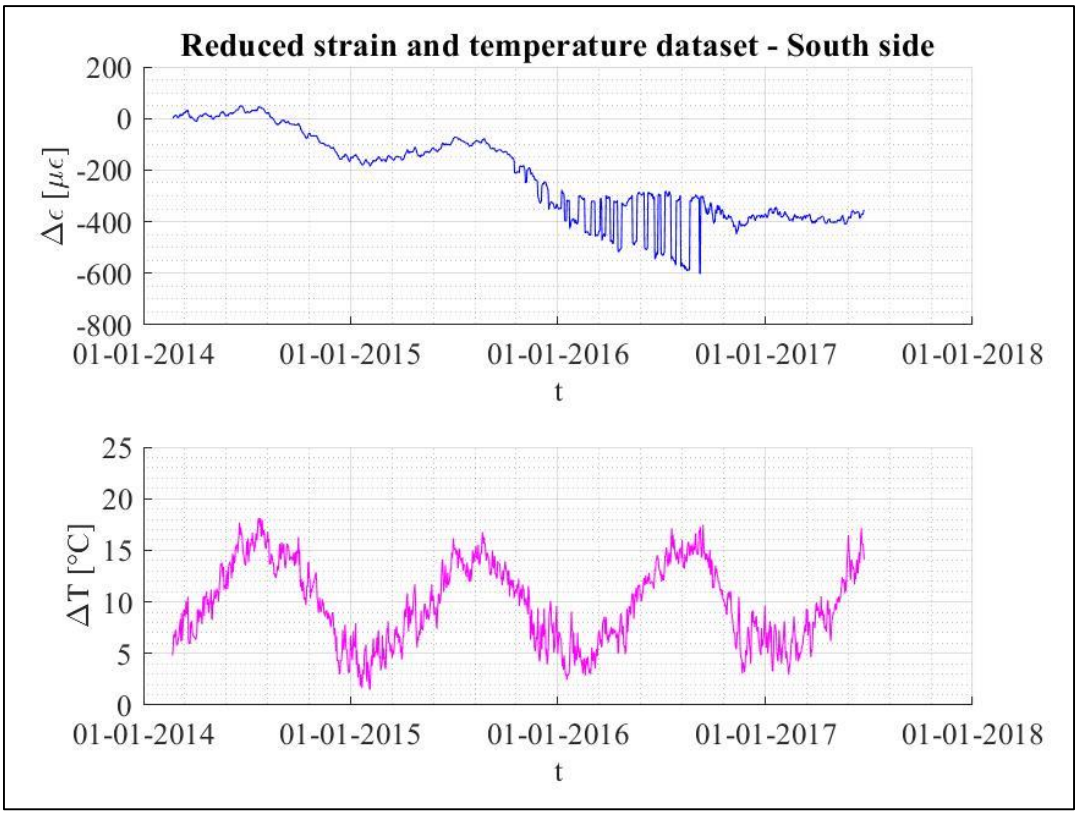

Figure 5.15. Reduced strain and temperature dataset from CT-OD7.5-S-STR-S-1198 (South side)

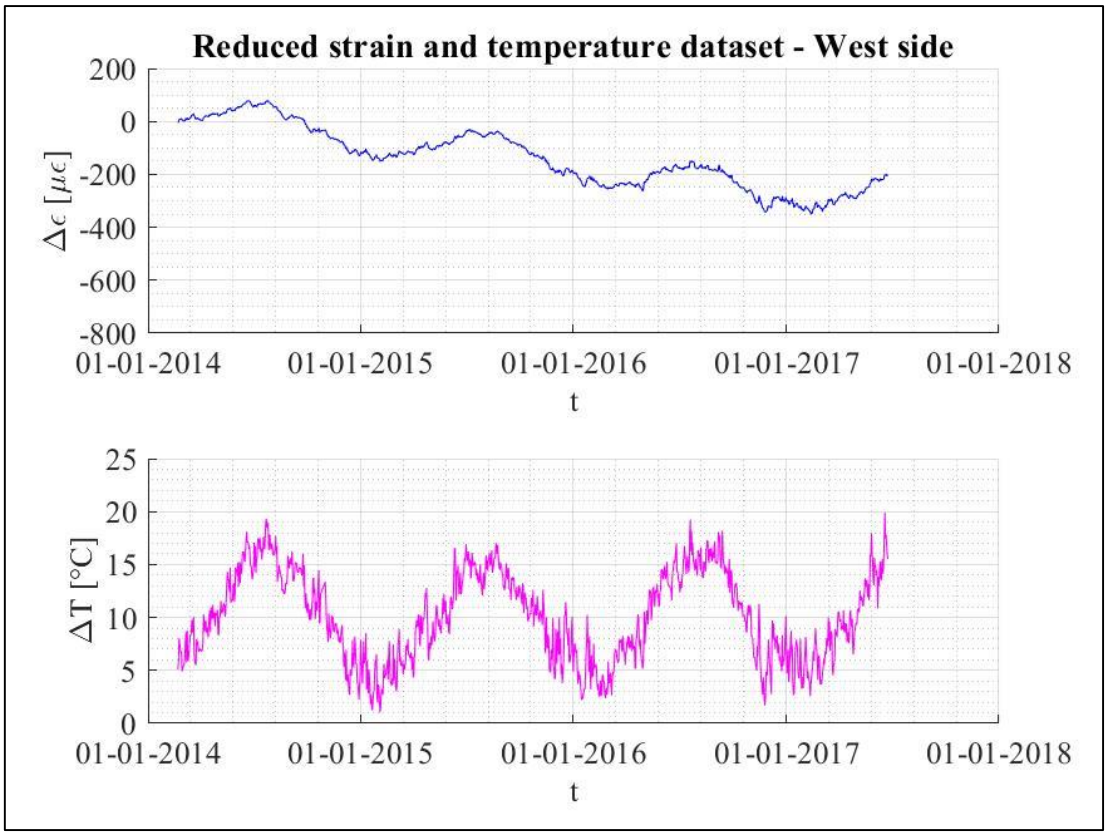

Figure 5.16. Reduced strain and temperature dataset from CT-OD7.5-S-STR-S-1192 (West side)

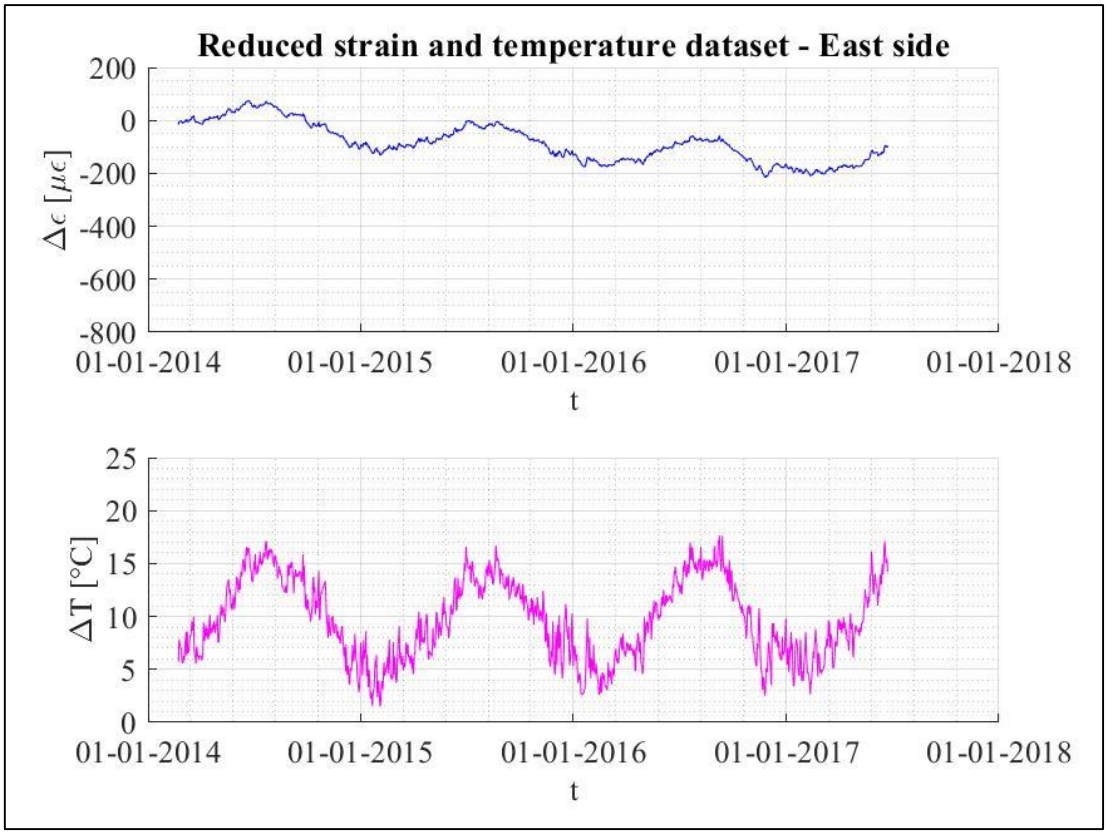

Figure 5.17. Reduced strain and temperature dataset from CT-OD7.5-S-STR-S-1196 (East side)

5.2.1 Results and discussion

Comparing the full-time history reduced strain plots to the full-time history uncompensated strain in **Figure 5.6**, **Figure 5.7**, **Figure 5.8** and **Figure 5.9**, we can instantly observe the almost identical pattern with which the two plots fluctuate; a pattern that appears to repeat itself in all three and a half years of measures. The similarity in the two patterns can be attributed to the contribution of the temperature to the strains generated in the concrete. Indeed, the temperature patterns follow the typical seasonal variation, so that the temperature reaches the maximum values during summer, while on the contrary it falls down in the winter.

Furthermore, if we focus on the overall strain change from the beginning of the observations to the end, it is clear that there is a constant decrease. This would be consequent to a contraction measured in the tower concrete. In order to understand the causes of this trend, it has been considered that concrete undergoes a natural contraction due to the sequential construction operations during the time period of observation. In particular, the increasing loading deriving firstly from the tower segments and, then, from deck segments lifting contributes to an increase of stress on the monitored section at the base of the tower.

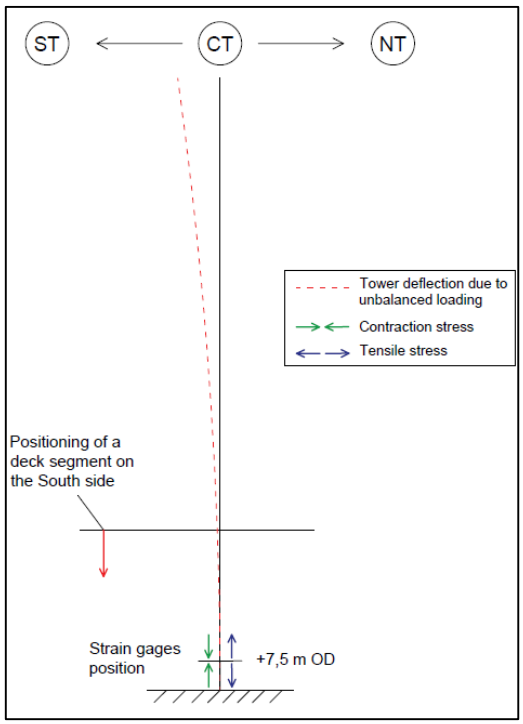

Figure 5.18. Simplified scheme representing the balance cantilevering construction

Moreover, the contribution of deformation due to creep and that due to the natural process of concrete shrinkage should be added to the elastic contraction.

As a consequence, it has been built a model for the interpretation of the dependence between the measured strain and each one of the influencing factors. Then, the two approaches (*LSA* and *Bayesian*) for parameters estimation have been used. In order to complete this task, the chronological order of the loading events (tower and deck segments lifting dates) and the weight of every segment was needed. While the exact dates of the segments lifting and the exact weight of the deck segments were known since they were provided as data on the bridge, the tower sections weight has been calculated by the author, using the information on the tower geometry. *Annex 2* report all the data needed and used for this task. Note that the parameters estimation has been carried out only on the CT. All the 8 sensors present on the section considered were analysed, in order to reach a more precise result.

6. Parametric model

The model employed for the interpretation of the dependence between the measured strain ε, the measured temperature T and other time-dependent variables is presented in the following equation:

$$\varepsilon(t) = \varepsilon_0 + \varepsilon_{el}(t) + \varepsilon_{cr}(t) + \varepsilon_{shr}(t) + \alpha T(t) = \\ = \varepsilon_0 + \frac{1}{E}\sigma(t) + \frac{\varphi_\infty}{E} C(t) + \varepsilon_{s,\infty}\beta_s(t) + \alpha T(t)$$

Where:

- ε(t) is the total deformation of the tower concrete;
- ε_0 is the strain value when T=0 and t=0, i.e. before the installation of the monitoring system;
- $\frac{1}{E}\sigma(t)$ is the elastic strain due to the loading;
- $\frac{\varphi_\infty}{E} C(t)$ is the creep deformation;
- $\varepsilon_{s,\infty}\beta_s(t)$ is the shrinkage contribution;
- $\alpha T(t)$ is the temperature correlated strain.

The zero of the deformation field should be measured. To achieve this, the variations in strain in respect of an unknown offset would be measured. Particularly, the first value recorded for the dataset would be subtracted from each subsequent quantity. With these considerations, our deformation model is re-written and becomes the following:

$$\Delta\varepsilon(t) = \varepsilon_0 + \frac{1}{E}\Delta\sigma(t) + \frac{\varphi_\infty}{E} C(t) + \varepsilon_{s,\infty}\beta_s(t) + \alpha\Delta T(t).$$

This parametric model is based on the knowledge of the time-dependent functions, while five parameters need to be determined using the already mentioned methods. These parameters are:

- ε_0, that is a sort of starting value of strain;
- $\frac{1}{E}$, where E is the modulus of elasticity of the concrete;
- $\frac{\varphi_\infty}{E}$, where φ_∞ is equal to the product of $\beta(f_{cm})$ and φ_{RH}, that are two factors defined in the Eurocode 2 (UNI-EN1992-1-1:2004), depending respectively on f_{cm} (the

mean concrete compressive strength at age of 28 days) and on the relative humidity (RH);

- $\varepsilon_{s,\infty}$, that is the strain due to shrinkage at time t=∞;
- α, that is an apparent thermal expansion coefficient, since it is not the real thermal expansion coefficient of the material, but it takes into account how strain changes because of the temperature T.

The four time-dependent functions are known. While the temperature ($\Delta T(t)$) is obviously known from measurements, the other three functions ($\sigma(t)$, $C(t)$ and $\beta_s(t)$) have been determined by calculation.

Each one of the calculations carried out to define these functions needs a detailed explanation.

6.1 Linear elastic strain

During the construction process, the tower section 2 (TS2), where the sensors are located and, so, whose strain they measure, experienced a state of progressive loading. Indeed, after about one month after the tower section in exam was cast, the second tower segment was poured onto it, representing the first load. Since then, all the other tower and deck segments were put in position, getting additional weight on TS2. All these loads represent a source of stress and, thus, according to Hooke's law, of deformation for the concrete section.

Please note that all the calculation has been carried out founding on the realistic assumption that the structure, composed firstly by the "growing" tower and then by the balanced cantilever, is isostatic. This allows to easily determine the forces at the base of the tower.

Therefore, the stresses experienced by TS2 in correspondence of the sensors have been determined using the well-known Navier formula:

$$\sigma = \frac{N}{A} \pm \frac{M}{J} y,$$

Where:

- *N* is the axial force of the added segments dead load;

- *A* is the section of the TS2;
- *M* is the bending moment generated by the unbalanced segments lifting;
- *J* is the moment of inertia of the section in the North-South direction (=1900 m^4);
- *y* is the distance between the sensors and the neutral axis, that coincides in this case with the West-East direction (see *5.1.2*).

During the first two years, tower construction operations occurred. In this case, stresses are only generated by the increasing axial force on TS2. Bending moment starts to be effective when deck segments lifting operations began, that is from October 2015. There are 8 different sensors with 3 different distance from the neutral axis y; the ones on the North side have an y=6,75 m, those on the South side have y=-6.75 m and those on the West and East sides are on the neutral axis, so y=0 m.

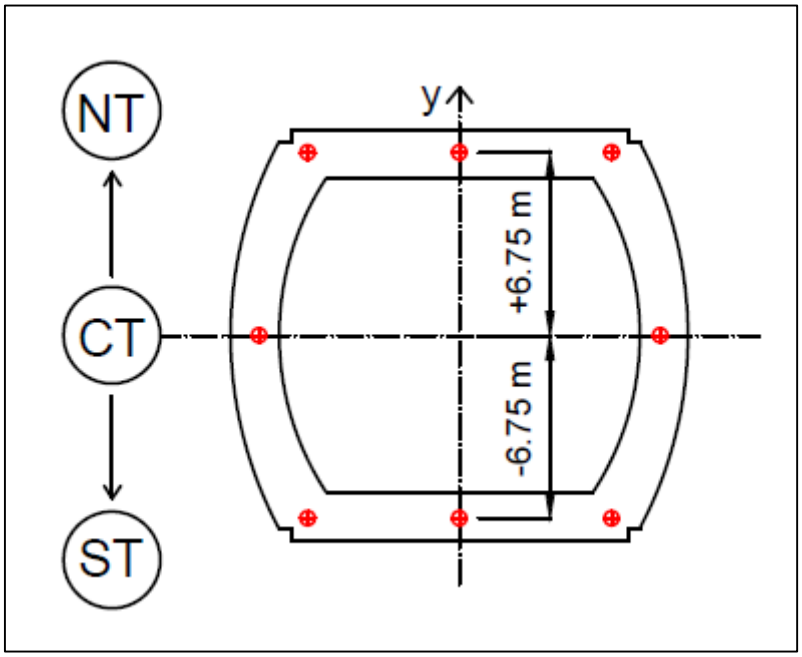

Figure 6.1. TS2 reference system for the calculation of the stresses

Due to this situation, three different stress functions were built, each of them related to the position of the sensors. Of course, they follow the same initial trend, since only tower segments were acting (no bending moment) until October 2015.

The author reminds the reader that the tower and deck segments lift data used to calculate the stresses at the base of the tower are reported in *Annex 2*. Following, the three final stress functions σ(t) are presented.

North side sensors

The three strain gages located on the North face of the tower are y=6.75 m away from the neutral axis.

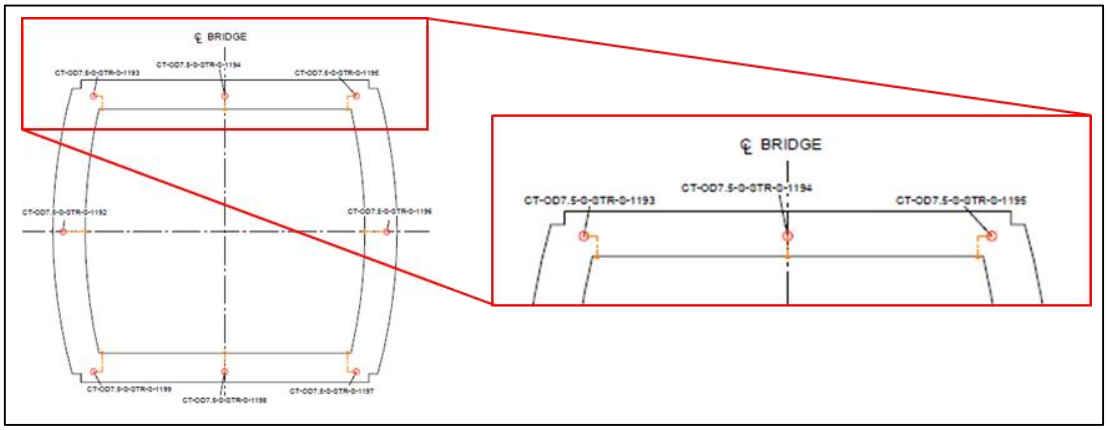

Figure 6.2. North side sensors position (CT-OD7.5-S-STR-S-1193/1194/1195)

The stress function related to the North sensors $\sigma_N(t)$ is represented in the following picture.

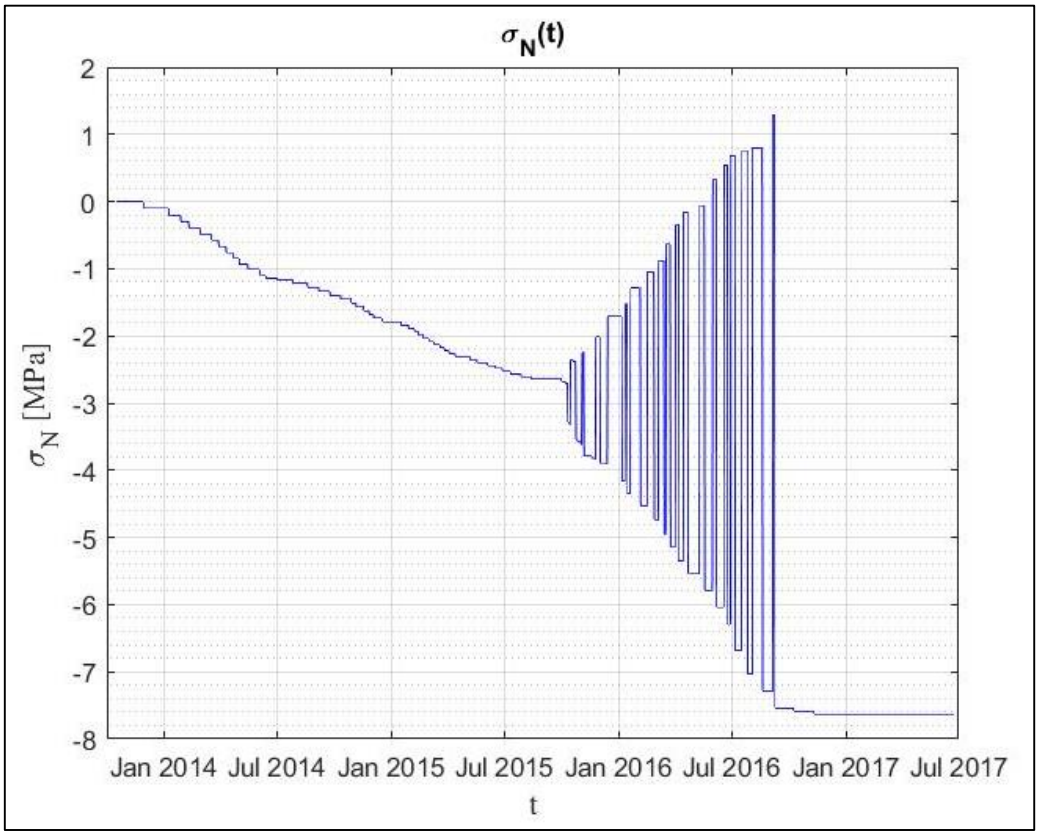

Figure 6.3. North sensors stress function $\sigma_N(t)$

South side sensors

The three strain gages located on the South face of the tower are y=-6.75 m away from the neutral axis.

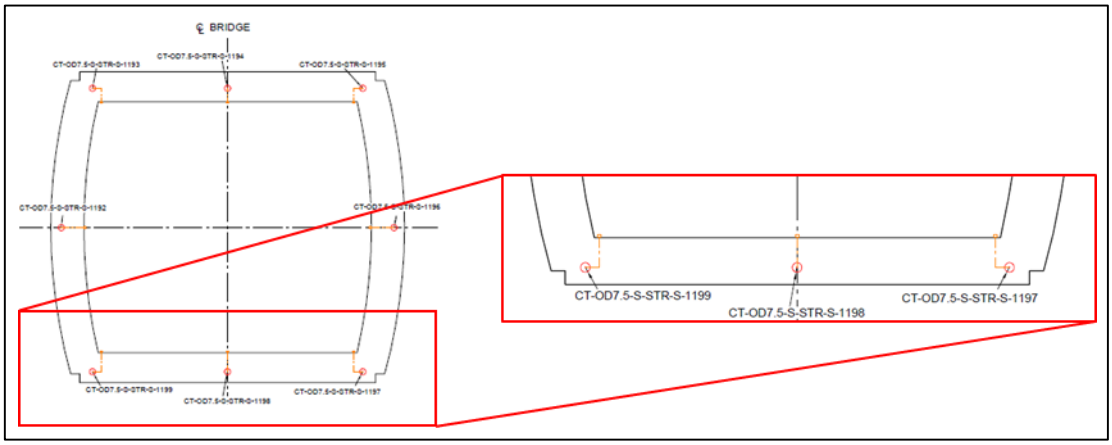

Figure 6.4. South side sensors position (CT-OD7.5-S-STR-S-1197/1198/1199)

The stress function related to the South sensors $\sigma_S(t)$ is represented in the following picture.

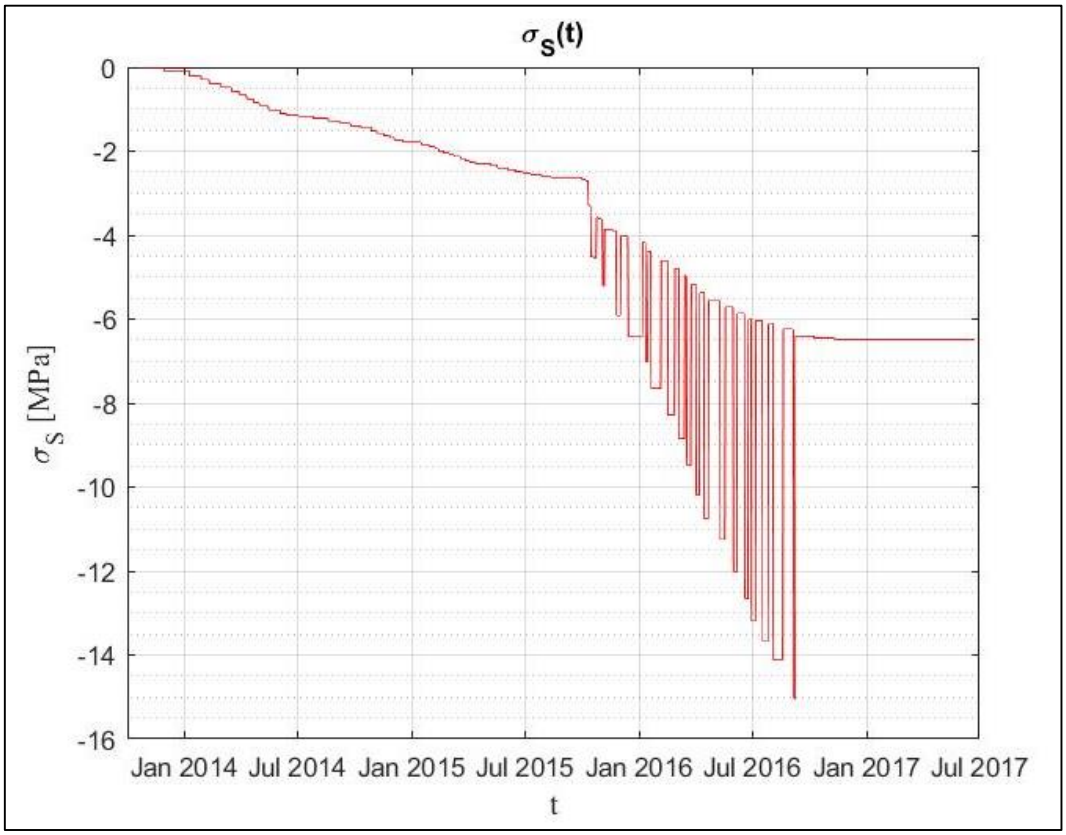

Figure 6.5. South sensors stress function $\sigma_S(t)$

West and East side sensors

The two strain gages located on the West and East faces of the tower are exactly on the neutral axis (y=0 m). Thus, they theoretically do not experience any bending moment.

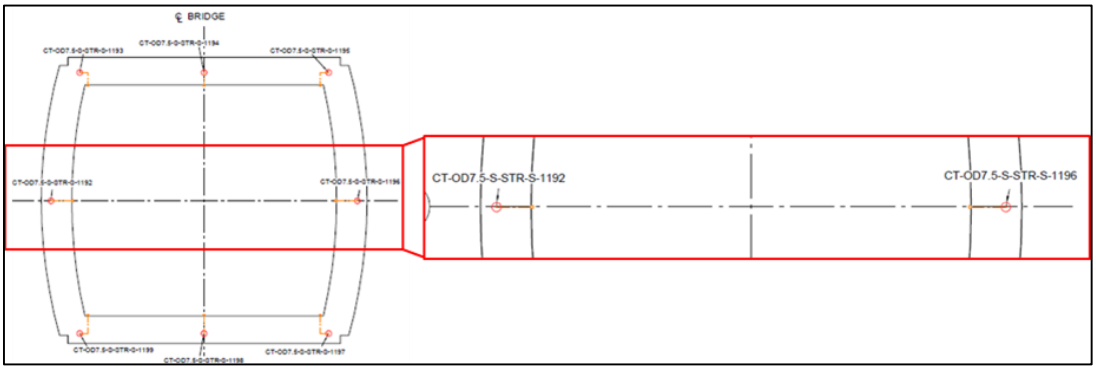

Figure 6.6. West and East side sensors position (CT-OD7.5-S-STR-S-1192/1196)

The stress function related to the West and East sensors $\sigma_{na}(t)$ is represented in the following picture.

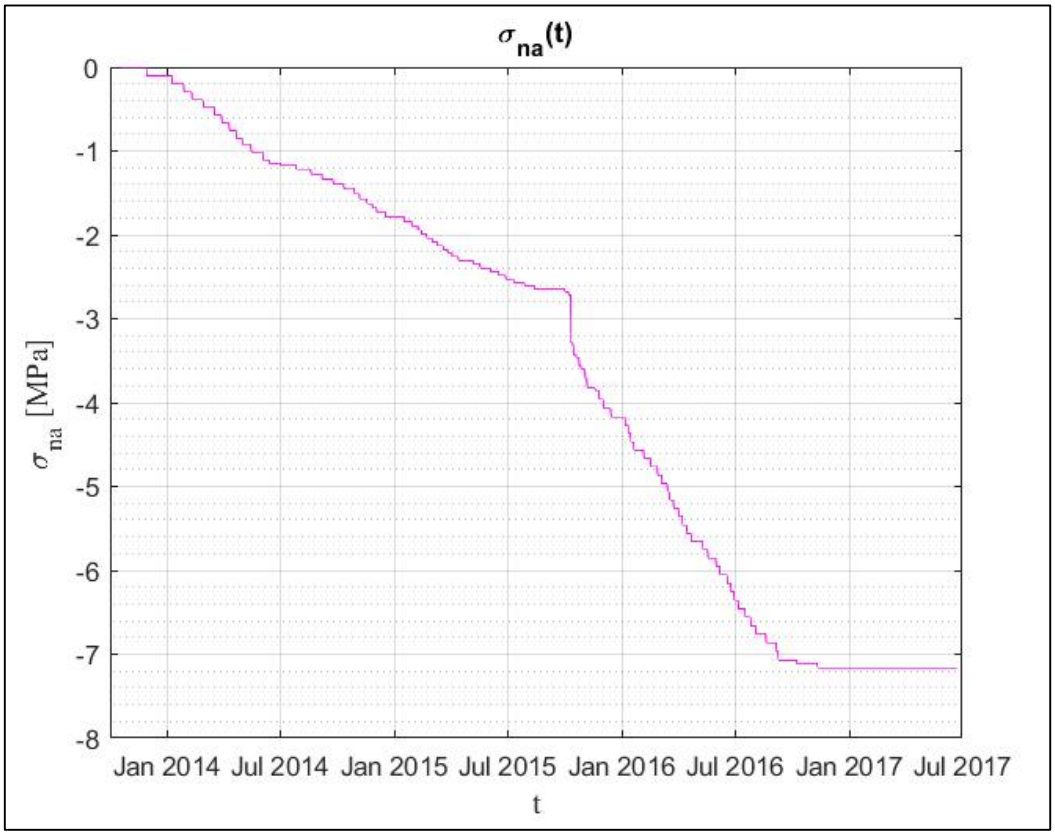

Figure 6.7. Neutral axis sensors stress function $\sigma_{na}(t)$

6.2 Creep

The creep contribution to the total deformation of the concrete has been studied and calculated as indicated on the Eurocodes. Following, a brief introduction and explanation of the creep theory is provided.

A concrete element subject to a constant state of stress (σ=cost.) will suffer an immediate deformation (the elastic one) plus a time-dependent one due to the viscous flow (creep). This second strain contribute is related to the amount of load applied through a creep function $\varphi(t,t_0)$, which is dependent on the age of the concrete at the loading (t_0): the younger the concrete at the time of loading, the greater the creep coefficient and therefore the viscous deformation. The behaviour can be easily described with the following image:

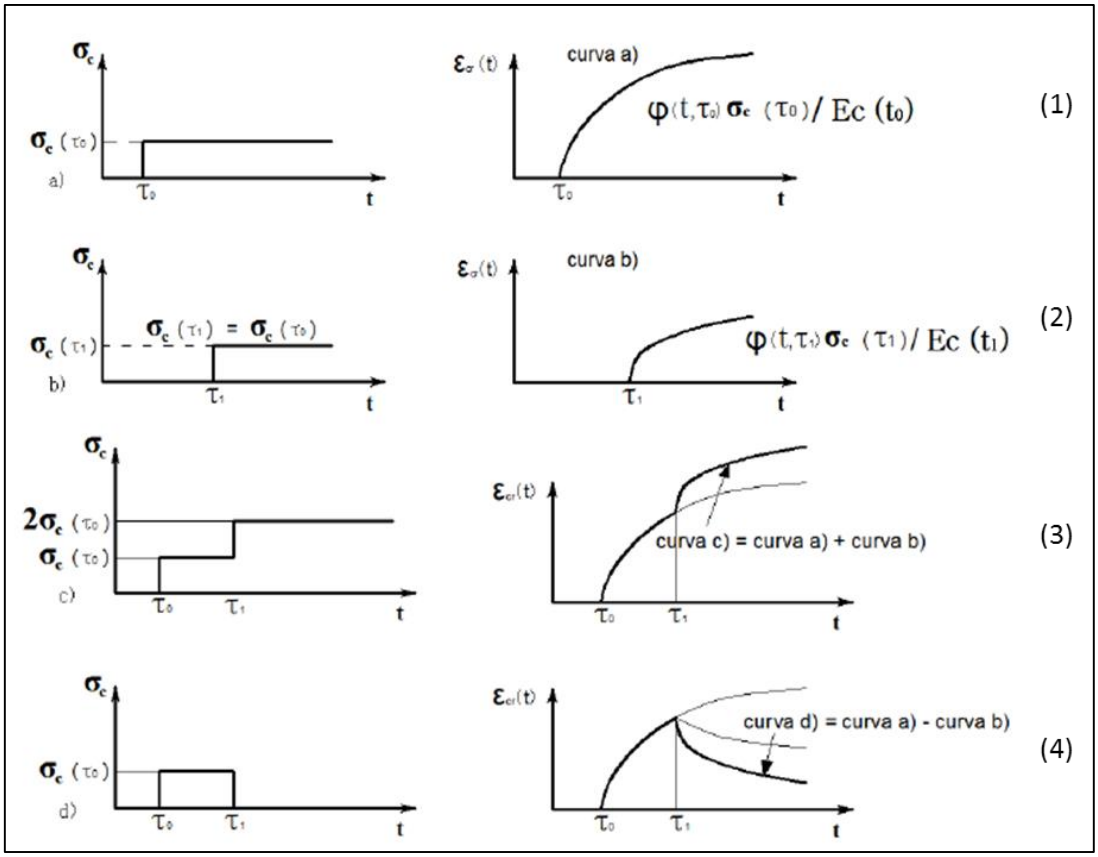

Figure 6.8. Creep deformation $\varepsilon_{cr}(t)$ is function of the loading time τ and of the stress state σ_c *(Monaco, 2012)*

Creep deformation is thus calculated as:

$$\varepsilon_{cr}(t) = \varepsilon_{el}\varphi(t,t_0) = \frac{\sigma_c(t_0)}{E}\varphi(t,t_0)$$

Eurocode 2 provides the following expression for the creep coefficient $\varphi(t,t_0)$, based on experimental results:

$$\varphi(t,t_0) = \varphi_{RH} \cdot \beta(f_{cm}) \cdot \beta(t_0) \cdot \beta_c(t,t_0),$$

where RH is the relative humidity of the environment and f_{cm} is the concrete mean compressive strength at 28 days. Each one of the factors that influence the creep coefficient is defined in Annex B of the Eurocode 2.

In the case in exam, TS2 is subjected to different loading steps at progressive times. It is therefore necessary to execute a convolution between the different creep deformations at different times. Therefore, the total creep deformation at time t is:

$$\varepsilon_{cr}(t) = \int \frac{\sigma_c(\tau)}{E} \cdot \varphi(t-\tau)d\tau = \int \frac{\sigma_c(\tau)}{E} \cdot \varphi_{RH} \cdot \beta(f_{cm}) \cdot \beta(\tau) \cdot \beta_c(t-\tau)d\tau =$$

$$= \frac{\varphi_{RH} \cdot \beta(f_{cm})}{E} \cdot \int \sigma_c(\tau) \cdot \beta(\tau) \cdot \beta_c(t-\tau)d\tau =$$

$$= \frac{\varphi_\infty}{E} \cdot \int \sigma_c(\tau) \cdot \beta(\tau) \cdot \beta_c(t-\tau)d\tau = \frac{\varphi_\infty}{E} \cdot C(t)$$

Now that the creep contribution is defined, fixing $\frac{\varphi_\infty}{E}$ as parameter to estimate, the function C(t) needs to be calculated. The stress function σ(t) is known (see *6.1*). The coefficients $\beta(t_0)$ and $\beta_c(t,t_0)$ have been calculated as described in Eurocode 2.

Finally, the function C(t) has been determined and plotted for each sensor position (since σ(t) is different for North, South and neutral axis positions).

North side sensors

The creep function for the North side sensors $C_N(t)$ is shown in the next figure.

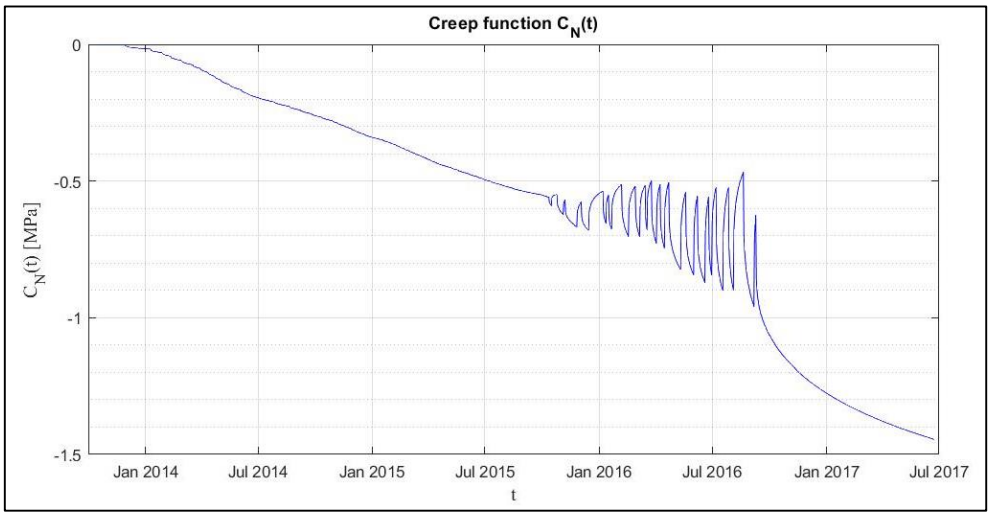

Figure 6.9. North sensors creep function $C_N(t)$

Following, a comparison between the elastic and the creep strain is depicted.

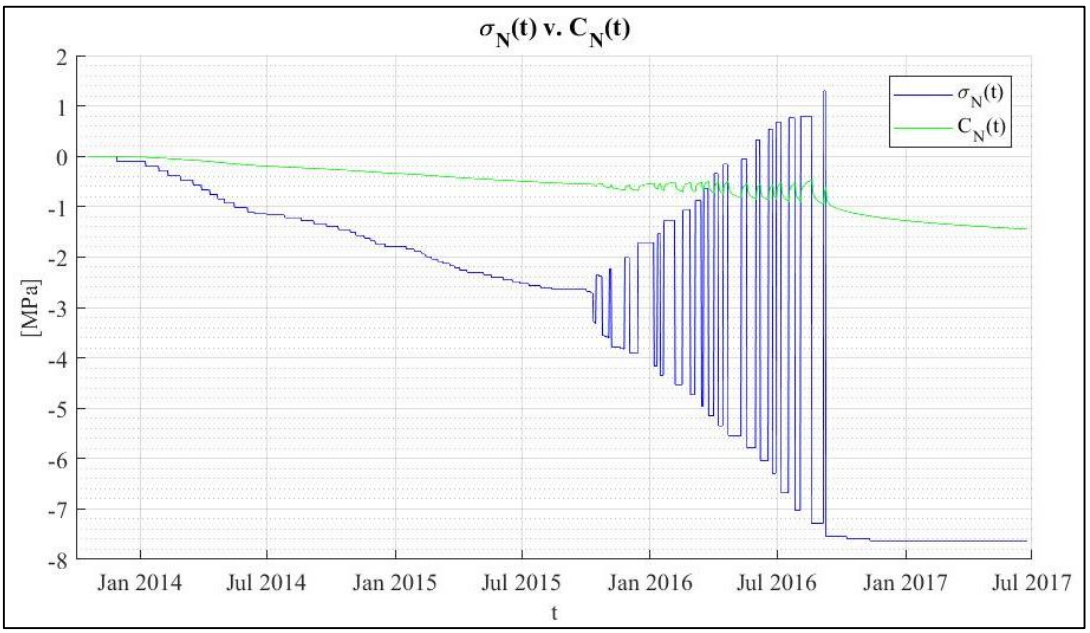

Figure 6.10. Comparison stress v. creep function – North

South side sensors

The creep function for the South side sensors $C_S(t)$ is shown in the next figure.

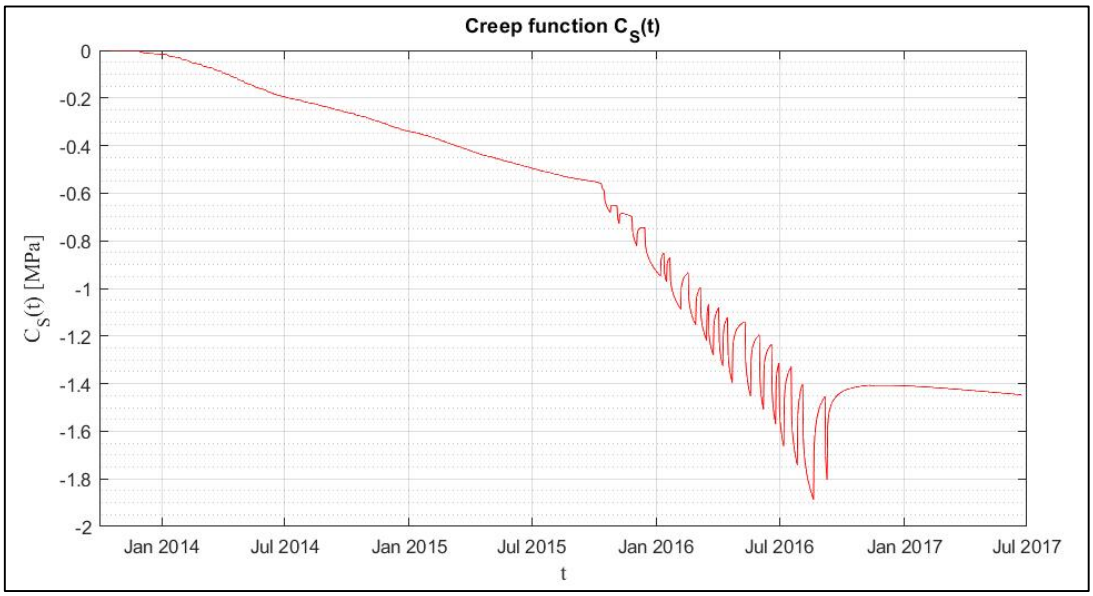

Figure 6.11. South sensors creep function $C_S(t)$

Following, a comparison between the elastic and the creep strain is depicted.

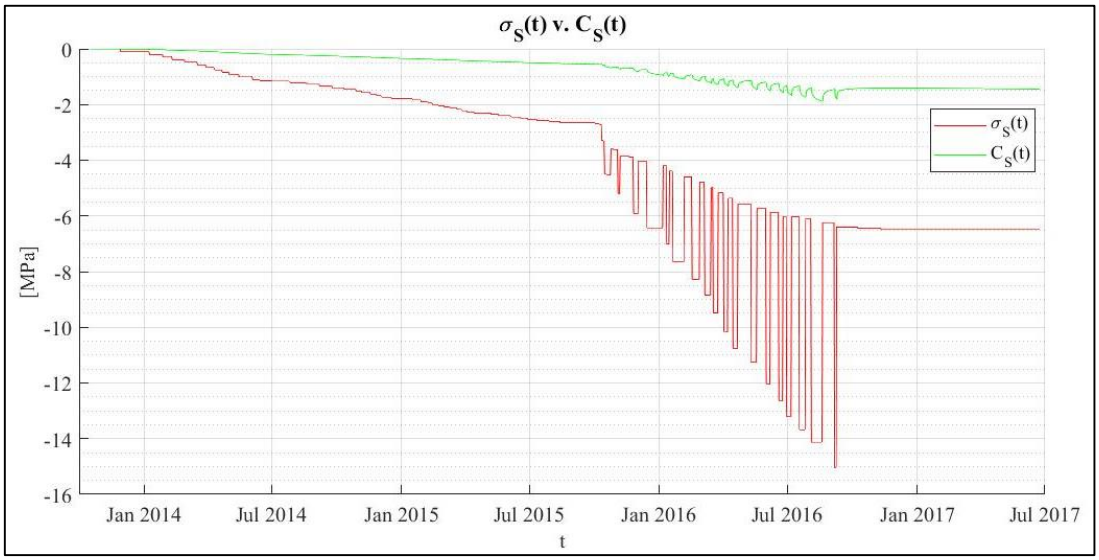

Figure 6.12. Comparison stress v. creep function – South

West and East side sensors

The creep function for the West and East side sensors $C_{na}(t)$ is shown in the next figure.

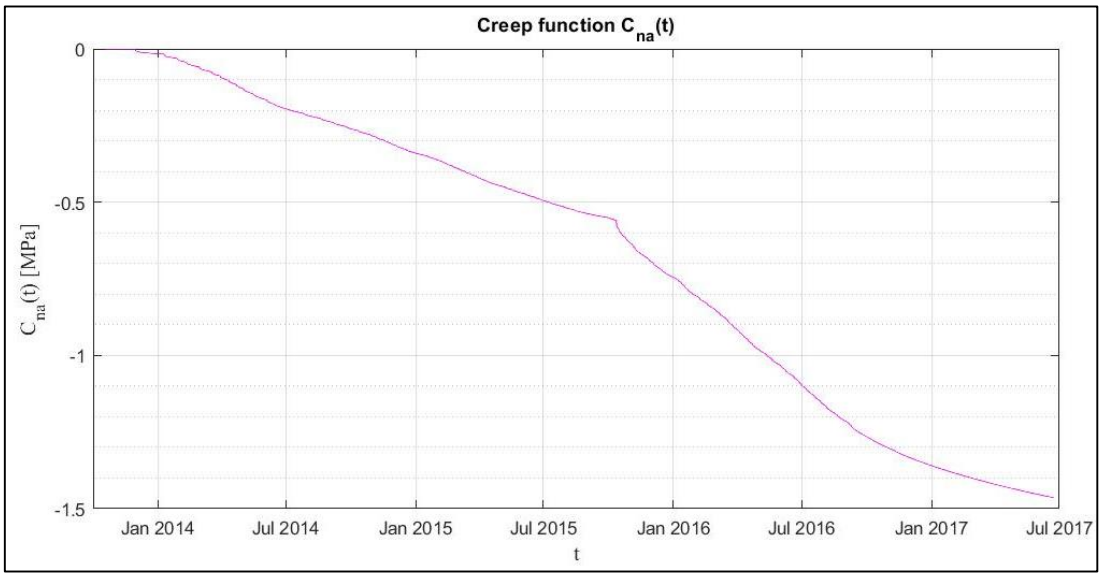

Figure 6.13. West and East sensors creep function $C_{na}(t)$

Following, a comparison between the elastic and the creep strain is depicted.

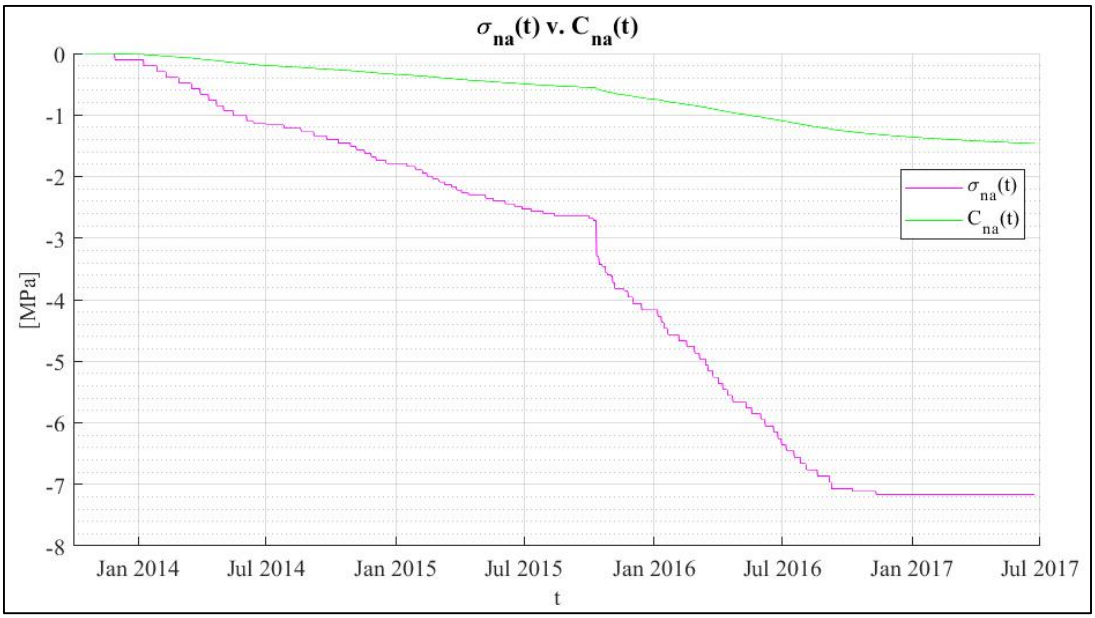

Figure 6.14. Comparison stress v. creep function – neutral axis

6.3 Shrinkage

The total shrinkage strain $\varepsilon_{cs}(t)$ is composed of two components, the drying shrinkage strain $\varepsilon_{cd}(t)$ and the autogenous shrinkage strain $\varepsilon_{ca}(t)$. The drying shrinkage strain develops slowly, since it is a function of the migration of the water through the hardened

concrete. The autogenous shrinkage strain develops during the hardening of the concrete: the major part therefore develops in the early days after casting. Autogenous shrinkage is a linear function of the concrete strength (EN 1992-1-1, 2004).

Since the measurements start about six months after TS2 concrete casting, only the drying shrinkage contribution has been taken into account for the parametric model, assuming that all the autogenous percentage of shrinkage was already spent at that time.

Hence, the drying shrinkage value follows from:

$$\varepsilon_{cd}(t) = k_h \cdot \varepsilon_{cd,0} \cdot \beta_{ds}(t, t_s) = \varepsilon_{s,\infty} \cdot \beta_{ds}(t, t_s)$$

where k_h and $\varepsilon_{cd,0}$ are defined in the Eurocode 2. The former coefficient depends on the notional size h0 according to the table:

h_0	k_h
100	1.0
200	0.85
300	0.75
≥ 500	0.70

Table 6.1. Values for k_h

$\varepsilon_{cd,0}$ is instead determined as follows:

$$\varepsilon_{cd,0} = 0{,}85\left[(220 + 110 \cdot \alpha_{ds1}) \cdot \exp\left(-\alpha_{ds2} \cdot \frac{f_{cm}}{f_{cmo}}\right)\right] \cdot 10^{-6} \cdot \beta_{RH}$$

$$\beta_{RH} = 1{,}55\left[1 - \left(\frac{RH}{RH_0}\right)^3\right]$$

where:

f_{cm} is the mean compressive strength (MPa)

f_{cmo} = 10 Mpa

α_{ds1} is a coefficient which depends on the type of cement (see 3.1.2 (6))
- = 3 for cement Class *S*
- = 4 for cement Class *N*
- = 6 for cement Class *R*

α_{ds2} is a coefficient which depends on the type of cement
- = 0,13 for cement Class *S*
- = 0,12 for cement Class *N*
- = 0,11 for cement Class *R*

RH is the ambient relative humidity (%)

RH_0 = 100%.

Figure 6.15. Calculation of the basic drying shrinkage strain according to *(EN 1992-1-1, 2004)*

Establishing $\varepsilon_{s,\infty}$ as parameter to estimate, the time-dependent coefficient $\beta_{ds}(t,t_s)$ has to be calculated as follows:

$$\beta_{ds}(t,t_s) = \frac{(t-t_s)}{(t-t_s)+0.04\sqrt{h_0{}^3}}$$

where:

- t is the age of the concrete at the moment considered, in days;
- t_s is the age of the concrete (days) at the beginning of drying shrinkage, which normally is at the end of curing; in this case it has been assumed equal to 7 days due to lack of knowledge;
- h_0 is the notional size (mm) of the cross-section (2Ac/u=2*75E6/100E3=1500 mm).

The function is shown in the next figure.

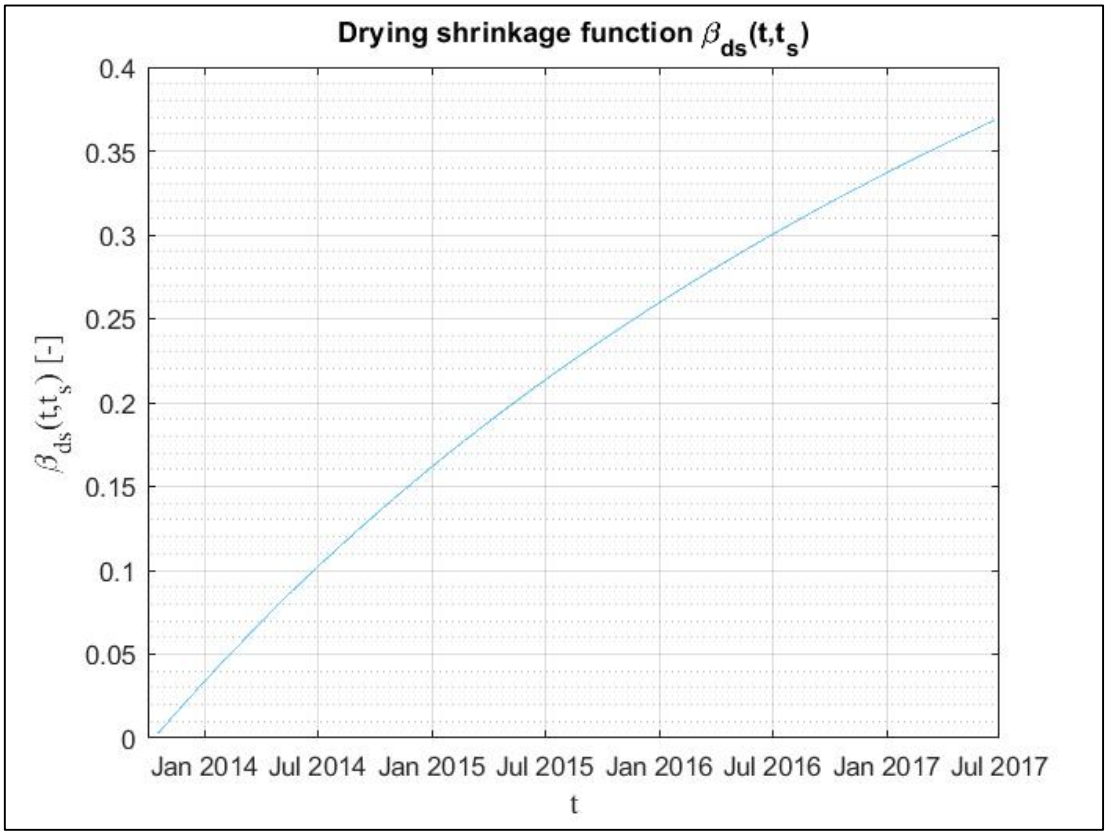

Figure 6.16. Drying shrinkage function $\beta_{ds}(t,t_s)$

7. Parameters estimation

In this section, the results of the parameters estimation obtained applying the two above mentioned methods will be illustrated and discussed.

7.1 Parameters estimation using Least Squares Analysis

Defined the parametric model $f(x_i, \theta) = \varepsilon = \varepsilon_0 + \frac{1}{E}\sigma(t) + \frac{\varphi_\infty}{E}C(t) + \varepsilon_{s,\infty}\beta_s(t) + \alpha T(t)$, we can establish that:

$$\boldsymbol{y} = \boldsymbol{\Delta\varepsilon_i} = \begin{bmatrix} \varepsilon_1 - \varepsilon_1 \\ \vdots \\ \varepsilon_i - \varepsilon_1 \\ \vdots \\ \varepsilon_N - \varepsilon_1 \end{bmatrix}, \quad \boldsymbol{\theta} = \begin{bmatrix} \varepsilon_0 \\ \frac{1}{E} \\ \frac{\varphi_\infty}{E} \\ \varepsilon_{s,\infty} \\ \alpha \end{bmatrix}, \quad \boldsymbol{D} = \begin{bmatrix} 1 & \Delta\sigma_1 & \Delta C_1 & \Delta\beta_{s,1} & \Delta T_1 \\ \vdots & \vdots & \vdots & \vdots & \vdots \\ 1 & \Delta\sigma_i & \Delta C_i & \Delta\beta_{s,i} & \Delta T_i \\ \vdots & \vdots & \vdots & \vdots & \vdots \\ 1 & \Delta\sigma_N & \Delta C_N & \Delta\beta_{s,N} & \Delta T_N \end{bmatrix}$$

Following the expressions mentioned in *4.3*, the parameters vector $\boldsymbol{\theta}$ has been evaluated for each of the eight sensors analysed.

A brief explanation of the units of measure is needed. The strain is measured in microstrain με (that is 10^{-6}), so ε_0 is in με too, as well as $\varepsilon_{s,\infty}$, which multiply non-dimensional numbers. On the contrary, since $\sigma(t)$ and $C(t)$ are calculated in MPa, the parameters $\frac{1}{E}$ and $\frac{\varphi_\infty}{E}$ will be in MPaE-6. Finally, the temperature T is measured in °C, so α will be in με/°C.

North side sensors

The parameters values together with the covariance matrix and the Pearson's correlations estimated from the sensors on the North face of the CT have been reported below.

1) North

Sensor (location)	ε_0 [με]	1/E [1/MPaE6]	ϕ_∞/E [1/MPaE6]	$\varepsilon_{s,\infty}$ [με]	α [με/°C]
CT-OD7.5-S-STR-S-1194 (North)	13	20,47	99,43	-139	12,49

Table 7.1. CT-OD7.5-S-STR-S-1194 (North) LSA parameters estimated values

Covariance matrix:

	ε_0	1/E	ϕ_∞/E	$\varepsilon_{s,\infty}$	α
ε_0	10,4247	0,4738	-7,4768	-63,8574	-0,1376
1/E	0,4738	0,5373	-2,3322	-3,6206	0,0022
ϕ_∞/E	-7,4768	-2,3322	18,6336	74,8267	-0,0726
$\varepsilon_{s,\infty}$	-63,8574	-3,6206	74,8267	531,9863	-0,2558
α	-0,1376	0,0022	-0,0726	-0,2558	0,0567

Std[ε_0] [με]	Std[1/E] [1/MPaE6]	Std[ϕ_∞/E] [1/MPaE6]	Std[$\varepsilon_{s,\infty}$] [με]	Std[α] [με/°C]
3	0,73	4,32	23	0,24

Pearson's correlation:

	ε_0	1/E	ϕ_∞/E	$\varepsilon_{s,\infty}$	α
ε_0	1	0,2002	-0,5365	-0,8575	-0,1790
1/E	0,2002	1	-0,7370	-0,2141	0,0128
ϕ_∞/E	-0,5365	-0,7370	1	0,7515	-0,0706
$\varepsilon_{s,\infty}$	-0,8575	-0,2141	0,7515	1	-0,0466
α	-0,1790	0,0128	-0,0706	-0,0466	1

From the estimated parameters we can calculate:

- E=48841 MPa;
- φ_∞=4,86.

2) North-West

Sensor (location)	ε_0 [με]	1/E [1/MPaE6]	ϕ_∞/E [1/MPaE6]	$\varepsilon_{s,\infty}$ [με]	α [με/°C]
CT-OD7.5-S-STR-S-1192 (North-West)	-14	17,23	87,07	-250	12,72

Table 7.2. CT-OD7.5-S-STR-S-1192 (North-West) LSA parameters estimated values

Covariance matrix:

	ε_0	1/E	ϕ_∞/E	$\varepsilon_{s,\infty}$	α
ε_0	9,2822	0,3968	-6,1407	-52,9814	-0,2037
1/E	0,3968	0,4608	-1,9987	-3,0834	0,0011
ϕ_∞/E	-6,1407	-1,9987	15,9502	63,7134	-0,0499
$\varepsilon_{s,\infty}$	-52,9814	-3,0834	63,7134	451,1738	-0,1525
α	-0,2037	0,0011	-0,0499	-0,1525	0,0438

Std[ε_0] [με]	Std[1/E] [1/MPaE6]	Std[ϕ_∞/E] [1/MPaE6]	Std[$\varepsilon_{s,\infty}$] [με]	Std[α] [με/°C]
3	0,69	3,99	21	0,21

Pearson's correlation:

	ε_0	1/E	ϕ_∞/E	$\varepsilon_{s,\infty}$	α
ε_0	1	0,1919	-0,5047	-0,8187	-0,3196
1/E	0,1919	1	-0,7372	-0,2138	0,0076
ϕ_∞/E	-0,5047	-0,7372	1	0,7511	-0,0597
$\varepsilon_{s,\infty}$	-0,8187	-0,2138	0,7511	1	-0,0343
α	-0,3196	0,0076	-0,0597	-0,0343	1

From the estimated parameters, we can calculate:

- E=58022 MPa;
- φ_∞=5,05.

3) North-East

Sensor (location)	ε_0 [με]	1/E [1/MPaE6]	ϕ_∞/E [1/MPaE6]	$\varepsilon_{s,\infty}$ [με]	α [με/°C]
CT-OD7.5-S-STR-S-1195 (North-East)	-23	14,91	90,42	-65	13,05

Table 7.3. CT-OD7.5-S-STR-S-1195 (North-East) LSA parameters estimated values

Covariance matrix:

	ε_0	1/E	ϕ_∞/E	$\varepsilon_{s,\infty}$	α
ε_0	6,5406	0,2797	-4,3372	-37,4970	-0,1414
1/E	0,2797	0,3266	-1,4173	-2,1874	0,0011
ϕ_∞/E	-4,3372	-1,4173	11,3167	45,1973	-0,0402
$\varepsilon_{s,\infty}$	-37,4970	-2,1874	45,1973	319,9191	-0,1251
α	-0,1414	0,0011	-0,0402	-0,1251	0,0316

Std[ε_0] [με]	Std[1/E] [1/MPaE6]	Std[ϕ_∞/E] [1/MPaE6]	Std[$\varepsilon_{s,\infty}$] [με]	Std[α] [με/°C]
3	0,57	3,36	18	0,18

Pearson's correlation:

	ε_0	1/E	ϕ_∞/E	$\varepsilon_{s,\infty}$	α
ε_0	1	0,1914	-0,5041	-0,8197	-0,3112
1/E	0,1914	1	-0,7371	-0,2140	0,0112
ϕ_∞/E	-0,5041	-0,7371	1	0,7512	-0,0673
$\varepsilon_{s,\infty}$	-0,8197	-0,2140	0,7512	1	-0,0394
α	-0,3112	0,0112	-0,0673	-0,0394	1

From the estimated parameters, we can calculate:

- E=67061 MPa;
- φ_∞=6,06.

South side sensors

The parameters values together with the covariance matrix and the Pearson's correlations estimated from the sensors on the South face of the CT have been reported below.

1) South

Sensor (location)	ε_0 [με]	1/E [1/MPaE6]	ϕ_∞/E [1/MPaE6]	$\varepsilon_{s,\infty}$ [με]	α [με/°C]
CT-OD7.5-S-STR-S-1198 (South)	19	23,42	70,38	-333	9,08

Table 7.4. CT-OD7.5-S-STR-S-1198 (South) LSA parameters estimated values

Covariance matrix:

	ε_0	1/E	ϕ_∞/E	$\varepsilon_{s,\infty}$	α
ε_0	15,0643	0,7496	-10,9299	-102,7861	-0,3285
1/E	0,7496	0,4293	-1,8227	-4,8977	-0,0065
ϕ_∞/E	-10,9299	-1,8227	16,2554	98,7827	0,1476
$\varepsilon_{s,\infty}$	-102,7861	-4,8977	98,7827	867,7207	1,4570
α	-0,3285	-0,0065	0,1476	1,4570	0,0552

Std[ε_0] [με]	Std[1/E] [1/MPaE6]	Std[ϕ_∞/E] [1/MPaE6]	Std[$\varepsilon_{s,\infty}$] [με]	Std[α] [με/°C]
4	0,66	4,03	29	0,23

Pearson's correlation:

	ε_0	1/E	ϕ_∞/E	$\varepsilon_{s,\infty}$	α
ε_0	1	0,2948	-0,6985	-0,8990	-0,3602
1/E	0,2948	1	-0,6900	-0,2538	-0,0425
ϕ_∞/E	-0,6985	-0,6900	1	0,8317	0,1558
$\varepsilon_{s,\infty}$	-0,8990	-0,2538	0,8317	1	0,2105
α	-0,3602	-0,0425	0,1558	0,2105	1

From the estimated parameters we can calculate:

- E=42691 MPa;
- φ_∞=3,00.

2) South-East

Sensor (location)	ε_0 [με]	1/E [1/MPaE6]	ϕ_∞/E [1/MPaE6]	$\varepsilon_{s,\infty}$ [με]	α [με/°C]
CT-OD7.5-S-STR-S-1197 (South-East)	-9	20,73	63,85	-258	9,60

Table 7.5. CT-OD7.5-S-STR-S-1197 (South-East) LSA parameters estimated values

Covariance matrix:

	ε_0	1/E	ϕ_∞/E	$\varepsilon_{s,\infty}$	α
ε_0	14,4781	0,6586	-9,7770	-92,1540	-0,3756
1/E	0,6586	0,3763	-1,5946	-4,2579	-0,0045
ϕ_∞/E	-9,7770	-1,5946	14,2204	86,3184	0,1211
$\varepsilon_{s,\infty}$	-92,1540	-4,2579	86,3184	758,2787	1,2115
α	-0,3756	-0,0045	0,1211	1,2115	0,0473

Std[ε_0] [με]	Std[1/E] [1/MPaE6]	Std[ϕ_∞/E] [1/MPaE6]	Std[$\varepsilon_{s,\infty}$] [με]	Std[α] [με/°C]
4	0,61	3,78	28	0,22

Pearson's correlation:

	ε_0	1/E	ϕ_∞/E	$\varepsilon_{s,\infty}$	α
ε_0	1	0,2822	-0,6814	-0,8795	-0,4537
1/E	0,2822	1	-0,6894	-0,2521	-0,0334
ϕ_∞/E	-0,6814	-0,6894	1	0,8313	0,1477
$\varepsilon_{s,\infty}$	-0,8795	-0,2521	0,8313	1	0,2022
α	-0,4537	-0,0334	0,1477	0,2022	1

From the estimated parameters, we can calculate:

- E=48245 MPa;
- φ_∞=3,08.

3)South-West

Sensor (location)	ε_0 [με]	1/E [1/MPaE6]	ϕ_∞/E [1/MPaE6]	$\varepsilon_{s,\infty}$ [με]	α [με/°C]
CT-OD7.5-S-STR-S-1199 (South-West)	6	22,27	54,87	-319	9,50

Table 7.6. CT-OD7.5-S-STR-S-1199 (South-West) LSA parameters estimated values

Covariance matrix:

	ε_0	1/E	ϕ_∞/E	$\varepsilon_{s,\infty}$	α
ε_0	14,5836	0,6599	-9,8459	-93,0120	-0,3542
1/E	0,6599	0,3786	-1,6037	-4,2779	-0,0038
ϕ_∞/E	-9,8459	-1,6037	14,3132	86,9607	0,1146
$\varepsilon_{s,\infty}$	-93,0120	-4,2779	86,9607	764,7131	1,1695
α	-0,3542	-0,0038	0,1146	1,1695	0,0416

Std[ε_0] [με]	Std[1/E] [1/MPaE6]	Std[ϕ_∞/E] [1/MPaE6]	Std[$\varepsilon_{s,\infty}$] [με]	Std[α] [με/°C]
4	0,61	3,78	28	0,20

Pearson's correlation:

	ε_0	1/E	ϕ_∞/E	$\varepsilon_{s,\infty}$	α
ε_0	1	0,2808	-0,6815	-0,8808	-0,4546
1/E	0,2808	1	-0,6890	-0,2514	-0,0306
ϕ_∞/E	-0,6815	-0,6890	1	0,8312	0,1484
$\varepsilon_{s,\infty}$	-0,8808	-0,2514	0,8312	1	0,2073
α	-0,4546	-0,0306	0,1484	0,2073	1

From the estimated parameters, we can calculate:

- E=44894 MPa;
- φ_∞=2,46.

West and East sensors

1) West

Sensor (location)	ε_0 [με]	1/E [1/MPaE6]	ϕ_∞/E [1/MPaE6]	$\varepsilon_{s,\infty}$ [με]	α [με/°C]
CT-OD7.5-S-STR-S-1192 (West)	35	21,84	-10,32	-640	10,69

Table 7.7. CT-OD7.5-S-STR-S-1192 (West) LSA parameters estimated values

Covariance matrix:

	ε_0	1/E	ϕ_∞/E	$\varepsilon_{s,\infty}$	α
ε_0	3,5492	0,1644	-3,1057	-25,4729	-0,0580
1/E	0,1644	1,7290	-4,7273	6,1108	0,0014
ϕ_∞/E	-3,1057	-4,7273	16,2008	10,1479	0,0076
$\varepsilon_{s,\infty}$	-25,4729	6,1108	10,1479	259,4135	0,1335
α	-0,0580	0,0014	0,0076	0,1335	0,0082

Std[ε_0] [με]	Std[1/E] [1/MPaE6]	Std[ϕ_∞/E] [1/MPaE6]	Std[$\varepsilon_{s,\infty}$] [με]	Std[α] [με/°C]
2	1,31	4,02	16	0,09

Pearson's correlation:

	ε_0	1/E	ϕ_∞/E	$\varepsilon_{s,\infty}$	α
ε_0	1	0,0664	-0,4096	-0,8395	-0,3399
1/E	0,0664	1	-0,8932	0,2885	0,0119
ϕ_∞/E	-0,4096	-0,8932	1	0,1565	0,0208
$\varepsilon_{s,\infty}$	-0,8395	0,2885	0,1565	1	0,0916
α	-0,3399	0,0119	0,0208	0,0916	1

From the estimated parameters, we can calculate:

- E=45778 MPa;
- φ_∞=-0.47.

2) East

Sensor (location)	ε_0 [με]	1/E [1/MPaE6]	ϕ_∞/E [1/MPaE6]	$\varepsilon_{s,\infty}$ [με]	α [με/°C]
CT-OD7.5-S-STR-S-1196 (East)	41	6,19	-8,39	-534	10,86

Table 7.8. CT-OD7.5-S-STR-S-1192 (East) LSA parameters estimated values

Covariance matrix:

	ε_0	1/E	ϕ_∞/E	$\varepsilon_{s,\infty}$	α
ε_0	1,9926	0,1021	-1,8848	-15,3588	-0,0205
1/E	0,1021	1,0607	-2,8994	3,7566	0,0015
ϕ_∞/E	-1,8848	-2,8994	9,9351	6,2083	0,0039
$\varepsilon_{s,\infty}$	-15,3588	3,7566	6,2083	159,2495	0,0960
α	-0,0205	0,0015	0,0039	0,0960	0,0063

Std[ε_0] [με]	Std[1/E] [1/MPaE6]	Std[ϕ_∞/E] [1/MPaE6]	Std[$\varepsilon_{s,\infty}$] [με]	Std[α] [με/°C]
1	1,03	3,15	13	0,08

Pearson's correlation:

	ε_0	1/E	ϕ_∞/E	$\varepsilon_{s,\infty}$	α
ε_0	1	0,0703	-0,4236	-0,8622	-0,1836
1/E	0,0703	1	-0,8932	0,2890	0,0181
ϕ_∞/E	-0,4236	-0,8932	1	0,1561	0,0156
$\varepsilon_{s,\infty}$	-0,8622	0,2890	0,1561	1	0,0961
α	-0,1836	0,0181	0,0156	0,0961	1

From the estimated parameters, we can calculate:

- E=161550 MPa;
- φ_∞=-1,36.

Summary

	ε_0[με]	E [MPa]	φ_∞ [-]	$\varepsilon_{s,\infty}$ [με]	α [με/°C]
NORTH	13	48841	4,86	-139	12,49
NORTH-WEST	-14	58022	5,05	-250	12,72
NORTH-EAST	-23	67061	6,06	-65	13,05
SOUTH	19	42691	3,00	-333	9,08
SOUTH-WEST	6	44894	2,46	-319	9,50
SOUTH-EAST	-9	48245	3,08	-258	9,60
WEST	35	45778	-0,47	-640	10,69
EAST	41	161550	-1,36	-534	10,86

Table 7.9. LSA parameters estimated values

7.1.1 Results discussion

LSA was performed to estimate the values of the parameters using the strain data from every single strain gage located on TS2. Observing the results, it is clear that the method proves to be inappropriate for the purposes intended.

Firstly, the values that come out of the estimation process are almost all different from the expected ones. In particular way, there is a clear uncertainty between the stress and creep functions. Indeed, the process tends to confuse the two functions because of their dependency, as C(t) is function of σ(t) (see *6.2*). The effect of this indetermination problem is exactly the underestimation of the parameter *1/E* and the overestimation of the parameter φ_∞/E. As a consequence, the modulus of elasticity results to be higher than expected, as well as the creep coefficient. In other words, the LSA tends to reduce the difference between the two functions, decreasing the elastic contribution and, at the same time, increasing the creep one. This behaviour is clearly represented in **Figure 7.1**.

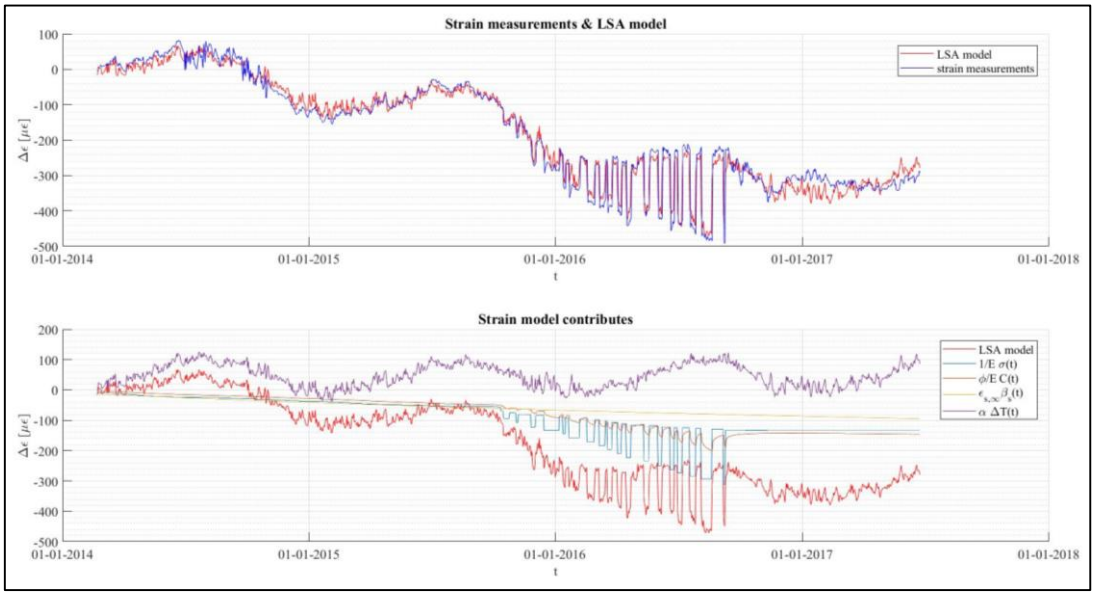

Figure 7.1. LSA estimated model

In the first graph, the strain measurements are plotted together with the model that comes out of the LSA application. In the second graph, every single contribution to the model has been plotted. From this second picture, it is clear how the elastic (blue) and creep (orange) contributions tend to be confused: the order of magnitude of the elastic and creep strain seems to be comparable, that is not realistic as the former one should be higher than the other one.

This issue is even more highlighted if we consider the two strain gages on the neutral axis (West and East sensors). In this case, it can be observed that the creep coefficient is negative, so that the creep contribution would be a tensile one, according to the model. This effect would be compensated by a very high value of the shrinkage strain. The East sensor data show a further weird value of the modulus of elasticity. The problem here should be related to the very smaller value of strain variation measured by this sensor over the period considered. If you observe the full-time histories of the uncompensated strain measured by every sensor of the CT (**Figure 5.6-Figure 5.9**), you can notice that the East sensor is the only one that measures an overall change in strain (considering 3 years from the beginning) of about 200 με. All the other strain gages show a variation of about 400 με. We can therefore simply state that the measurements of the East sensor are not reliable.

Another important feature that we can point out from the LSA application results is that the estimated value of the thermal coefficient α is a realistic value for each sensor data. This is due to the complete knowledge of the temperature throughout the whole period of observation. As a consequence, the relationship between strain and temperature is well understood by the estimation process. However it is interesting to note that the estimated α value is similar according to the position of the sensor: for the North sensors, α is about 12,5 με/°C; for the South sensors, it is approximately 9,50 με/°C; for the neutral axis sensors, it is between 10,7 and 10,9 με/°C. The values that come out from the North and South sensors might be affected by the presence of the elastic jumps. In this case, the neutral axis sensors would produce a more reliable value of the thermal coefficient.

7.2 Parameters estimation using Bayesian Approach

In order to perform the Bayesian estimation, the author reminds that the strain model function is:

$$\hat{\varepsilon} = \varepsilon_0 + \frac{1}{E}\hat{\sigma}_c + \frac{\varphi_\infty}{E}\hat{C} + \varepsilon_{s,\infty}\hat{\beta}_s + \alpha\hat{T}$$

Where:

- $\hat{\varepsilon}$ is the strain resulting from the model;
- ε_0 is the strain offset;

- $\frac{1}{E}$, $\frac{\varphi_\infty}{E}$, $\varepsilon_{s,\infty}$, α are the already presented parameters (see *6*);
- $\widehat{\sigma_c}$, $\widehat{C}$, $\widehat{\beta_s}$, $\widehat{T}$ are the true time-dependent functions of stress, creep, shrinkage and temperature.

The relationship between true physical quantities and measurements/calculations is:

$$\hat{\varepsilon} = \varepsilon + g(\sigma_\varepsilon), \quad \widehat{\sigma_c} = \sigma_c + g(\sigma_{\sigma_c}), \quad \widehat{C} = C + g(\sigma_C),$$

$$\widehat{\beta_s} = \beta_s + g(\sigma_{\beta_s}), \quad \widehat{T} = T + g(\sigma_T),$$

Where:

- ε is the strain measured;
- T is the temperature measured;
- σ_c, C, β_s are the calculated functions of stress, creep and shrinkage;
- $g(\sigma)$ is a zero-mean Gaussian noise with standard deviation *σ*.

If we write the model equation introducing the noise, we obtain:

$$\varepsilon + g(\sigma_\varepsilon) = \varepsilon_0 + \frac{1}{E}\left(\sigma_c + g(\sigma_{\sigma_c})\right) + \frac{\varphi_\infty}{E}\left(C + g(\sigma_C)\right) + \varepsilon_{s,\infty}\left(\beta_s + g(\sigma_{\beta_s})\right) + \alpha\left(T + g(\sigma_T)\right)$$

$$\varepsilon - \left[\varepsilon_0 + \frac{1}{E}\sigma_c + \frac{\varphi_\infty}{E}C + \varepsilon_{s,\infty}\beta_s + \alpha T\right] + g(\sigma_{LH}) = 0$$

The expression $z = \varepsilon - \left[\varepsilon_0 + \frac{1}{E}\sigma_c + \frac{\varphi_\infty}{E}C + \varepsilon_{s,\infty}\beta_s + \alpha T\right]$ is the residual *z*, while the standard deviation of the likelihood function is:

$$\sigma_{LH}{}^2 = \left(\frac{\partial z}{\partial \varepsilon}\right)^2 \sigma_\varepsilon{}^2 + \left(\frac{\partial z}{\partial \sigma_c}\right)^2 \sigma_{\sigma_c}{}^2 + \left(\frac{\partial z}{\partial C}\right)^2 \sigma_C{}^2 + \left(\frac{\partial z}{\partial \beta_s}\right)^2 \sigma_{\beta_s}{}^2 + \left(\frac{\partial z}{\partial T}\right)^2 \sigma_T{}^2 =$$

$$= \sigma_\varepsilon{}^2 + \left(\frac{1}{E}\right)^2 \sigma_{\sigma_c}{}^2 + \left(\frac{\varphi_\infty}{E}\right)^2 \sigma_C{}^2 + \varepsilon_{s,\infty}{}^2 \sigma_{\beta_s}{}^2 + \alpha^2 \sigma_T{}^2$$

Thus, the probability of observing each *i*-th measurement (that is the likelihood) is:

$$\text{normpdf}\,(z_i, 0, \sigma_{LH}) = \text{normpdf}\left(\left(\varepsilon_i - \left[\varepsilon_0 + \frac{1}{E}\sigma_c + \frac{\varphi_\infty}{E}C + \varepsilon_{s,\infty}\beta_s + \alpha T\right]\right), 0, \sigma_{LH}\right)$$

In other words, applying the Bayes' theorem:

$$\mathrm{pdf}(\boldsymbol{\theta}|\mathbf{Y},\mathbf{X}) = \frac{\mathrm{pdf}(\mathbf{Y},\mathbf{X}|\boldsymbol{\theta})\cdot\mathrm{pdf}(\boldsymbol{\theta})}{\mathrm{pdf}(\mathbf{Y})} =$$

$$= \frac{[\prod_{i=1}^{n}\mathrm{pdf}(y_i,x_i|\,\boldsymbol{\theta})]\cdot[\mathrm{pdf}(\varepsilon_0)\cdot\mathrm{pdf}\left(\frac{1}{E}\right)\cdot\mathrm{pdf}\left(\frac{\varphi_\infty}{E}\right)\cdot\mathrm{pdf}(\varepsilon_{s,\infty})\cdot\mathrm{pdf}(\alpha)\cdot\mathrm{pdf}(\sigma_{LH})]}{\mathrm{pdf}(\mathbf{Y})}$$

Where the likelihood is:

$$\prod_{i=1}^{n}\mathrm{pdf}(y_i,x_i|\,\boldsymbol{\theta}) = \mathrm{normpdf}\left(\varepsilon_i - \mathrm{f}\left(\left[\sigma_{c_i},C_i,\beta_{s_i},T_i\right],\left[\,\varepsilon_0,\frac{1}{E},\frac{\varphi_\infty}{E},\varepsilon_{s,\infty},\alpha\right]^T\right),0,\sigma_{LH}\right)$$

and where:

$$\mathrm{f}\left(\left[\sigma_{c_i},C_i,\beta_{s_i},T_i\right],\left[\,\varepsilon_0,\frac{1}{E},\frac{\varphi_\infty}{E},\varepsilon_{s,\infty},\alpha\right]^T\right) = \varepsilon_0 + \frac{1}{E}\sigma_{c_i} + \frac{\varphi_\infty}{E}C_i + \varepsilon_{s,\infty}\beta_{s_i} + \alpha T_i$$

Therefore, the parameters vector $\boldsymbol{\theta}$ is:

$$\boldsymbol{\theta} = \left[\varepsilon_0,\frac{1}{E},\frac{\varphi_\infty}{E},\varepsilon_{s,\infty},\alpha,\sigma_{LH}\right]^T$$

To prevent numerical overflow and linearize the model, thus enhancing its solution, logarithmic distributions will be used. Therefore, the posterior distribution will transform into the following logarithmic one:

$$\log[\mathrm{pdf}(\boldsymbol{\theta}|\mathbf{Y},\mathbf{X})] = \sum_{i=1}^{n}\log[\mathrm{pdf}(y_i,x_i|\boldsymbol{\theta})] + \sum_{j=1}^{p}\log\left[\mathrm{pdf}(\theta_j\right]$$

To sum up, the posterior distribution expression will essentially derive from the combination of the likelihood and the prior distribution. The two distributions will be presented in the next paragraphs.

7.2.1 Prior distribution

The prior distribution is the combination of the prior knowledge on the parameters of the model. Thus, since the knowledge a priori is based on the values that commonly are used and calculated using the regulations, that is not a precise knowledge, wide trapezoidal distributions were assumed for the parameters. On the other hand, as regards ε_0 and σ_{LH}, two normal prior distributions were used. The former one is centred in 0 με with standard

deviation equal to 20 με, while the latter is centred in 20 με with standard deviation equal to 5 με.

Modulus of elasticity E

Since we know the strength class of concrete (fck = 55 MPa), we can suppose a mean value of the modulus of elasticity equal to 38 GPa (EN 1992-1-1, 2004). The prior distribution has been set as a trapezoid that has the maximum probability of occurrence between 35 and 45 MPa, while the probability is set to 0 for $E < 28$ GPa and $E > 50$ GPa.

However, the prior distribution needed for the Bayesian estimation is related to the inverse of *E*. Then it has been calculated using the inverse numbers mentioned and taken into account the conversion of the unit of measure (see *7.1*).

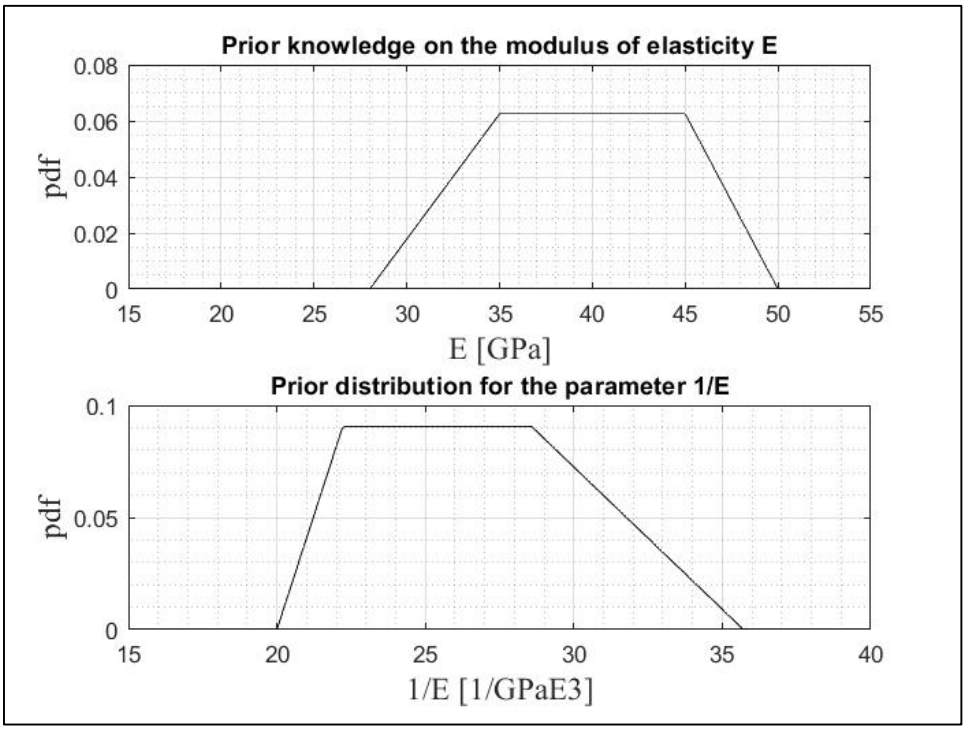

Figure 7.2. Prior distribution for the parameter 1/E

Creep coefficient φ

With reference to the Eurocode 2, the coefficient φ_∞, defined as the product of $\beta(f_{cm})$ and φ_{RH}, is function of the mean concrete compressive strength and the relative humidity RH. Following the formulation given in (EN 1992-1-1, 2004), the values of the two coefficients are:

- $\beta(f_{cm}) = 2{,}1166$;
- $\varphi_{RH} = 0{,}9920$, assuming a mean value for RH = 80% and h0 = 1500 mm.

Thus, the expected value of φ_∞ is 2,0997. The a priori knowledge for the coefficient φ_∞ has been set as a trapezoidal distribution presented in the next picture:

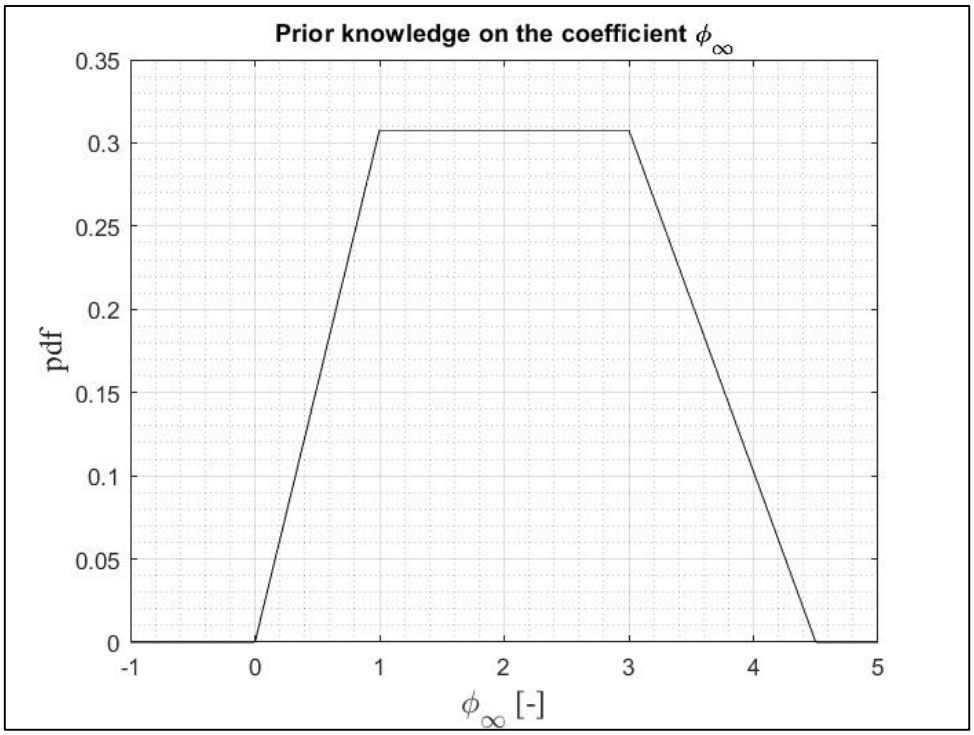

Figure 7.3. A priori knowledge on the creep coefficient φ_∞

However, the prior distribution needed for the Bayesian estimation is related to the inverse of *E*. Then, it has been calculated multiplying the expected value of 1/E (1/38 GPa) for the values of the trapezoid considered above. For the explanation of the units of measure, see *7.1*.

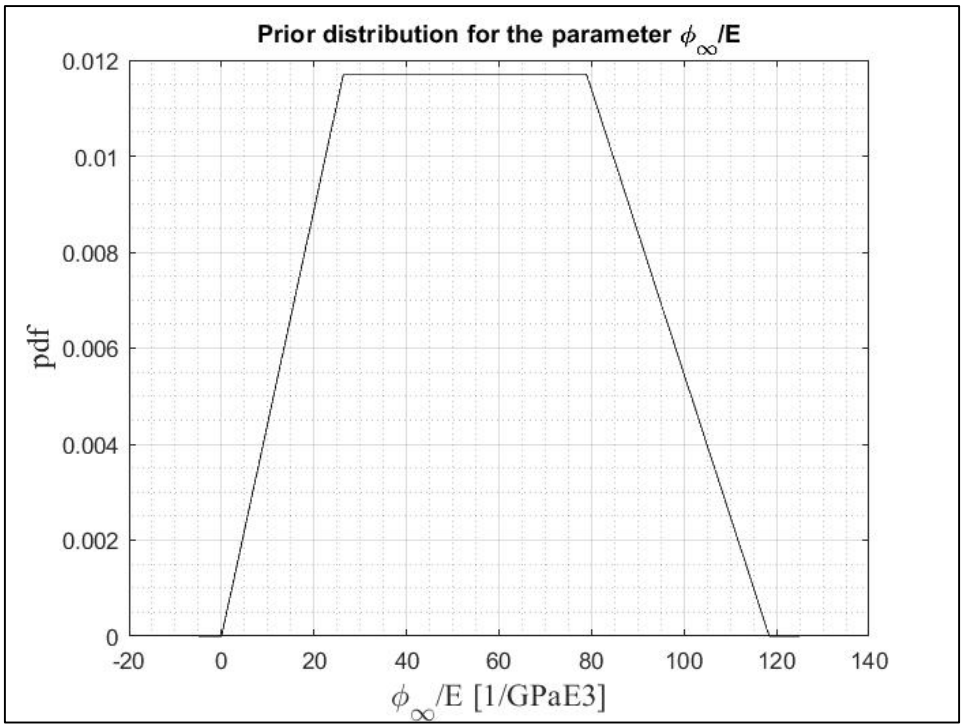

Figure 7.4. Prior distribution for the parameter φ_∞/E

Shrinkage strain at t=∞ $\varepsilon_{s,\infty}$

Following the formulations of the Eurocode 2, the parameter $\varepsilon_{s,\infty}$ depends on the coefficient k_h (see *6.3*) and the basic drying shrinkage strain $\varepsilon_{cd,0}$, function of the relative humidity. Assuming a class of concrete R, $\varepsilon_{s,\infty}$ results equal to approximately 200 με.

Thus, the trapezoid presented in the next figure has been assumed as prior distribution for this parameter.

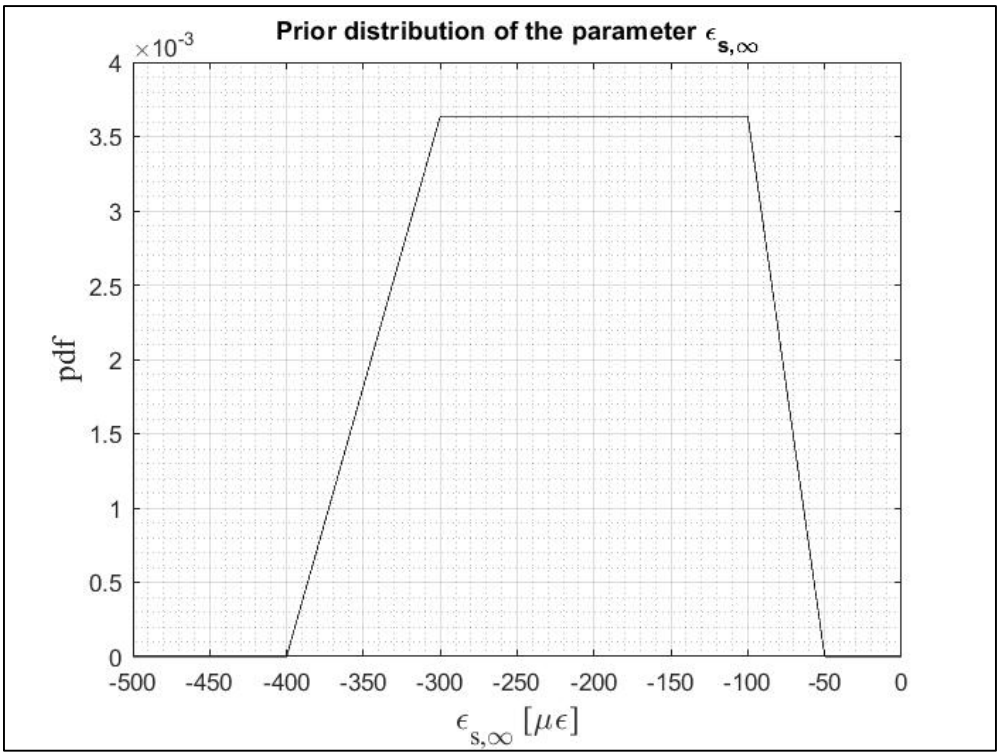

Figure 7.5. Prior distribution for the parameter $\varepsilon_{s,\infty}$

Thermal coefficient α

The thermal coefficient of the concrete is generally between 10 and 12 με/°C. For this parameter a slack prior distribution has been used.

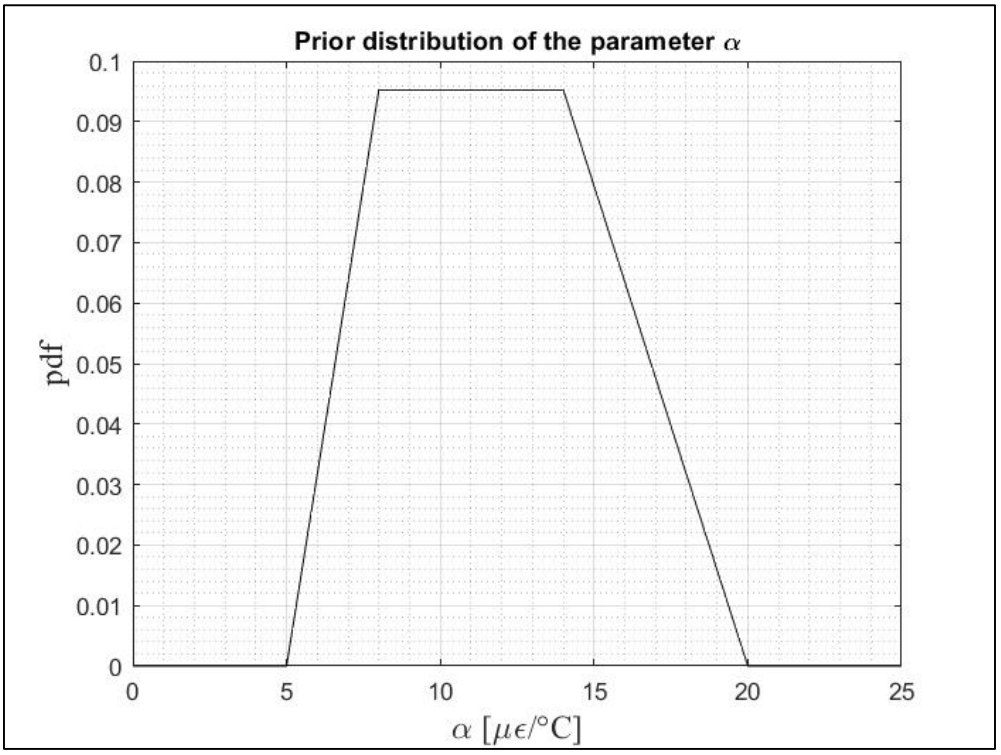

Figure 7.6. Prior distribution for the parameter α

7.2.2 Results

The Metropolis-Hastings algorithm (MH) can be used to estimate the Maximum A Posteriori (MAP) of the parameters. They are the mean values of the samples extracted by the MH. Following, the results obtained with the Bayesian inference for the North, South, West and East sensors will be illustrated and discussed. For completeness, the results obtained using the other four strain data (North-West, North-East, South-West, and South-East sensors) are reported in *Annex 3*.

North sensor

Sensor (location)	E[ε_0] [με]	E[1/E] [1/MPaE6]	E[ϕ_∞/E] [1/MPaE6]	E[$\varepsilon_{s,\infty}$] [με]	E[α] [με/°C]	E[σ_{LH}] [με]
CT-OD7.5-S-STR-S-1194 (North)	-31	25,01	68,77	-271	12,59	32

Table 7.10. CT-OD7.5-S-STR-S-1194 (North) BA parameters estimated values

Covariance matrix:

	ε_0	1/E	ϕ_∞/E	$\varepsilon_{s,\infty}$	α	σ_{LH}
ε_0	3,8946	0,0598	0,4819	-8,5236	-0,2586	-0,1222
1/E	0,0598	0,2010	-0,4327	1,8321	-0,0048	0,0242
ϕ_∞/E	0,4819	-0,4327	3,1421	-0,3520	0,0051	-0,0692
$\varepsilon_{s,\infty}$	-8,5236	1,8321	-0,3520	77,7015	-0,0175	0,5739
α	-0,2586	-0,0048	0,0051	-0,0175	0,0608	0,0076
σ_{LH}	-0,1222	0,0242	-0,0692	0,5739	0,0076	0,4431

Std[ε_0] [με]	Std[1/E] [1/MPaE6]	Std[ϕ_∞/E] [1/MPaE6]	Std[$\varepsilon_{s,\infty}$] [με]	Std[α] [με/°C]
2	0,44	1,77	9	0,26

Pearson's correlation:

	ε_0	1/E	ϕ_∞/E	$\varepsilon_{s,\infty}$	α	σ_{LH}
ε_0	1,0000	0,0675	0,1377	-0,4900	-0,5315	-0,0930
1/E	0,0675	1,0000	-0,5445	0,4636	-0,0430	0,0811
ϕ_∞/E	0,1377	-0,5445	1,0000	-0,0225	0,0116	-0,0586
$\varepsilon_{s,\infty}$	-0,4900	0,4636	-0,0225	1,0000	-0,0081	0,0978
α	-0,5315	-0,0430	0,0116	-0,0081	1,0000	0,0463
σ_{LH}	-0,0930	0,0811	-0,0586	0,0978	0,0463	1,0000

From the estimated parameters we can calculate:

- E=39987 MPa;
- φ_∞=2,75.

Using the values obtained with this approach, the temperature compensated strain can be evaluated. It is the overall trend of the strain that is not influenced by temperature. In the following picture, it is depicted together with the *temperature compensated* strain model $\varepsilon = \varepsilon_0 + \frac{1}{E}\sigma_c + \frac{\varphi_\infty}{E}C + \varepsilon_{s,\infty}\beta_s$ (note that the temperature strain contribute is neglected) with the parameters values obtained.

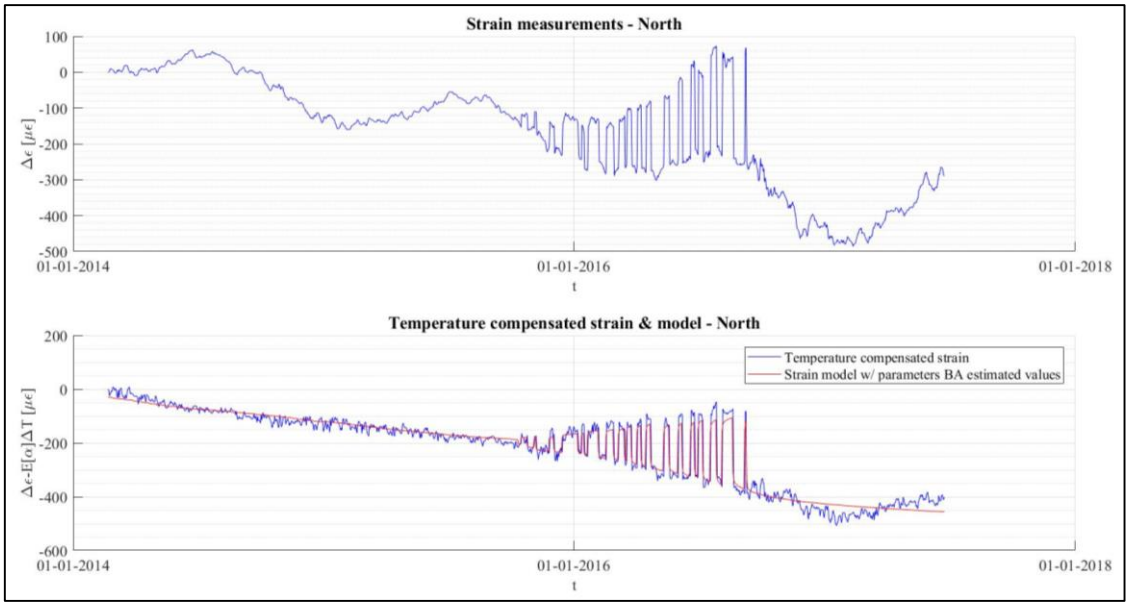

Figure 7.7. Temperature compensated measured strain and model with the parameters BA estimated values for the North sensor

At the end of the process, we obtain a posterior distribution for each parameter that is compared with the prior one in the following picture:

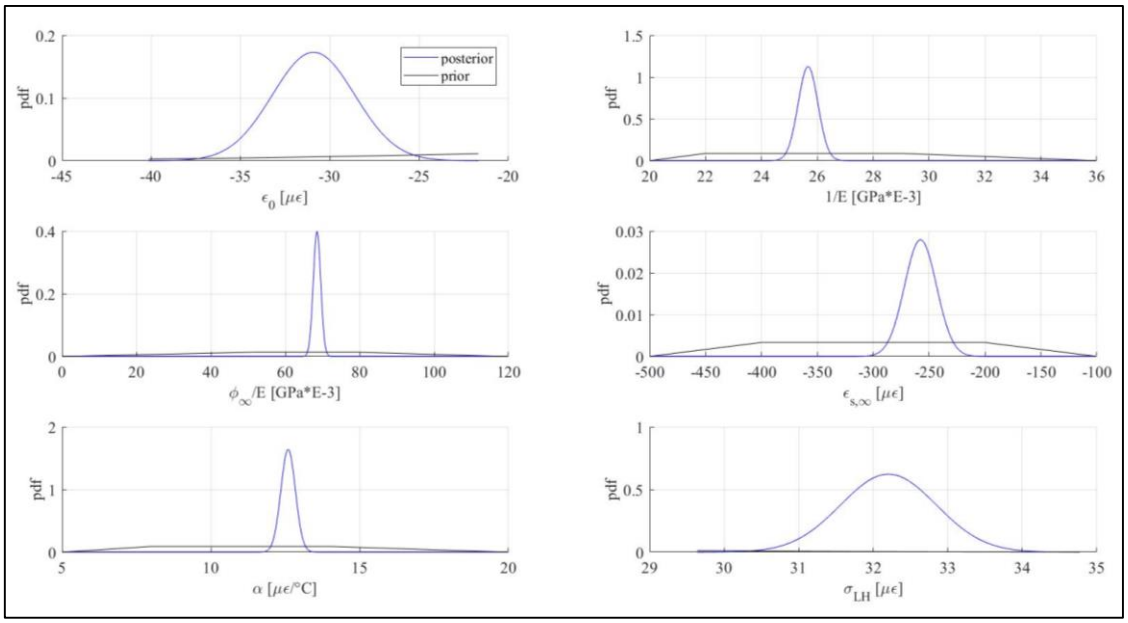

Figure 7.8. Prior (black) vs. Posterior (blue) distributions for the North sensor

Metropolis-Hastings outputs

Following, the MH samples have been reported in form of histograms. The second plot depicts the trend of the samples while the algorithm is running. You can easily see that the algorithm converges to a defined value, after the very first set of about 500 samples ("burn in"), which is neglected in the estimation of parameter values.

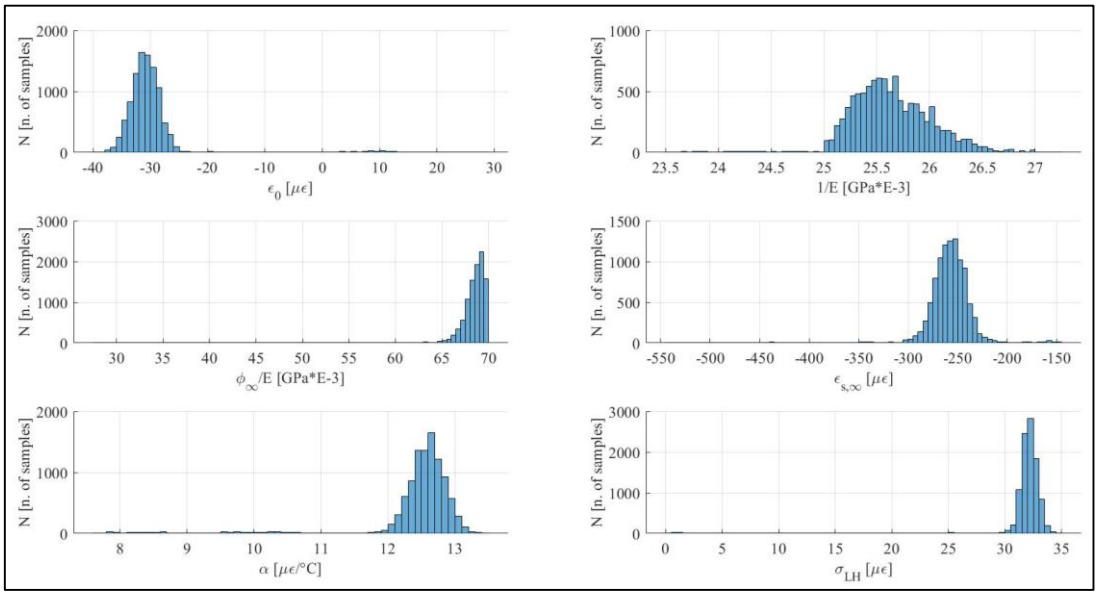

Figure 7.9. MH samples distributions of each parameter for the North sensor

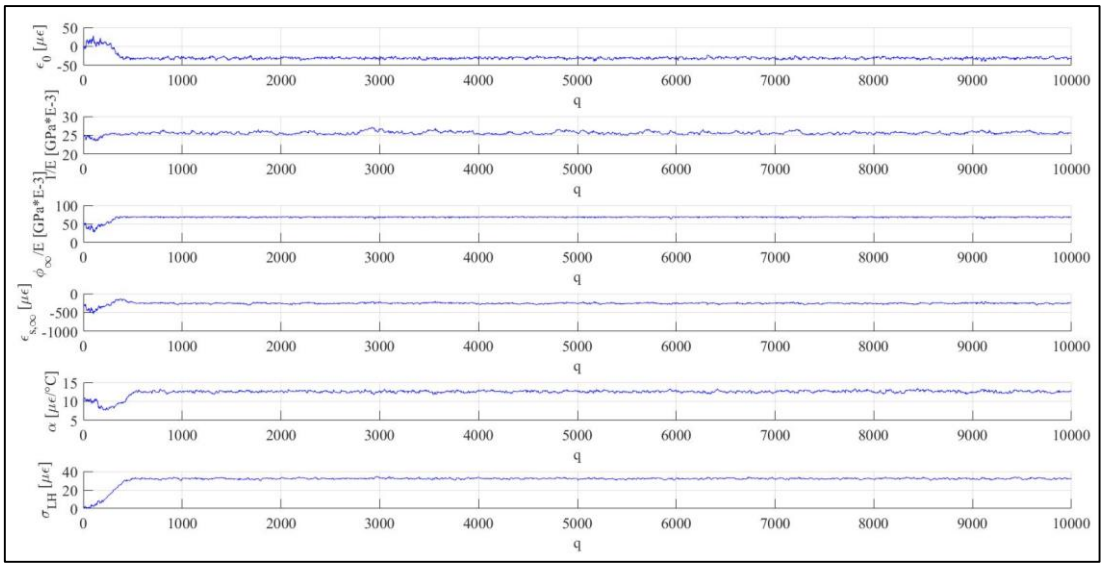

Figure 7.10. MH random samples during the 10000 iterations (North)

South sensor

Sensor (location)	E[ε₀] [με]	E[1/E] [MPaE-6]	E[ϕ∞/E] [MPaE-6]	E[εs,∞] [με]	E[α] [με/°C]	E[σLH] [με]
CT-OD7.5-S-STR-S-1198 (South)	-33	25,04	64,82	-373	8,98	32

Table 7.11. CT-OD7.5-S-STR-S-1198 (South) BA parameters estimated values

Covariance matrix:

	ε₀	1/E	ϕ∞/E	εs,∞	α	σLH
ε₀	7,0453	-0,3616	0,0425	-36,1723	-0,5035	-0,1256
1/E	-0,3616	0,5660	-1,4101	5,7450	0,0211	-0,0126
ϕ∞/E	0,0425	-1,4101	6,7941	12,9937	0,0082	0,1766
εs,∞	-36,1723	5,7450	12,9937	426,7063	1,9798	1,5294
α	-0,5035	0,0211	0,0082	1,9798	0,0752	0,0049
σLH	-0,1256	-0,0126	0,1766	1,5294	0,0049	0,4202

Std[ε₀] [με]	Std[1/E] [1/MPaE6]	Std[ϕ∞/E] [1/MPaE6]	Std[εs,∞] [με]	Std[α] [με/°C]
3	0,75	2,61	21	0,27

Pearson's correlation:

	ε_0	1/E	ϕ_∞/E	$\varepsilon_{s,\infty}$	α	σ_{LH}
ε_0	1,0000	-0,1811	0,0061	-0,6597	-0,6916	-0,0730
1/E	-0,1811	1,0000	-0,7190	0,3697	0,1023	-0,0258
ϕ_∞/E	0,0061	-0,7190	1,0000	0,2413	0,0115	0,1045
$\varepsilon_{s,\infty}$	-0,6597	0,3697	0,2413	1,0000	0,3494	0,1142
α	-0,6916	0,1023	0,0115	0,3494	1,0000	0,0276
σ_{LH}	-0,0730	-0,0258	0,1045	0,1142	0,0276	1,0000

From the estimated parameters we can calculate:

- E=39940 MPa;
- φ_∞=2,59.

Using the values obtained with this approach, the temperature compensated strain and the model can be evaluated.

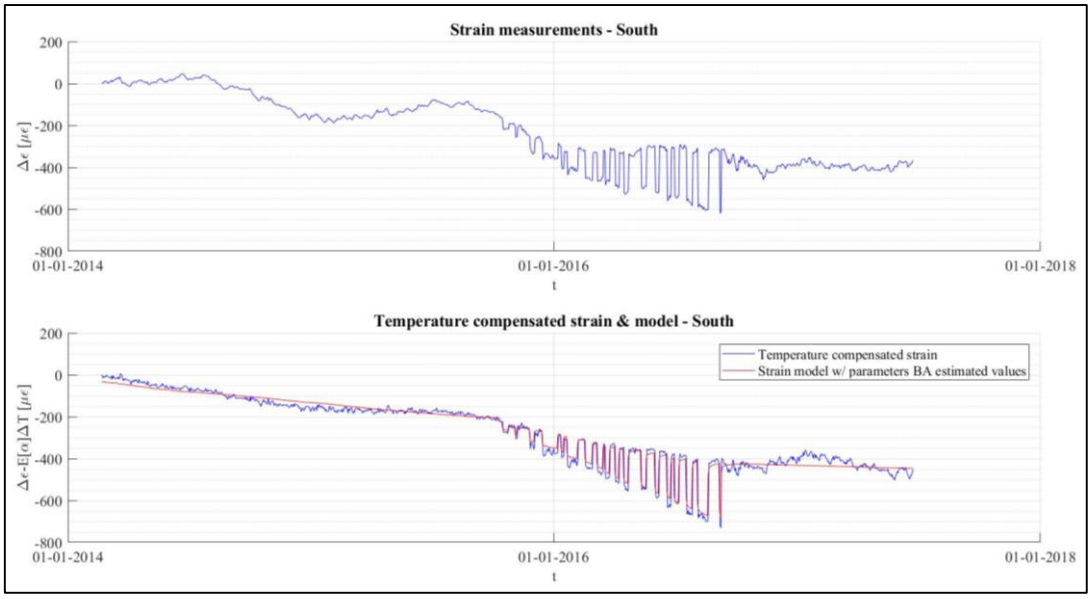

Figure 7.11. Temperature compensated strain and model with the parameters BA estimated values for the South sensor

At the end of the process we obtain a posterior distribution for each parameter that is compared with the prior one in the following picture:

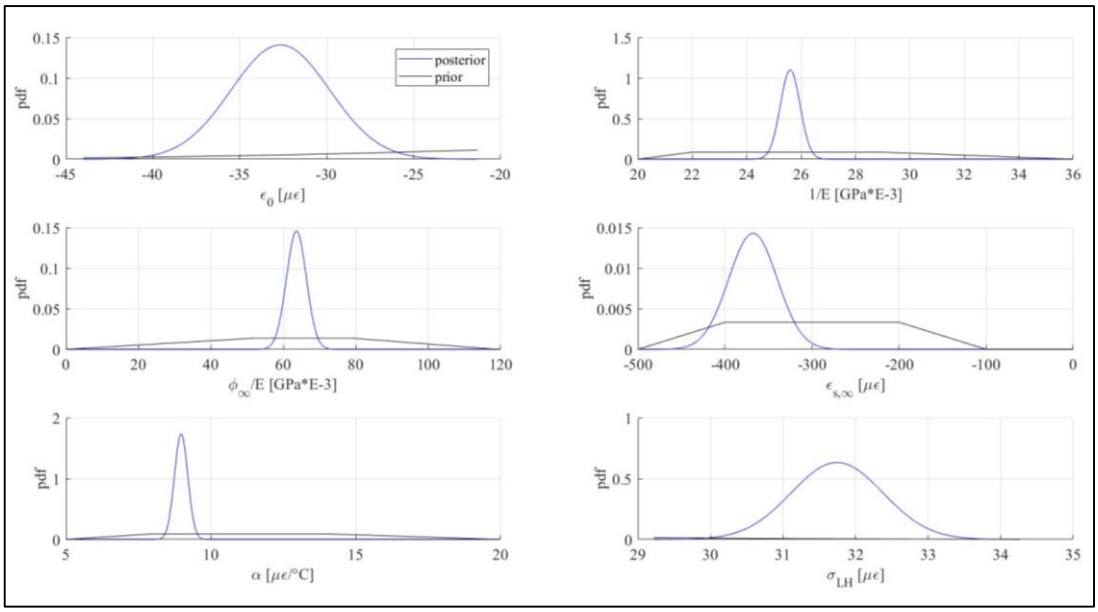

Figure 7.12. Prior (black) vs. Posterior (blue) distributions for the South sensor

Metropolis-Hastings outputs

Following, the MH samples have been reported in form of histograms. The second plot depicts the trend of the samples while the algorithm is running. You can easily see that the algorithm converges to a defined value, after the very first set of about 1000 samples ("burn in"), which is neglected in the estimation of parameter values.

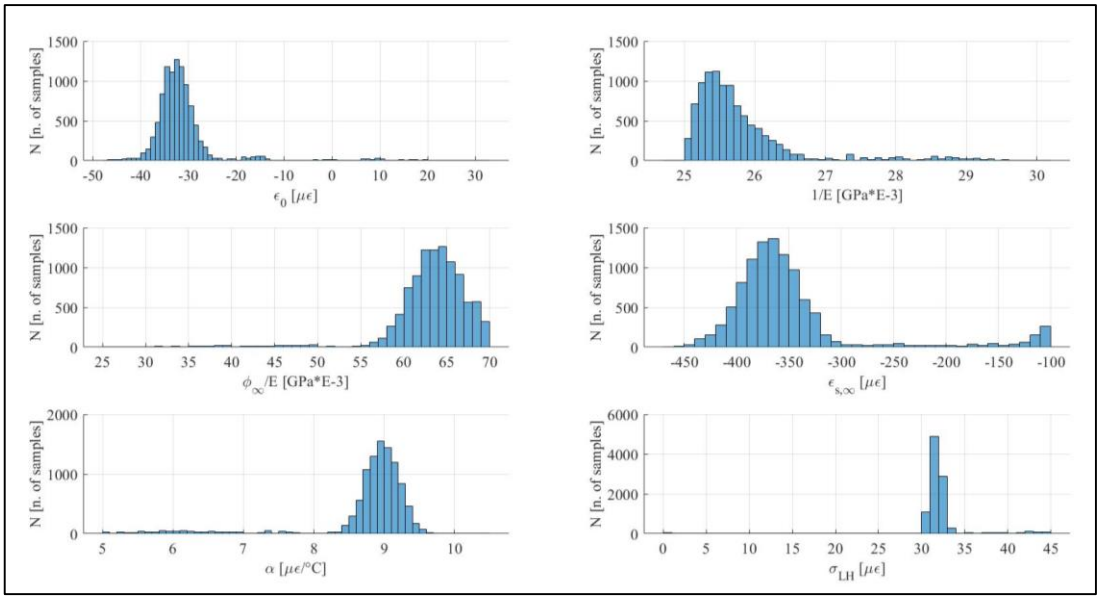

Figure 7.13. MH samples distributions of each parameter for the South sensor

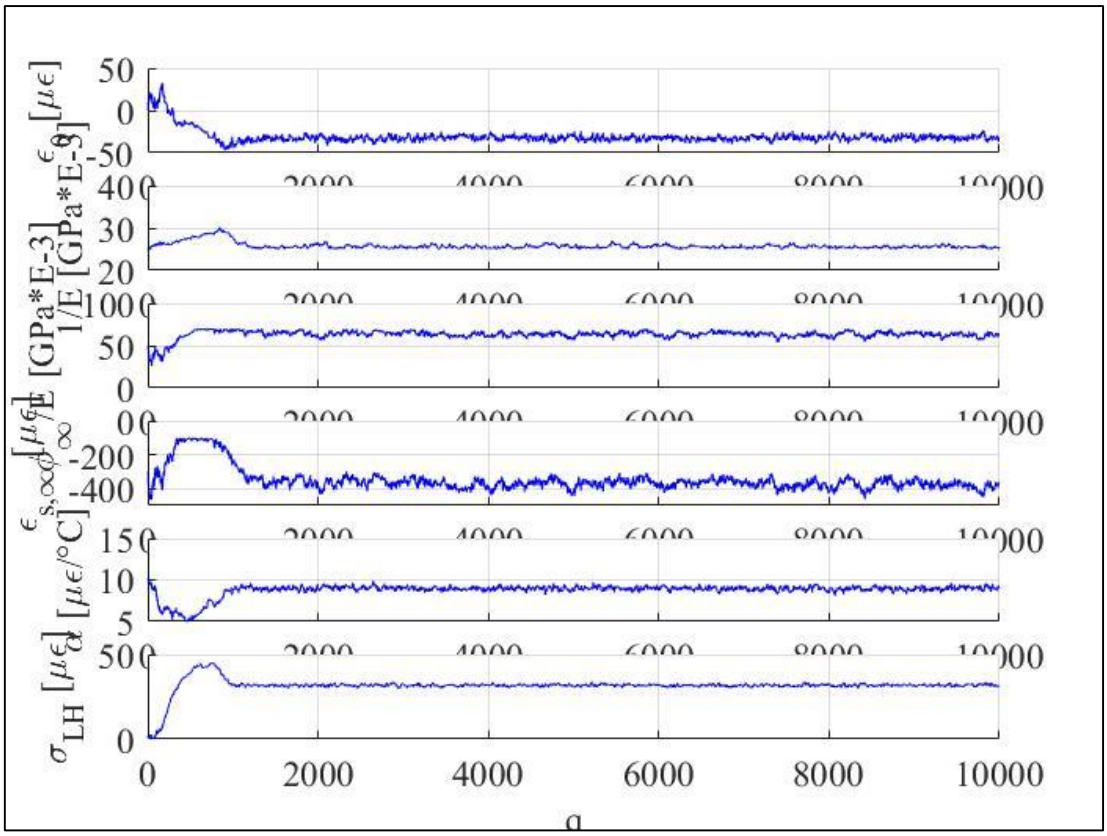

Figure 7.14. MH random samples during the 10000 iterations (South)

West sensor

Sensor (location)	E[ε_0] [με]	E[1/E] [MPaE-6]	E[ϕ_∞/E] [MPaE-6]	E[$\varepsilon_{s,\infty}$] [με]	E[α] [με/°C]	E[σ_{LH}] [με]
CT-OD7.5-S-STR-S-1192 (West)	-17	25,08	30,09	-245	10,85	17

Table 7.12. CT-OD7.5-S-STR-S-1192 (West) BA parameters estimated values

Covariance matrix:

	ε_0	1/E	ϕ_∞/E	$\varepsilon_{s,\infty}$	α	σ_{LH}
ε_0	1,7258	2,0604	-5,9249	-0,0740	-0,0760	-0,0152
1/E	2,0604	7,5511	-23,5508	0,1556	0,0162	-0,1954
ϕ_∞/E	-5,9249	-23,5508	73,9014	-0,2134	-0,0643	0,6562
$\varepsilon_{s,\infty}$	-0,0740	0,1556	-0,2134	2,1869	0,0028	0,0482
α	-0,0760	0,0162	-0,0643	0,0028	0,0130	-0,0007
σ_{LH}	-0,0152	-0,1954	0,6562	0,0482	-0,0007	0,1349

Std[ε_0] [με]	Std[1/E] [1/MPaE6]	Std[ϕ_∞/E] [1/MPaE6]	Std[$\varepsilon_{s,\infty}$] [με]	Std[α] [με/°C]
2	2,75	8,60	2	0,11

Pearson's correlation:

	ε_0	1/E	ϕ_∞/E	$\varepsilon_{s,\infty}$	α	σ_{LH}
ε_0	1,0000	0,5707	-0,5246	-0,0381	-0,5075	-0,0314
1/E	0,5707	1,0000	-0,9970	0,0383	0,0517	-0,1936
ϕ_∞/E	-0,5246	-0,9970	1,0000	-0,0168	-0,0656	0,2078
$\varepsilon_{s,\infty}$	-0,0381	0,0383	-0,0168	1,0000	0,0164	0,0887
α	-0,5075	0,0517	-0,0656	0,0164	1,0000	-0,0165
σ_{LH}	-0,0314	-0,1936	0,2078	0,0887	-0,0165	1,0000

From the estimated parameters we can calculate:

- E=39879 MPa;
- φ_∞=1,20.

Using the values obtained with this approach, the temperature compensated strain and the model can be evaluated.

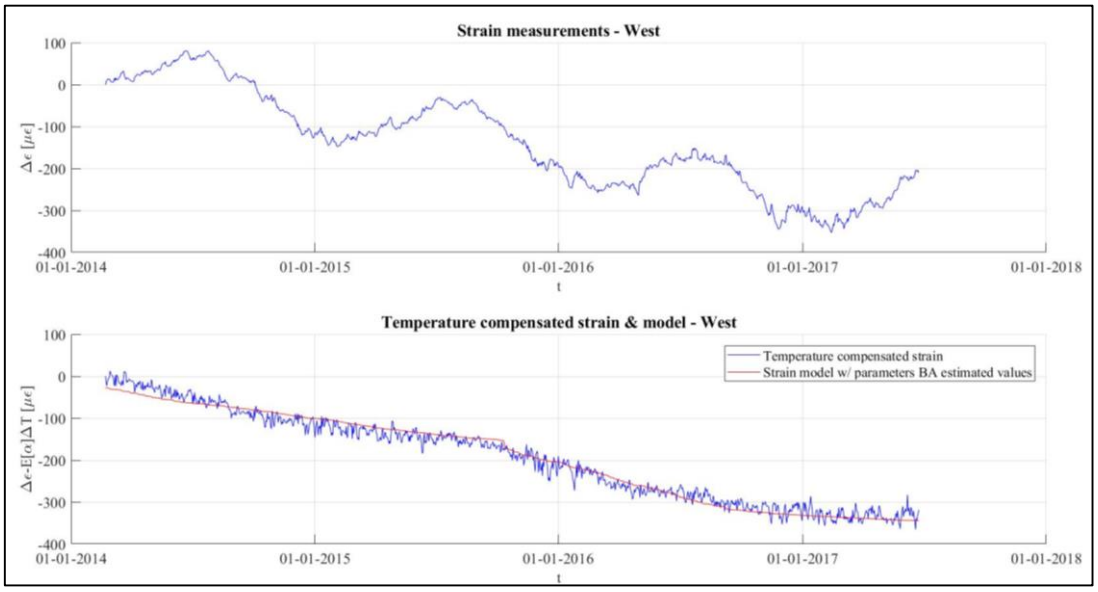

Figure 7.15. Temperature compensated strain and model with the parameters BA estimated values for the West sensor

At the end of the process we obtain a posterior distribution for each parameter that is compared with the prior one in the following picture:

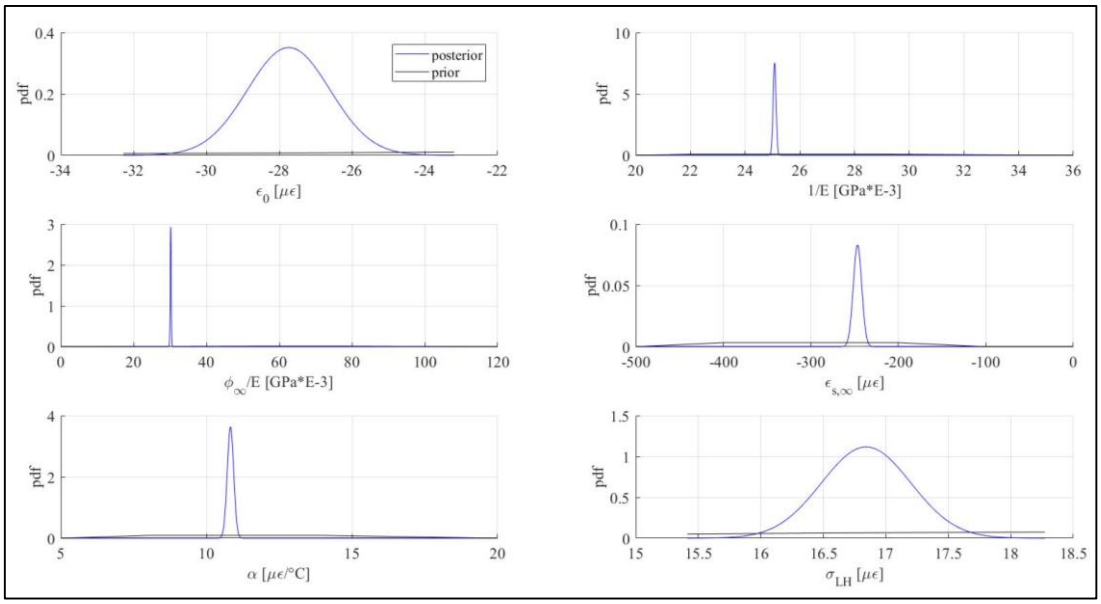

Figure 7.16. Prior (black) vs. Posterior (blue) distributions for the West sensor

Metropolis-Hastings outputs

Following, the MH samples have been reported in form of histograms. The second plot depicts the trend of the samples while the algorithm is running. You can easily see that the algorithm converges to a defined value, after the very first set of about 200 samples ("burn in"), which is neglected in the estimation of parameter values.

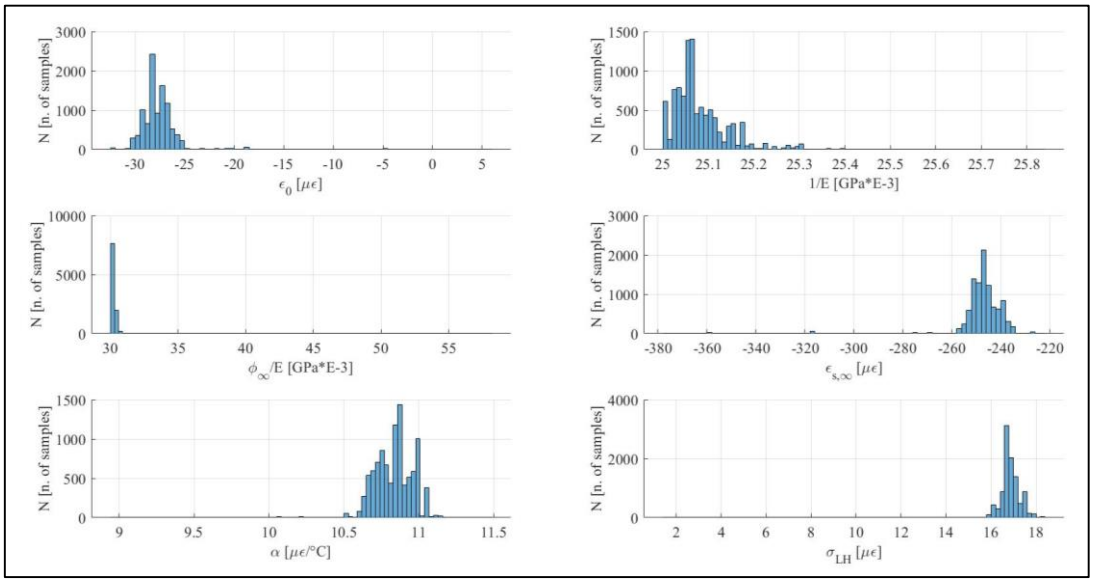

Figure 7.17. MH samples distributions of each parameter for the West sensor

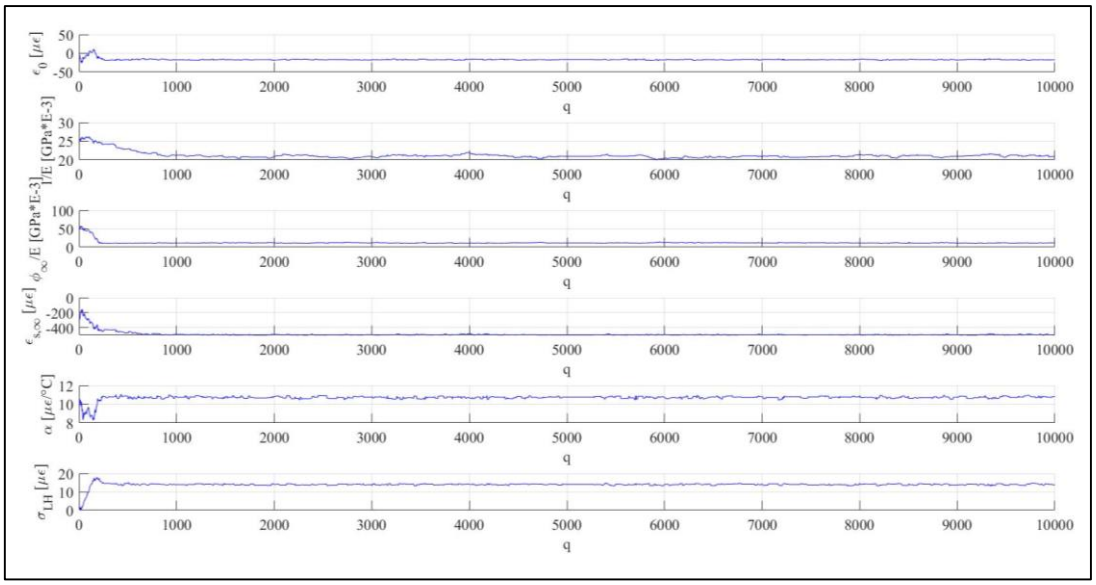

Figure 7.18. MH random samples during the 10000 iterations (West)

East sensor

Sensor (location)	E[ε₀] [με]	E[1/E] [MPaE-6]	E[ϕ∞/E] [MPaE-6]	E[εs,∞] [με]	E[α] [με/°C]	E[σLH] [με]
CT-OD7.5-S-STR-S-1196 (East)	-8	20,07	6,02	-117	10,9	18

Table 7.13. CT-OD7.5-S-STR-S-1196 (East) BA parameters estimated values

Covariance matrix:

	ε₀	1/E	ϕ∞/E	εs,∞	α	σLH
ε₀	9,8713	0,1274	24,2600	30,8935	-0,2684	7,5515
1/E	0,1274	0,0056	0,4046	0,7637	-0,0027	0,1182
ϕ∞/E	24,2600	0,4046	77,9725	127,8149	-0,4518	22,5924
εs,∞	30,8935	0,7637	127,8149	255,7594	-0,4168	34,4417
α	-0,2684	-0,0027	-0,4518	-0,4168	0,0207	-0,1602
σLH	7,5515	0,1182	22,5924	34,4417	-0,1602	7,0050

Std[ε₀] [με]	Std[1/E] [1/MPaE6]	Std[ϕ∞/E] [1/MPaE6]	Std[εs,∞] [με]	Std[α] [με/°C]
3	0,07	8,83	16	0,14

Pearson's correlation:

	ε_0	1/E	ϕ_∞/E	$\varepsilon_{s,\infty}$	α	σ_{LH}
ε_0	1,0000	0,5409	0,8744	0,6148	-0,5941	0,9081
1/E	0,5409	1,0000	0,6113	0,6370	-0,2492	0,5955
ϕ_∞/E	0,8744	0,6113	1,0000	0,9051	-0,3559	0,9667
$\varepsilon_{s,\infty}$	0,6148	0,6370	0,9051	1,0000	-0,1813	0,8137
α	-0,5941	-0,2492	-0,3559	-0,1813	1,0000	-0,4210
σ_{LH}	0,9081	0,5955	0,9667	0,8137	-0,4210	1,0000

From the estimated parameters we can calculate:

- E=49834 MPa;
- φ_∞=0,30.

Using the values obtained with this approach, the temperature compensated strain and the model can be evaluated. The author stated that the plot of the compensated strain obtained from East sensor data was not representative, as the algorithm provides parameter values that were considered not relevant. In the following paragraph the reasons that led to this decision will be explained.

Summary

	E[ε_0] [με]	E[E] [MPa]	E[φ] [-]	E[$\varepsilon_{s,\infty}$] [με]	E[α] [με/°C]	E[σ_{LH}] [με]
NORTH	-31	39987	2,75	-271	12,59	32
NORTH-WEST	-35	39784	2,34	-281	12,73	30
NORTH-EAST	-30	39862	1,96	-133	13,09	27
SOUTH	-33	39940	2,59	-373	8,98	32
SOUTH-WEST	-22	39552	2,04	-286	9,53	30
SOUTH-EAST	-10	39745	2,03	-281	9,70	30
WEST	-17	39879	1,20	-245	10,85	17
EAST	-8	49834	0,30	-117	10,9	18

Table 7.14. Summary of the estimated values for each sensor data

7.2.3 Results discussion

The Bayesian approach was performed on the data registered by all the eight strain gages located on TS2. The parameters estimation seem to produce reasonable values for every parameter.

In this case, we obtain a sixth parameter value, that is the standard deviation of the likelihood $\sigma_{LH.}$ It takes into account the uncertainties that we have on the likelihood. It is maintained as a free parameter in order to obtain a much higher accuracy on the estimation of the other parameters.

From the observation of the values obtained, we can certainly notice that the modulus of elasticity E is really close to the expected value for each one of the registered datasets, except for the East sensor. If we compare with the other seven sensor data, the East side registered data generate also very small values (in absolute value) for the other two parameters that describe the contracting behaviour of the concrete, φ_∞ and $\varepsilon_{s,\infty}$. The reason for this result is the same described in the LSA results (see *7.1.1*). The main issue is that the East sensor registered an overall change in strain much smaller than the other ones, thus resulting in an overestimation of the modulus of elasticity E (and so of concrete strength), as well as an underestimation of the contractive contributes of creep (φ_∞) and shrinkage ($\varepsilon_{s,\infty}$).

Another feature that the results obtained with the two methods have in common is the values of the thermal coefficient α. Also applying the Bayesian inference, we find that α seems to be affected by the presence of the elastic jumps in the registered data of the North and South sides sensor, so that the relative α value is in contrast. On the contrary, neutral axis sensor again return a value of approximately 10,9 με/°C, similar to the one estimated by the LSA.

However, the difference between the results achieved with the two methods applied is clear. The main reason is that as least square analysis only considers the number of data points as the sample number, it has a much larger uncertainty in comparison to Bayesian approach, particularly the Metropolis-Hasting algorithm. As the sample number N can be increased without requiring more data points, then the accuracy of the estimations obtained via this method would be improved significantly.

It is also interesting to note that the period during which the deck was built is not a random choice.

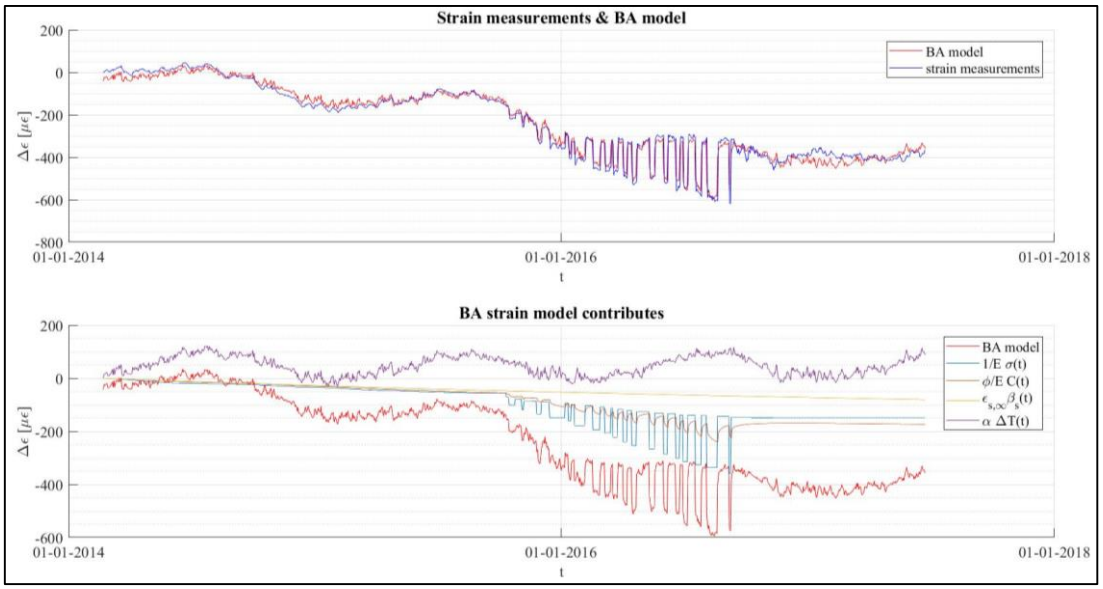

Figure 7.19. BA model v. strain measurements (above), BA model and BA estimated strain contributes (below)

If we focus on the balanced cantilevering process, you can see that the highest elastic jumps occur during summer 2016, when the temperature rises and reaches the highest peaks (see **Figure 5.7**). Now, focusing on **Figure 7.19** relative to the South sensor data, the second plot shows the strain model resulting from the BA estimation (red), together with all its contributes. Consider the last peak of contraction (that is the maximum level of contraction experienced by the sensor): the model, as well as the measurements above, indicates a total strain of ~ -575 με, that is the sum of the elastic (~ -375 με, in blue), creep (~ -230 με, in orange), shrinkage (~ -70 με, in yellow) and temperature (~ +100 με, in purple) contributions. It is clear that if this last jump had happened during the winter, temperature dilatation contribution would have been much smaller, if not close to zero. In that case, the measured strain would have been approximately -670 με (an additional 100 με contraction, and thus compressive stress). This is evident if we observe the compensated strain in **Figure 7.11**: in correspondence of the last contraction peak, we read a contraction of ~700 με. As supposed the effect of the temperature is important to mitigate the contraction, and so the compressive stress, of the concrete during the construction of the deck.

A discussion on the covariance matrix and Pearson's correlations is needed. The main diagonal of the covariance matrix provides the variance of each parameter, while the off-

diagonal entries provide the covariance between each parameter pair. Observing the covariance matrix for each sensor, we can easily notice that the parameter on which the parameter estimated with the highest uncertainty is $\varepsilon_{s,\infty}$. Thus, the standard deviation terms related to this parameter results to be very high. This would be the effect of a slack *a priori* knowledge on its value. Indeed, the author reminds that the posterior distribution is function of the prior distribution, influenced by the *a priori* knowledge on each single parameter (see *7.2*). In contrast, the estimate of the thermal coefficient α is affected by very small uncertainty, that is the result of a complete and quite precise knowledge on the temperature.

Pearson's correlation matrix shows the correlation between each couple of parameters. The Pearson correlation coefficient ρ is a measure of the linear correlation between two variables. It is defined as the covariance of the two variables divided by the product of their standard deviations. It has a value between +1 and -1, where +1 means that there is a total positive correlation, 0 means no linear correlation and -1 means total negative correlation. The more ρ is close to 1, the higher is the linear correlation between the two variables. From the results obtained, it is evident the strong correlation between the parameters 1/E and φ_∞/E, as expected. In contrast, the other variables seem to be no strict dependency.

7.2.4 Multi-data Bayesian estimation

Finally, in order to obtain a more accurate parameter estimation, the Bayesian inference has been applied to the whole dataset available, considering the strain data from all the 8 sensors.

$E[\varepsilon_0]$ [με]	E[1/E] [1/MPaE6]	$E[\phi_\infty/E]$ [1/MPaE6]	$E[\varepsilon_{s,\infty}]$ [με]	E[α] [με/°C]	$E[\sigma_{LH}]$ [με]
-9	25,11	60,13	-133	10,48	55

From the estimated parameters we can calculate:

- E=39825 MPa;
- φ_∞=2,39.

Covariance matrix:

	ε_0	1/E	ϕ_∞/E	$\varepsilon_{s,\infty}$	α	σ_{LH}
ε_0	4,6035	0,0856	-2,3110	-25,6444	-0,1269	0,0149
1/E	0,0856	0,1690	-0,5093	0,0873	-0,0012	0,0155
ϕ_∞/E	-2,3110	-0,5093	4,0650	20,0555	0,0353	-0,0767
$\varepsilon_{s,\infty}$	-25,6444	0,0873	20,0555	202,6758	0,2853	-0,2113
α	-0,1269	-0,0012	0,0353	0,2853	0,0200	0,0022
σ_{LH}	0,0149	0,0155	-0,0767	-0,2113	0,0022	0,1671

Std[ε_0] [με]	Std[1/E] [1/MPaE6]	Std[ϕ_∞/E] [1/MPaE6]	Std[$\varepsilon_{s,\infty}$] [με]	Std[α] [με/°C]
2	0,41	2,01	14	0,14

Pearson's correlation:

	ε_0	1/E	ϕ_∞/E	$\varepsilon_{s,\infty}$	α	σ_{LH}
ε_0	1,0000	0,0970	-0,5342	-0,5874	-0,4181	0,0170
1/E	0,0970	1,0000	-0,7345	0,0149	-0,0205	0,0920
ϕ_∞/E	-0,5342	-0,7345	1,0000	0,6987	0,1238	-0,0930
$\varepsilon_{s,\infty}$	-0,5874	0,0149	0,6987	1,0000	0,1417	-0,0363
α	-0,4181	-0,0205	0,1238	0,1417	1,0000	0,0385
σ_{LH}	0,0170	0,0920	-0,0930	-0,0363	0,0385	1,0000

Following, you can see the comparison between the prior and the posterior distributions:

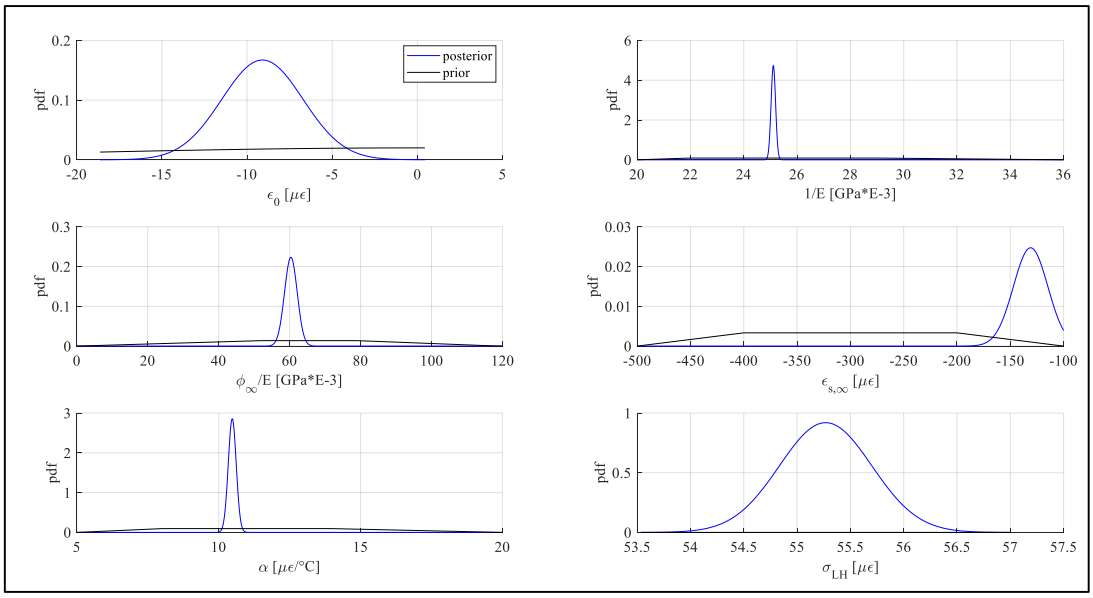

Figure 7.20. Prior (black) vs. posterior (blue) distributions from the multi-data estimation

Metropolis-Hastings outputs

Following, the MH samples have been reported in form of histograms. The second plot depicts the trend of the samples while the algorithm is running. You can easily see that the algorithm converges to a defined value, after the very first set of about 500 samples ("burn in"), which is neglected in the estimation of parameter values.

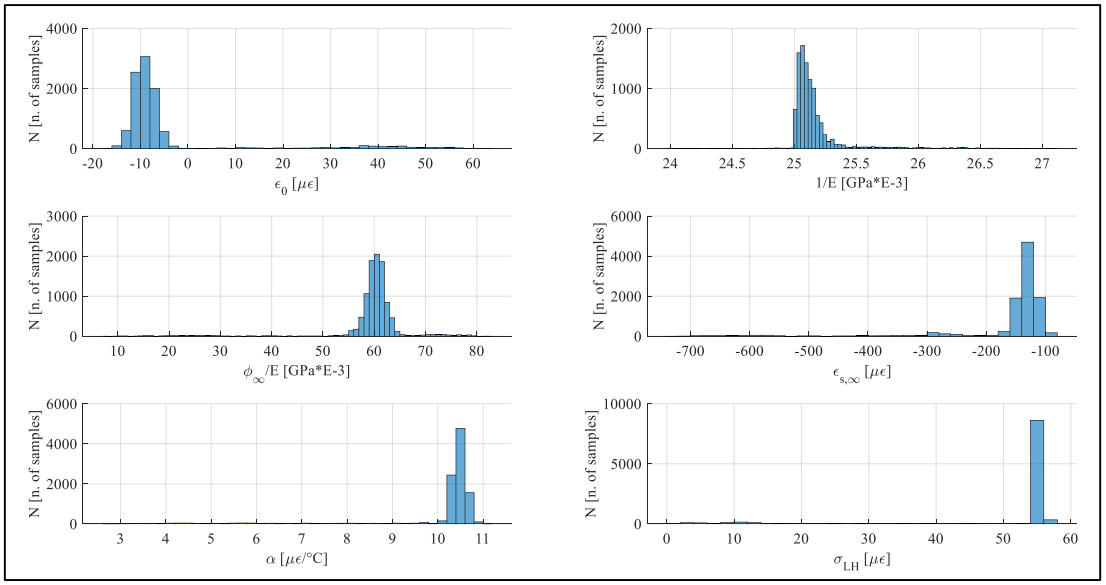

Figure 7.21. MH samples distributions of each parameter from all strain data-sets

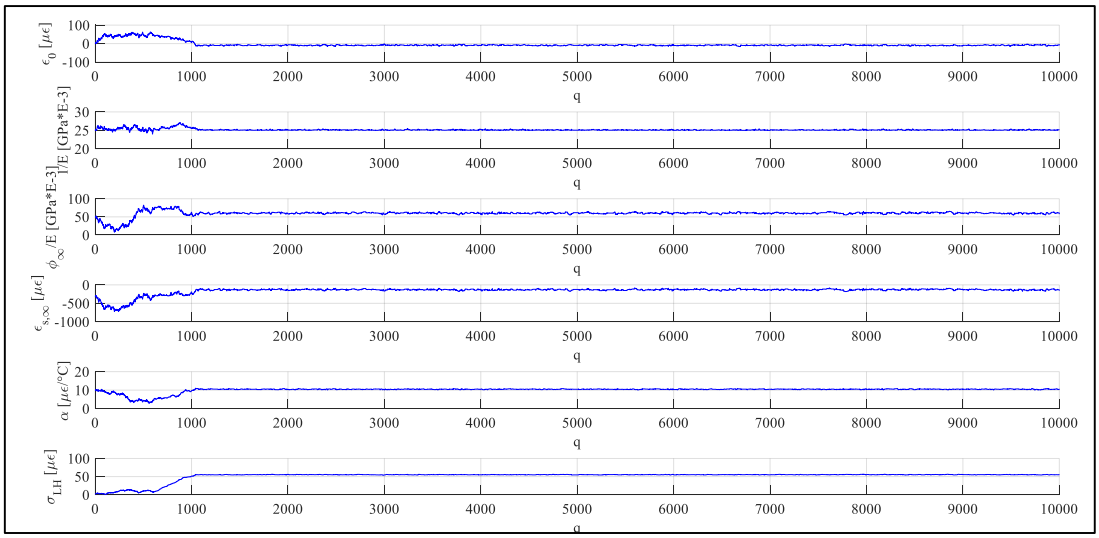

Figure 7.22. MH random samples during the 10000 iterations (multi-data)

8. Conclusions

The Queensferry Crossing case study on the SHM deployment proved to be an interesting topic. The initial aims of this case study were:

- to develop a thorough enough understanding of the structural scheme and construction of the Queensferry Crossing to enable adequate analysis of the data from the sensors;
- to infer what construction operations are taking place by analysing the SHM data;
- to interpret strain data and understand their correlation with temperature;
- to build a realistic parametric strain model that could be compared with strain data and, then, to estimate concrete parameters related to each strain component;
- to provide evidence to support the inferences made and the results obtained.

This study has been successful in terms of achieving the purposes intended.

Firstly, a quite good understanding of the structural scheme and construction operations of the Queensferry Crossing was developed. It proved to be determinant to understand and interpret the SHM data provided (*Chapter 2*).

However, the main subject of this work was to carry out the tower concrete parameters estimation applying two methods, the Least Squares Analysis and the Bayesian inference. The definition of the parametric model was a crucial step to complete this task. In particular, it was possible to define the stress function (*Par. 6.1*) and, consequently, the creep function (*Par. 6.2)* only when the data relating to the weight (and date of lifting) of each deck segment were provided.

After having defined the parametric model of the strain, LSA and BA were performed. The former method demonstrates the lack of precision in the estimation of the parameters (*Par. 7.1*). The values that come out of the Least Square regression analysis are totally meaningless, from an engineering point of view. However, the implemented algorithm based on the Bayesian inference proved to be helpful for the parameters estimation (*Par. 7.2*). The definition of the prior distributions, founded on the engineering knowledge of the parameters, was decisive for the completion of the task. In this way, the author found the results through comparison between the a priori knowledge of the parameters and that obtained a posteriori, thanks to the implemented Bayesian method. The good results

(considering all the uncertainties) allowed me to validate the algorithm that I had developed. In particular, the correlation between the strain and temperature was successfully estimated. This led to the definition of the temperature compensated strain trend, that shows the overall contracting behaviour of the tower concrete, as expected. The final analytical calculations does nothing but support the results obtained with the Bayesian approach.

8.1 Summary of key findings

The first key finding of the case study was that the strain signals from the SHM system over the full time period highlighted that there were three distinct phases during this period. Through quantitative and qualitative analyses of the data from each of these time periods construction operations were identified. In the first two periods, tower construction and deck erection occurred. In the final time period no major construction activity was occurring on the main span. Evidence for these conclusions was provided by analysis of the signal data registered on the four sides of the CT: as deck was lifted on the North-South direction, the elastic jumps of strain are visible only on the North and South sides sensors, while West and East strain gages do not show this behaviour.

Secondly, the clear correlation between strain and temperature was highlighted. Chapter 5 exhaustively explains how both daily and seasonal temperature variation affects strain variation. It is also interesting to see this effect following the path of the sun (*Par. 5.1.3*).

Finally, a quantitative analysis was performed with the application of the two estimation methods. This led to find that LSA fails in the parameters evaluation, due to the uncertainty between the stress and creep functions, which are dependent on each other. In contrast, BA estimation process led to a good result of the estimation. The values found for each parameter and their uncertainties meet the expectations. The thermal coefficient α has been particularly well-estimated (~ 10,9 με/°C), allowing to perform a temperature compensation of the strain data. This was important because it allows seeing how the concrete deforms without the temperature influence. Temperature compensated strain allows to do calculations to understand the state of stress in the concrete.

8.2 Recommendations for future work

The identification of the effect of construction operations on the SHM data and concrete parameters estimation could be used as a starting point for further analysis. Therefore, a recommendation for future work would be to use the findings to identify a more precise state of stress in structural members, e.g. by building a finite element model. This may allow for some assumptions made during the design process to be confirmed or disproved. It could also enable more efficient designs in the future if stresses in members were significantly less than expected. Thus, investigation of the possible over design of large infrastructure projects to ensure safety could be explored using SHM data during construction or operation as starting point.

Future case studies could be carried out on the Queensferry Crossing, starting from the examination of the other two towers or throughout the operational lifecycle, to investigate the operational behaviour of the bridge. The SHM deployment as discussed previously is extensive. Thus, there are many possible avenues of investigation that could be carried out, as a focus of the case study.

Finally, the long term behaviour of the bridge could be studied. Of further interest would be an investigation of the state of the cable stays after years' service. Using the strain gauges on the cables analysis could be carried out to determine if they are elongating.

For any possible future case studies on the bridge it would be advantages to have access to data detailing the wind speed and direction, which could be used in conjunction with the temperature readings to remove environmental noise form the data.

8.3 Conclusions from work

The conclusion that can be finally drawn is that SHM data proved to be a successful instrument to examine the behaviour of the investigated elements of a structure. In spite of the uncertainties about the function that were built to construct the model, very significant values of the parameters were estimated. However, engineering knowledge and judgement is necessary in order to use properly data collected on a structure. Indeed, the identification of a strain model that would have been descriptive of the concrete behaviour during its first three years was a key point to perform the parameters estimation. If one of the strain contributes had been neglected, the estimation of the parameters would

have been wrong, as that contribute would have been assigned to another (or more) parameter (thus resulting in an overestimated value).

Moreover, the application of two estimation methods allowed me to infer the differences between a deterministic regression analysis (LSA), which approximates the solution neglecting any kind of errors between the independent variables, and a statistics inference, which considers the uncertainties of the model and the observations. In this task, engineering judgement is determinant, as the posterior information is connected to the prior knowledge on the parameters.

In conclusion, SHM is a powerful way to control, monitor, infer and analyse our structure, provided that output data are processed in the right way.

Acknowledgements

This project has been carried out within a collaboration between Politecnico di Torino and University of Strathclyde represented respectively by prof. Rosario Ceravolo and prof. Daniele Zonta.

I would like to thank professor Ceravolo who gave me the possibility to take part in the project that was totally developed in Scotland. I also want to thank my supervisor at the University of Strathclyde, prof. Zonta, and the PhDs, Andrea Verzobio and Andrea Maroni, who provided me all the material useful for the project realization and followed the development of the thesis work from the beginning until its conclusion.

Secondly, I would like to mention and thank the support, both economical and emotional, that I received from my family and, especially, my parents, without which I would not have been able to complete the project. I owe them the possibility to have taken part in this work.

Lastly, I wish to offer a particular word of thank to my "special" colleague and girlfriend, Greta Lentini, with whom I completely shared this experience. She no doubt helped make this period "lighter" and became a point of reference throughout all these months, supporting me in difficult times.

References

AKTAN A. E., HELMICKI A. J. AND HUNT V. J. - *Issues in health monitoring for intelligent*, Smart Materials and Structures 7, 1998.

ANDERSON G. R. JR. [ET AL.] - *Falling Down*, 2007.

ANGUS EWAN - *How integrated technology is driving safety and efficiency on the Forth Road Bridges*, 2018.

BBC - *BBC* - 30 August 2017. - www.bbc.co.uk.

BOLSTAD WILLIAM M. - *Understanding Computational Bayesian Statistics*, 2010.

BROUGHTON K. - *The Queensferry Crossing - Demonstrating that size is no object to off-site construction.*

CARTER M. [ET AL.] - *Design of the Forth replacement crossing, Scotland*, Proceedings of the Institution of Civil Engineers - Bridge Engineering, 2010.

CARTER M. [ET AL.] - *Queensferry Crossing*, The Arup Journal, 2017.

CHANG P. C., FLATAU A. AND LIU S. C. - *Health Monitoring of Civil Infrastructure*, 2003.

CURRAN P. [ET AL.] - *Queensferry Crossing – Cable Stayed Bridge Deck and Cables – Design and Construction*, Proceedings of the Institution of Civil Engineers - Bridge Engineering, 2018.

DEDMAN B. - *I-35 Bridge Was Rated among the Nation's Worst*, 2007.

DOEBLING SCOTT W, FARRAR CHARLES R AND PRIME MICHAEL B. - *A Summary Review of Vibration-Based Damage Identification Methods*, Identification Methods, The Shock and Vibration Digest, Vol. 30, pp. 91-105, 1998.

EN 1992-1-1:2004.

FARRAR C. R. AND WORDEN K. - *An introduction to structural health monitoring*, Philosophical Transactions of the Royal Society A, 2007.

FRANGOPOL D. M. AND MESSERVEY T. B. - *Maintenance Principles for Civil Structures*, Encycolpedia of Structural Health Monitoring [Boller, Chang and Fujino], 2009.

FRC FORTH REPLACEMENT CROSSING - *Forth Replacement Crossing Project Update March 2013,* Transport Scotland, 2013.

HUA-PENG CHEN, YI-QING NI - *Structural Health Monitoring of Large Civil Engineering Structures*, 2018.

JOHNSTON D, CHISHOLM A.J AND TRAPP W - *The Queensferry Crossing - construction of the caisson foundations*, Geotechnical Engineering for Infrastructure and Development, 2015.

KÆRN JENS CHRISTIAN, HANSEN JOHN ELNEGAARD - *Queensferry crossing cable-stayed composite bridge*, Vol. 1, pp. 4143-4152, 2017.

KARBHARI M. V. - *Design principles for civil structures*, Encyclopedia of Structural Health Monitoring [Boller, Chang and Fujino], 2009.

KITCHING RUBY - *Smart Infrastructure | Forth Road Bridge*, New Civil Engineering, https://www.newcivilengineer.com/tech-excellence/smart-infrastructure-forth-road-bridge/10021401.article, 2017.

KO J. M., NI Y. Q. - *Technology developments in structural health monitoring of large-scale bridges*, Engineering Structures 27, 2005.

KUTNER MICHAEL H., NACHTSHEIM CHRISTOPHER J., NETER JOHN, LI WILLIAM - *Applied Linear Statistical Models*, 2005.

LAMB RICHARD H. - *The Construction Of The Queensferry Crossing*, 2018.

LYNCH JEROME P., LOH KENNETH J - *A Summary Review of Wireless Sensors and Sensor Networks for Structural Health Monitoring*, The Shock and Vibration Digest, Vol. 2, pp. 91-128, 2006.

MARTIN M., CLIMIE D., CURRAN P. - *World record-breaking bridge*, 2017.

MONACO PIETRO - *La viscosità nelle strutture in calcestruzzo armato*, Lecce, 2012.

NIST/SEMATECH - *Least Squares*, e-Handbook of Statistical Methods, 2012.

RAMBOLL A - *SHMS system principle arrangement static strain guage rosette,* FORTH REPLACEMENT CROSSING - DESIGN JOINT VENTURE, 2015.

RAMBOLL B - *SHMS system principle arrangement static strain guage single gauge,* FORTH REPLACEMENT CROSSING - DESIGN JOINT VENTURE, 2015.

RAMBOLL C - *Main crossing structural health monitoring system central tower at +7.5 OD*, FORTH REPLACEMENT CROSSING - DESIGN JOINT VENTURE, 2013.

RAMBOLL D - *SHMS Sensory system, static strain gauges installed at S2,S1,ST,CT,NT,N1 and N2 design report*, FORTH REPLACEMENT CROSSING - DESIGN JOINT VENTURE, 2013.

RAMBOLL E - 2013.

RAMBOLL I - Central Tower Foundation, 2015.

RAMBOLL II - *Main crossing South tower foundation general arrangement*, FORTH REPLACEMENT CROSSING - DESIGN JOINT VENTURE, 2015.

RAMBOLL - *SHMS – Sensory System Corrosion Sensors Design Report S*, FORTH REPLACEMENT CROSSING - DESIGN JOINT VENTURE, 2013.

ROMBERG M. [ET AL.] - *Queensferry Crossing: towers, piers and abutments – design and construction*, Proceedings of the Institution of Civil Engineers - Bridge Engineering, 2018.

SCHERIE NICOL - *The Forth Replacement Crossing First Principles*, Parliament Scotland,http://www.parliament.scot/Research%20briefings%20and%20fact%20sheets/SB_10-17.pdf, 19 February 2010.

SHACKMAN LAWRENCE, CLIMIE DAVID - *Planning and procurement of the Queensferry Crossing in Scotland*, Proceedings of the Institution of Civil Engineers - Civil Engineering, Vol. 169, pp. 161-168, 2016.

STREJC V. - *Least squares parameter estimation*, Automatica, Vol. 16, pp. 535-550, 1980.

TORSTEN HOFFMANN - *Suncalc*, Suncalc.org. - https://www.suncalc.org/#/56.0043.

TRANSPORT SCOTLAND - *Queensferry Crossing ARC* - http://www.queensferrycrossingarc.co.uk/explore, 2014.

TRANSPORT SCOTLAND - *Quensferry Crossing ARC* - http://www.queensferrycrossingarc.co.uk/build-story/north-approach, 2018.

WATT DAVID - *QUEENSFERRY CROSSING: Vision to Reality*, Isle of Man: Lily Publications, 2017.

Annex 1

In this section, the plots presenting strain data registered on the two Flanking Towers have been reported.

North Tower

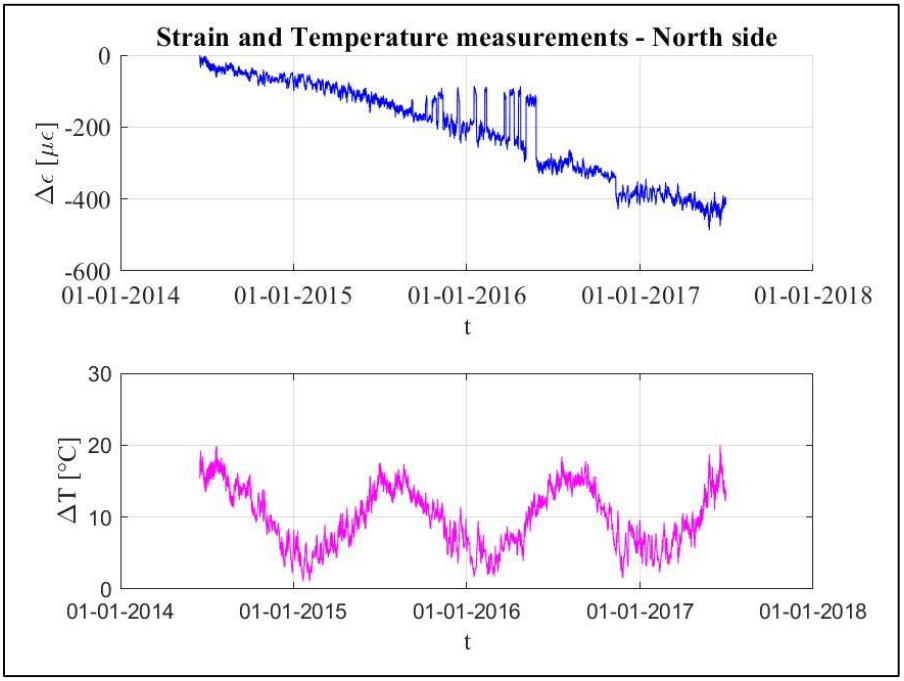

Figure A. 1. Raw strain measurements and temperature data from CT-OD7.5-S-STR-S-1342 (North side)

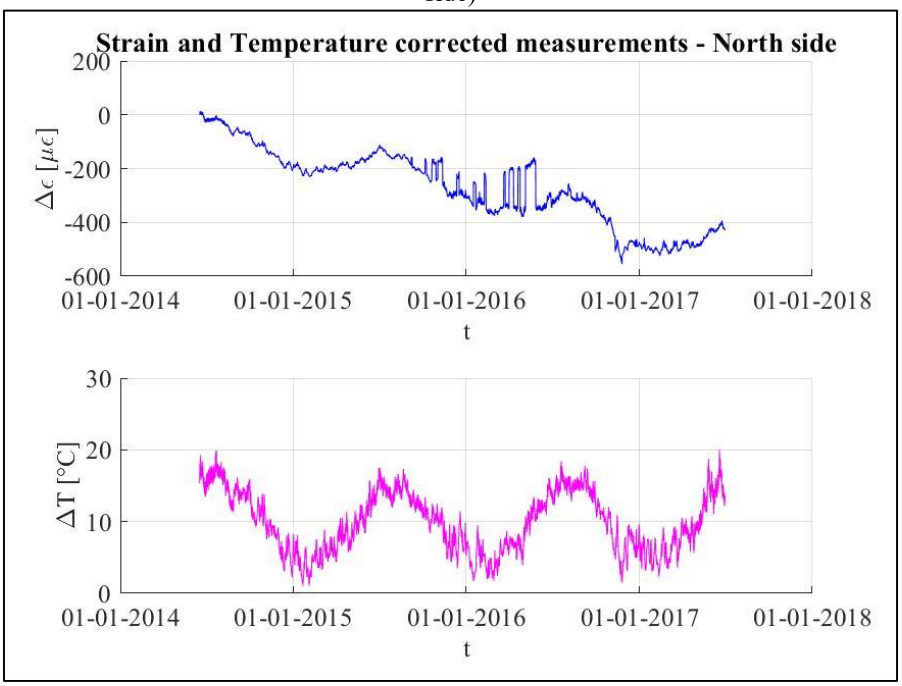

Figure A. 2. Corrected strain measurements and temperature data from CT-OD7.5-S-STR-S-1342 (North side)

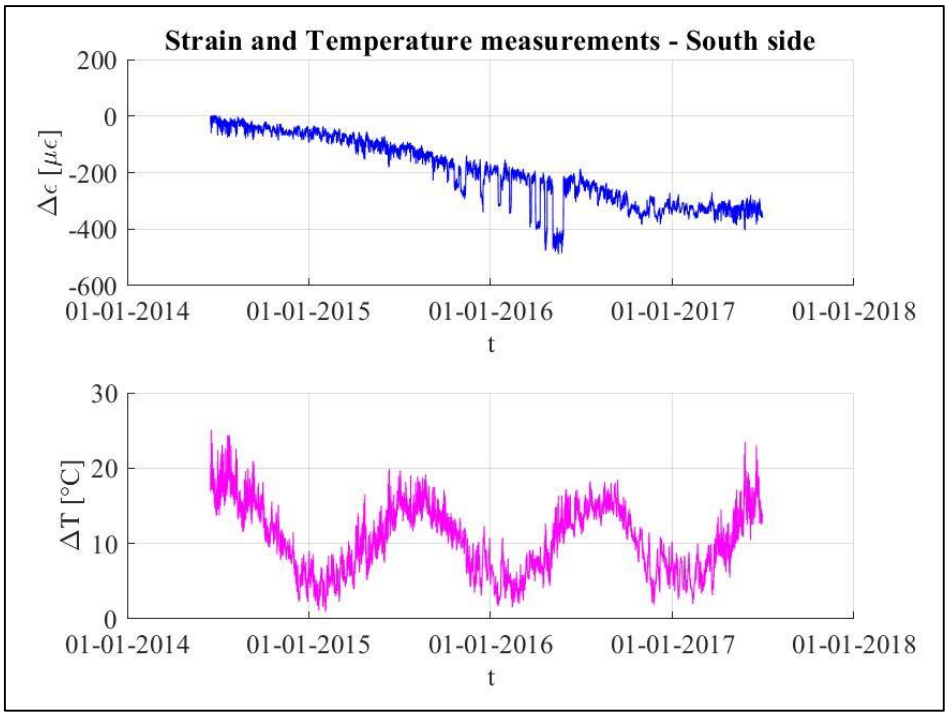

Figure A. 3. Raw strain measurements and temperature data from CT-OD7.5-S-STR-S-1346 (South side)

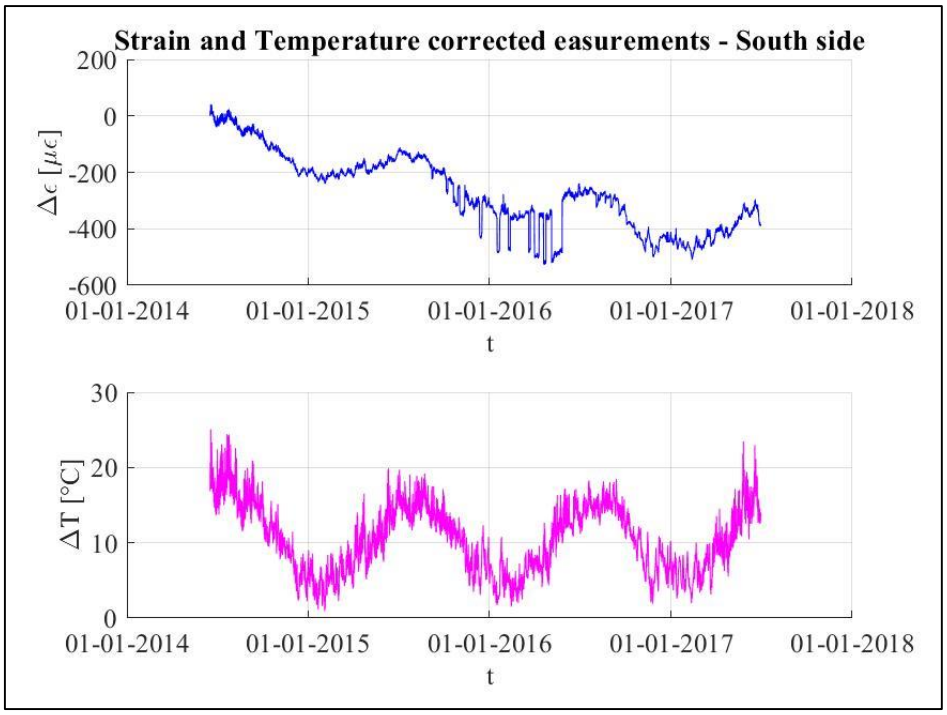

Figure A. 4. Corrected strain measurements and temperature data from CT-OD7.5-S-STR-S-1346 (South side)

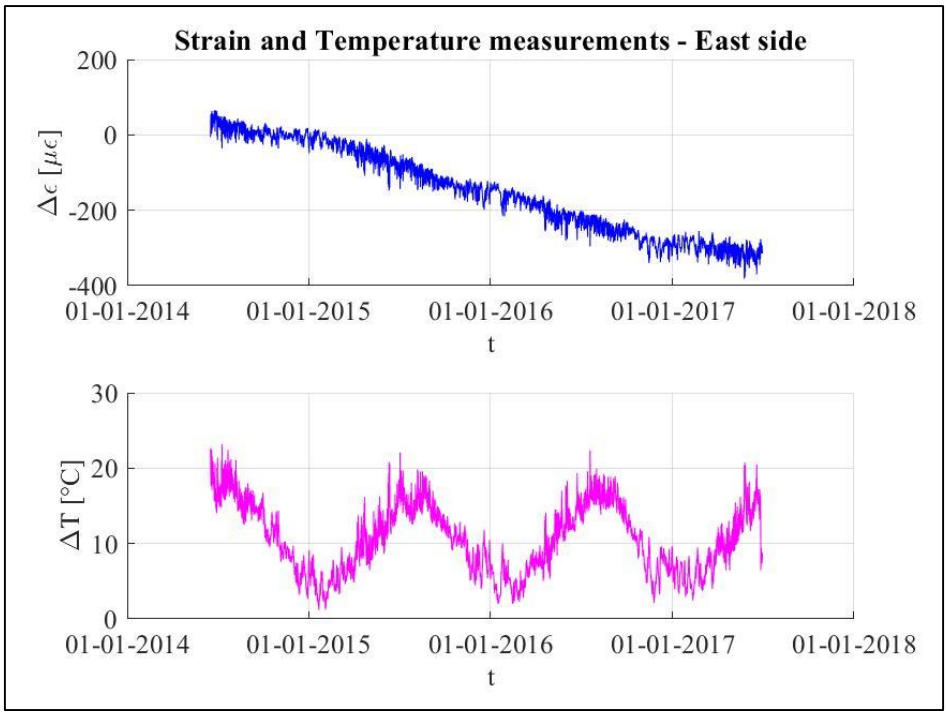

Figure A. 5. Raw strain measurements and temperature data from CT-OD7.5-S-STR-S-1344 (East side)

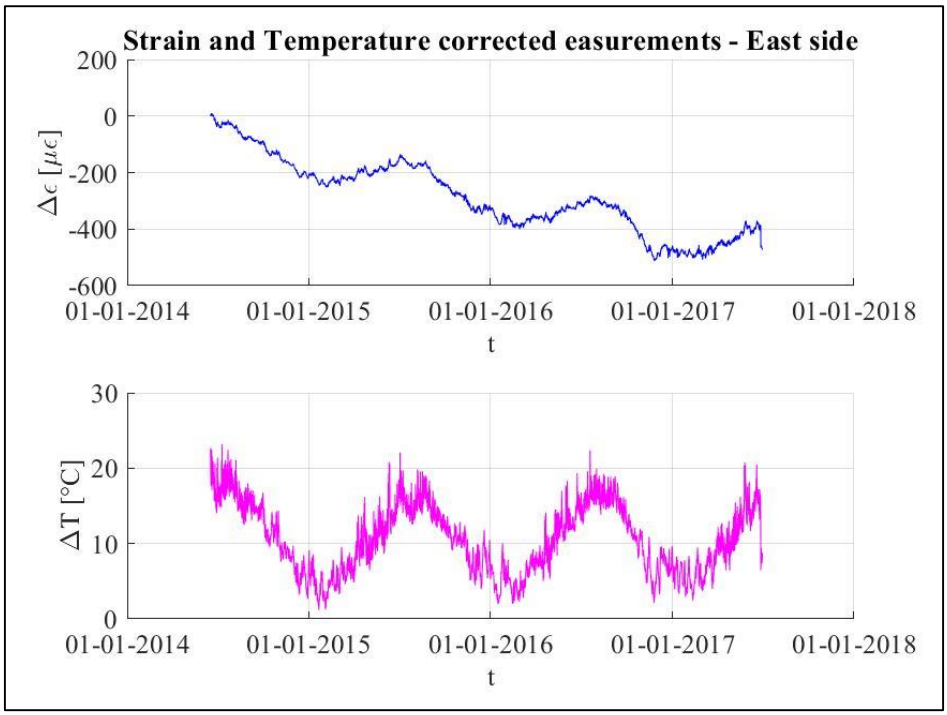

Figure A. 6. Corrected strain measurements and temperature data from CT-OD7.5-S-STR-S-1344 (East side)

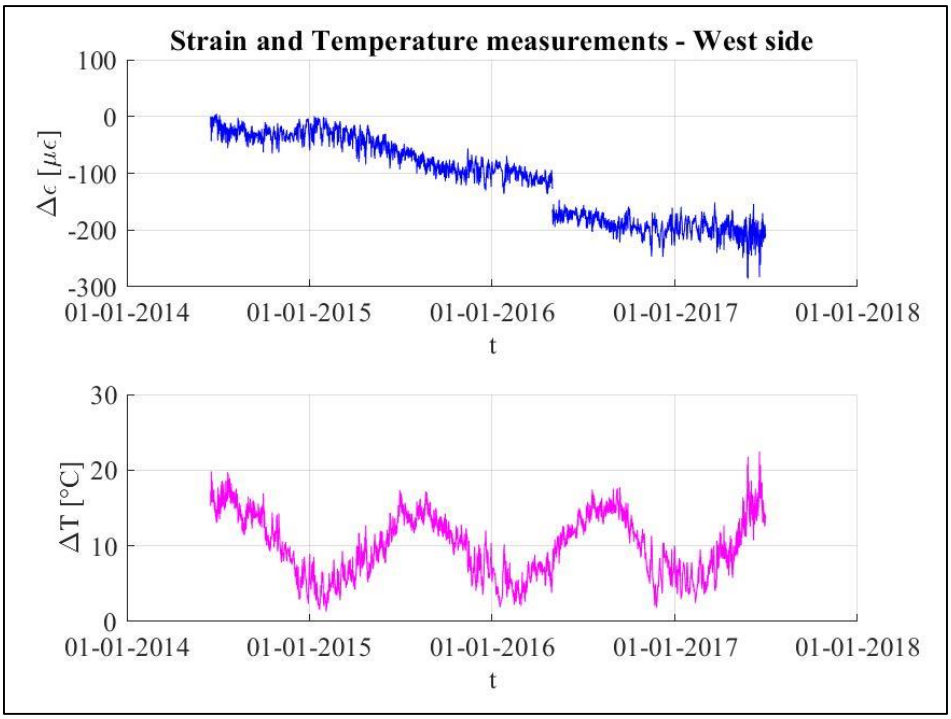

Figure A. 7. Raw strain measurements and temperature data from CT-OD7.5-S-STR-S-1340 (West side)

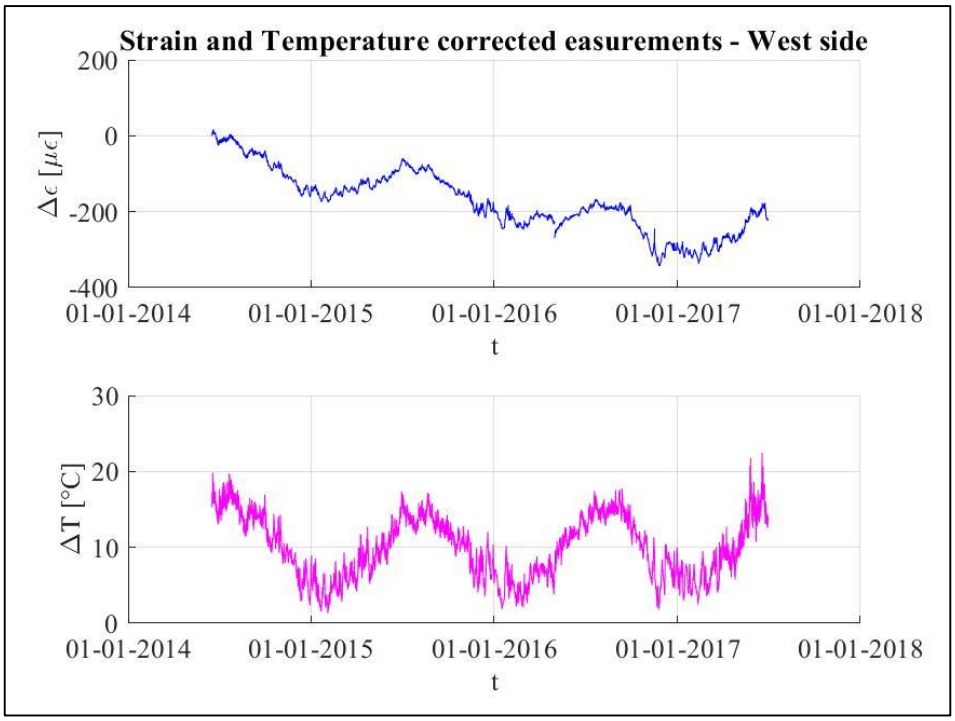

Figure A. 8. Corrected strain measurements and temperature data from CT-OD7.5-S-STR-S-1340 (West side)

South Tower

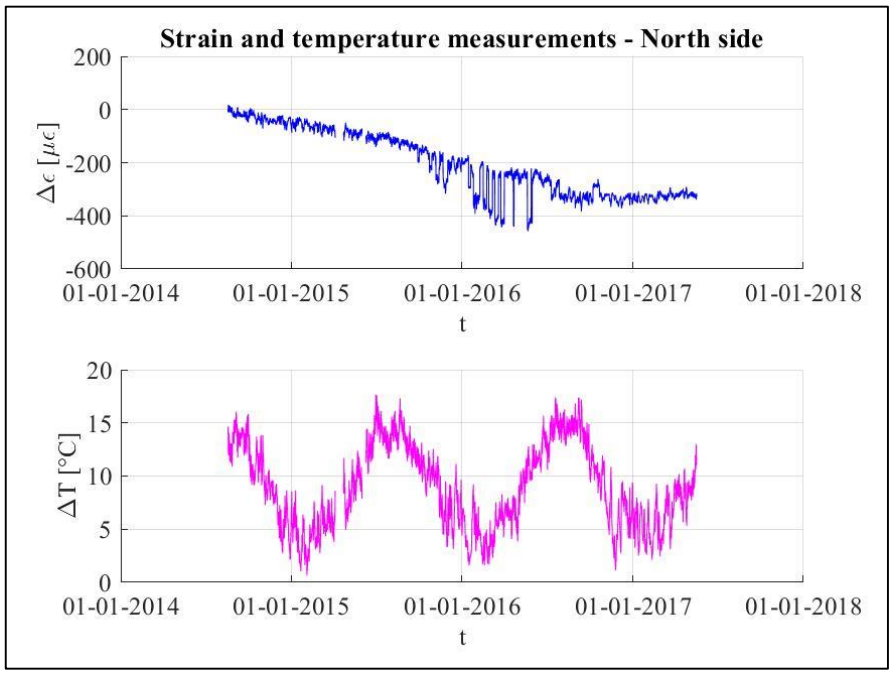

Figure A. 9. Raw strain measurements and temperature data from CT-OD7.5-S-STR-S-1078 (North side)

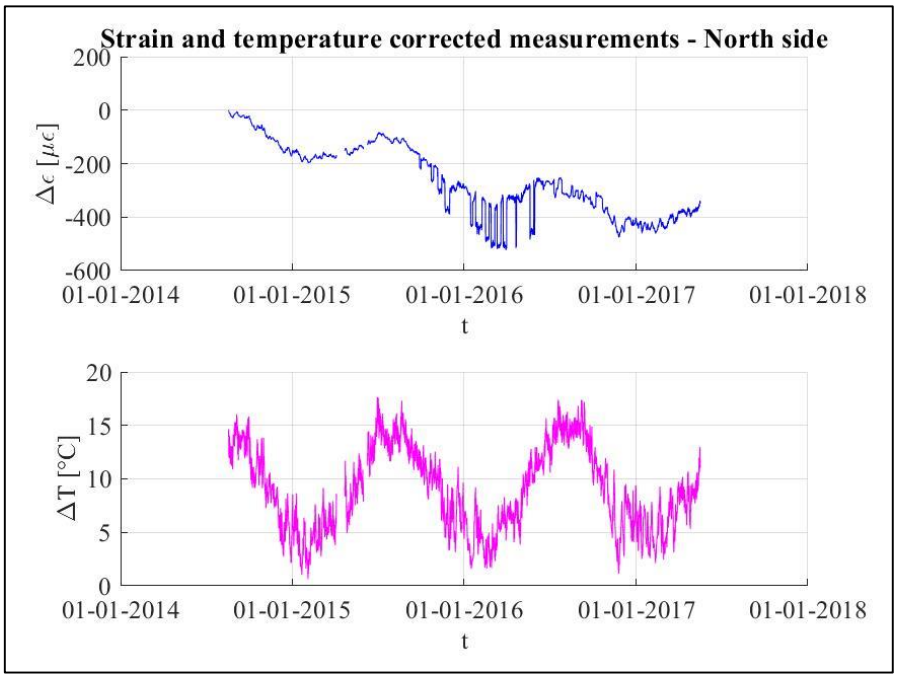

Figure A. 10. Corrected strain measurements and temperature data from CT-OD7.5-S-STR-S-1078 (North side)

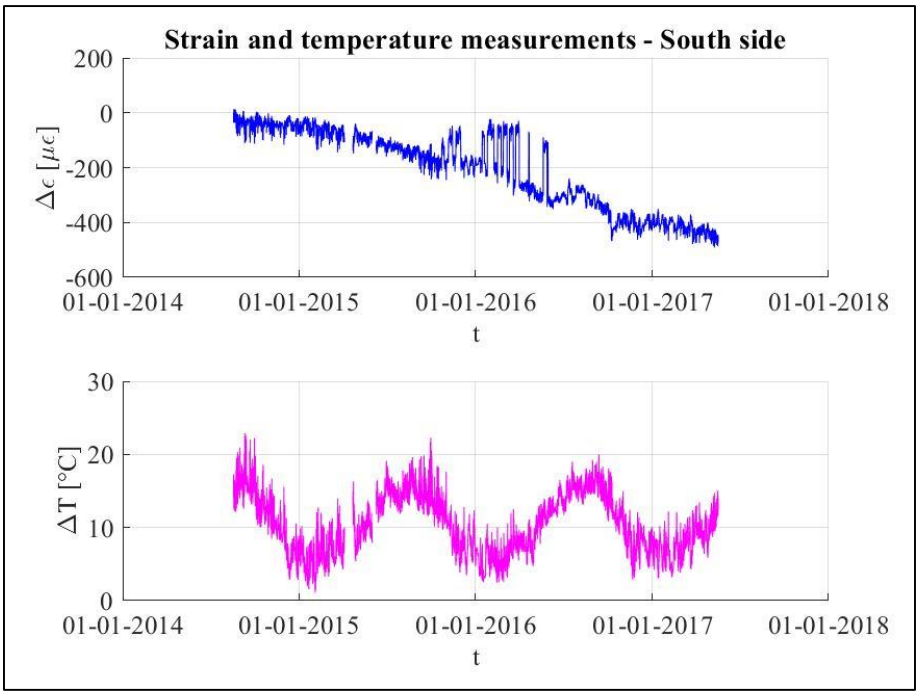

Figure A. 11. Raw strain measurements and temperature data from CT-OD7.5-S-STR-S-1082 (South side)

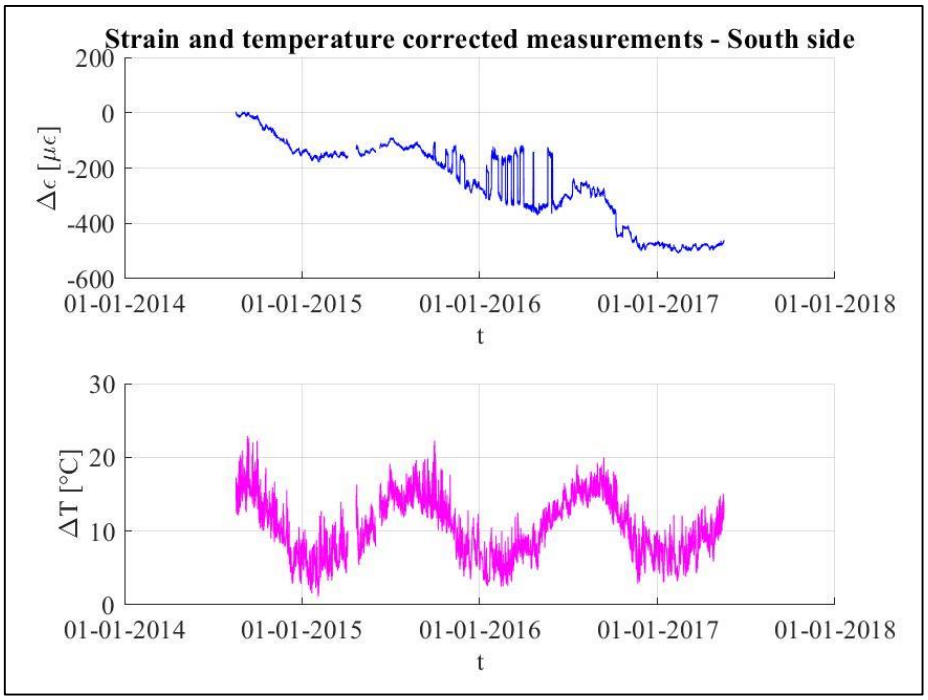

Figure A. 12. Corrected strain measurements and temperature data from CT-OD7.5-S-STR-S-1082 (South side)

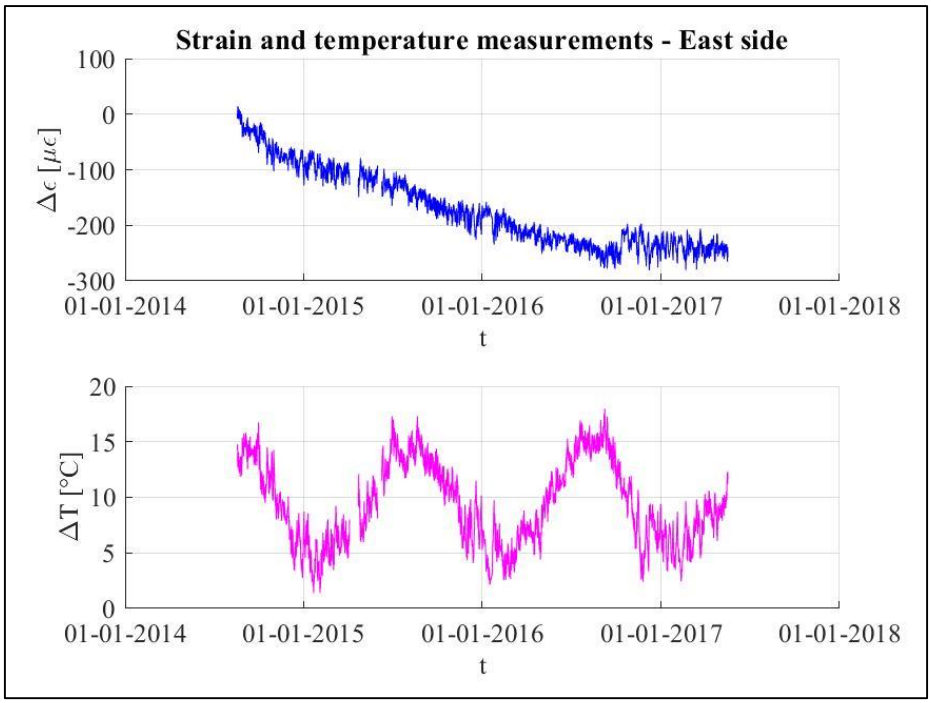

Figure A. 13. Raw strain measurements and temperature data from CT-OD7.5-S-STR-S-1080 (East side)

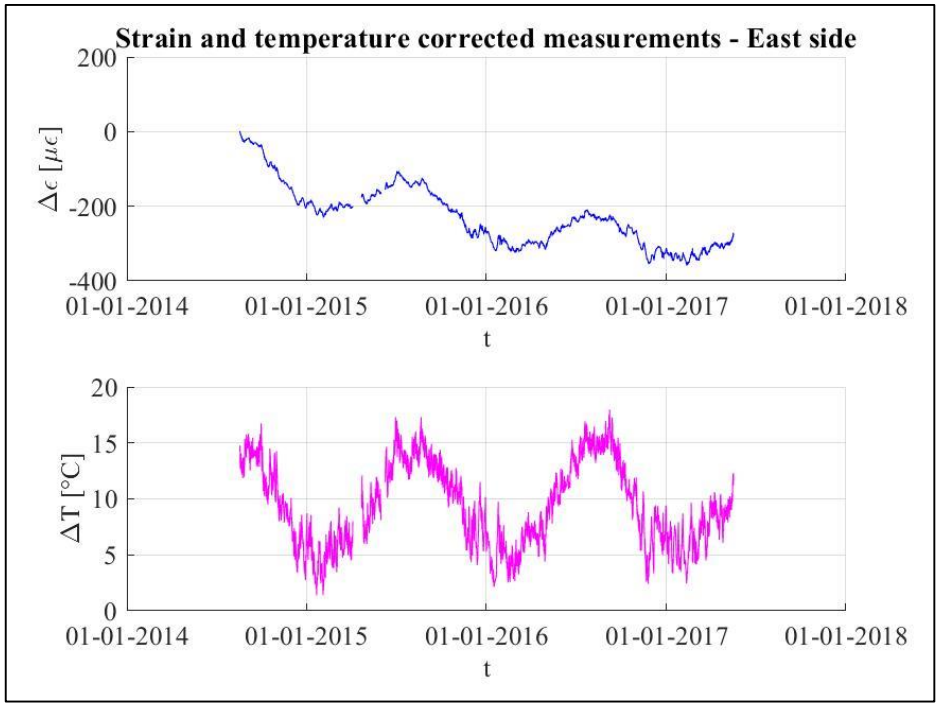

Figure A. 14. Corrected strain measurements and temperature data from CT-OD7.5-S-STR-S-1080 (East side)

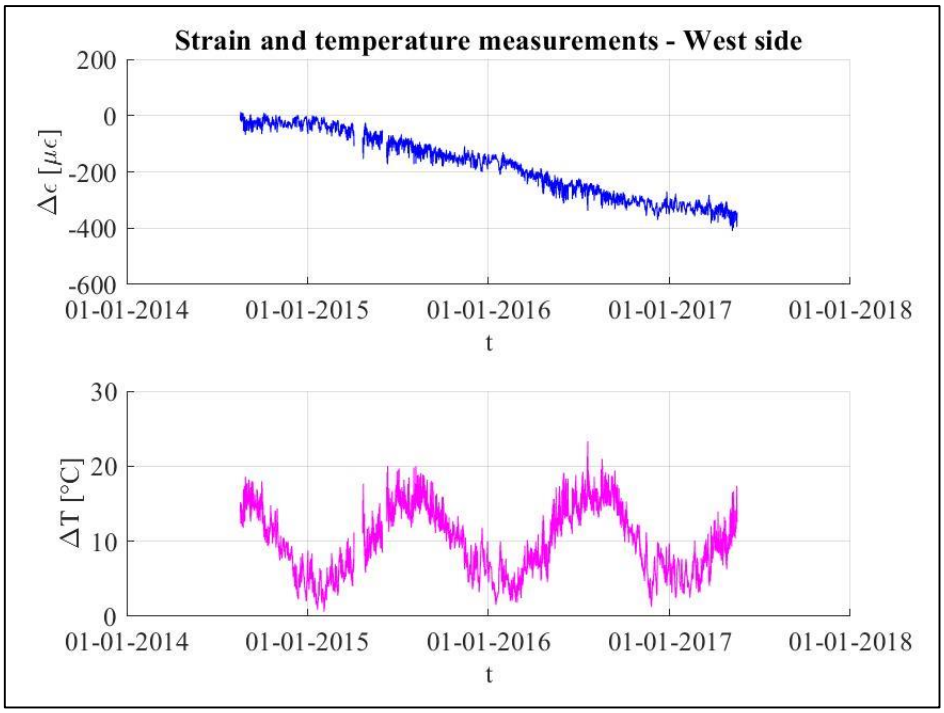

Figure A. 15. Raw strain measurements and temperature data from CT-OD7.5-S-STR-S-1076 (West side)

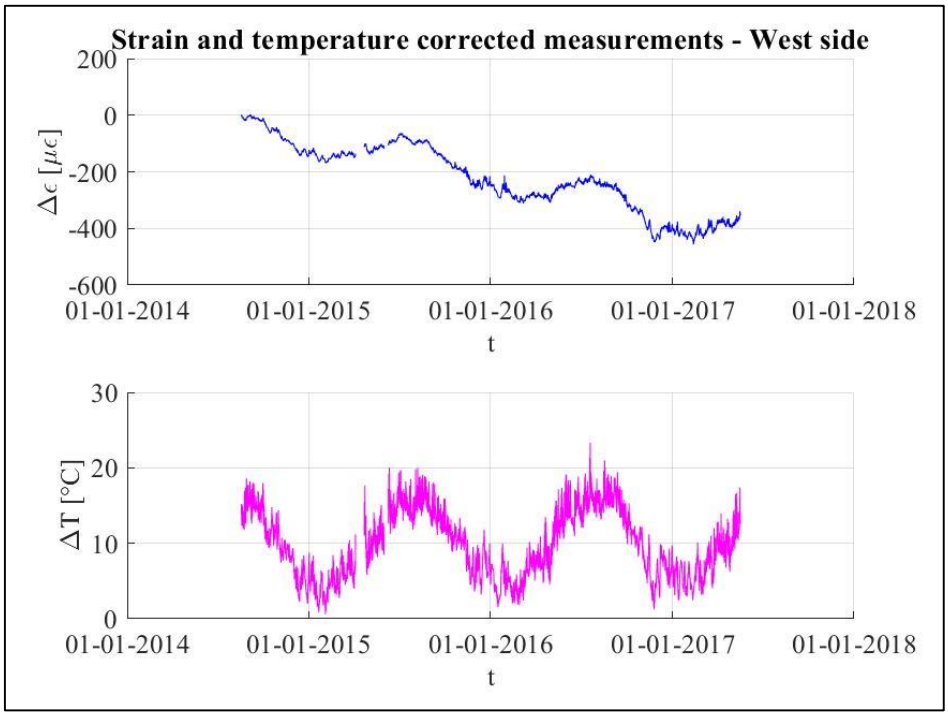

Figure A. 16. Corrected strain measurements and temperature data from CT-OD7.5-S-STR-S-1076 (West side)

Annex 2

In this Section, construction data including Centre Tower and Deck segments lift dates and weights have been reported.

Table A. 1. Tower segments lift data

Tower Segment	Level [m]	Pour date	TS Weight [kN]
	1	Top of foundation	
	1,1	Top of blinding	
TS1	5,1	09/09/2013	8191,94
TS2	9,1	18/10/2013	7935,89
TS3	13,1	29/11/2013	7679,85
TS4	17,1	09/01/2014	7423,81
TS5	21,1	28/01/2014	7167,77
TS6	25,1	10/02/2014	6911,72
TS7	29,1	28/02/2014	6826,33
TS8	33,1	18/03/2014	6890,23
TS9	37,1	30/03/2014	6911,47
TS10	41,1	11/04/2014	6890,02
TS11	45,1	22/04/2014	6697,93
TS12	49,1	02/05/2014	6356,53
TS13	53,1	16/05/2014	6015,14
TS14	57,1	04/06/2014	6921,22
TS15	58,967	14/06/2014	2929,68
TS16/1	60,217	02/07/2014	1423,60
TS16/2	61,967	27/07/2014	1993,04
TS16/3	63,717	27/07/2014	1993,04
TS17	67,717	20/08/2014	4533,62
TS18	71,717	07/09/2014	4489,79
TS19	75,717	25/09/2014	4445,96
TS20	79,717	12/10/2014	4402,13
TS21	83,717	29/10/2014	4358,30
TS22	87,717	06/11/2014	4314,47
TS23	91,717	18/11/2014	4182,98
TS24	95,717	27/11/2014	4053,02
TS25	99,717	04/12/2014	4012,27
TS26	103,717	18/12/2014	3971,51
TS27	107,717	17/01/2015	3930,76
TS28	111,717	29/01/2015	3890,00
TS29	115,717	08/02/2015	3849,25
TS30	119,717	14/02/2015	3731,60
TS31	123,717	22/02/2015	3516,86
TS32	127,717	03/03/2015	3381,53
TS33	131,717	11/03/2015	3345,77
TS34	135,717	21/03/2015	3310,02

Tower Segment	Level [m]	Pour date	TS Weight [kN]
TS35	139,717	28/03/2015	3274,26
TS36	143,717	04/04/2015	3238,50
TS37	147,717	14/04/2015	3305,90
TS38	151,717	08/05/2015	3439,43
TS39	155,717	19/05/2015	3434,83
TS40	159,717	05/06/2015	3329,59
TS41	163,717	18/06/2015	3225,35
TS42	167,717	29/06/2015	3122,09
TS43	171,717	12/07/2015	3019,81
TS44	175,717	29/07/2015	2918,52
TS45	179,717	14/08/2015	2818,21
TS46	183,717	02/10/2015	2718,89
TS47	187,717	08/10/2015	2620,56
TS48	191,717	15/10/2015	2523,21
TS49	195,717	20/10/2015	2426,85
TS50	199,717	28/10/2015	2331,47
TS51	203,717	02/11/2015	2237,07
TS52	207,717	20/11/2015	2143,67
TS53	208,774	25/11/2015	536,26
TS54	210,717	03/12/2015	978,91

Table A. 2. Deck segments lift data (South side segments in red, North side segments in blue)

Deck Segment	Length [m]	Date of lifting	Deck Segment Weight [kN]
CTS_	18,919	12/10/2015	15527
CTN_	18,918	12/10/2015	15456
CS01	11,44601	12/10/2015	5951
CN01	11,44601	12/10/2015	5983
CS02	16,20805	21/10/2015	7886
CN02	16,20904	26/10/2015	7774
CS03	16,2091	04/11/2015	7560
CN03	16,20909	07/11/2015	7458
CS04	16,21018	26/11/2015	7597
CN04	16,20916	03/12/2015	7503
CS05	16,20927	15/12/2015	7434
CN05	16,20926	07/01/2016	7596
CS06	16,20939	12/01/2016	7445
CN06	16,20937	16/01/2016	7408
CS07	16,20852	21/01/2016	7446
CN07	16,20951	06/02/2016	7418
CS08	16,20968	17/02/2016	7421
CN08	16,20866	28/02/2016	7428
CS09	16,20886	07/03/2016	7323
CN09	16,20884	15/03/2016	7374
CS10	16,20809	18/03/2016	7400

Deck Segment	Length [m]	Date of lifting	Deck Segment Weight [kN]
CN10	16,20906	25/03/2016	7387
CS11	16,20834	03/04/2016	7490
CN11	16,20731	09/04/2016	7491
CS12	16,2076	15/04/2016	7422
CN12	16,20858	22/04/2016	7420
CS13	16,20793	12/05/2016	7253
CN13	16,2069	19/05/2016	7313
CS14	16,20627	01/06/2016	7502
CN14	16,20723	07/06/2016	7564
CS15	16,20762	19/06/2016	7544
CN15	16,20659	25/06/2016	7605
CS16	16,207	30/06/2016	7508
CN16	16,20696	07/07/2016	7705
CS17	16,20643	18/07/2016	7543
CN17	16,20639	27/07/2016	7684
CS18	16,20589	04/08/2016	7492
CN18	16,20686	20/08/2016	7544
CS19	16,20744	06/09/2016	7787
CN19	16,20637	09/09/2016	7830
CLS_	6,101795	09/10/2016	3403
CLN_	6,102778	11/11/2016	3290

Annex 3

In this section, the results coming from Bayesian estimation on strain data registered by the strain gages at the corners (North-West, North-East, South-East, South-West) of the section have been reported. As a summary duty, only the estimation results together with the temperature compensated strain plot have been included.

North-West sensor

Sensor (location)	E[ε_0] [με]	E[1/E] [1/MPaE6]	E[ϕ_∞/E] [1/MPaE6]	E[$\varepsilon_{s,\infty}$] [με]	E[α] [με/°C]	E[σ_{LH}] [με]
CT-OD7.5-S-STR-S-1193	-35	25,14	58,85	-281	12,73	30

Table A. 3. CT-OD7.5-S-STR-S-1193 (North-West) BA parameters estimated values

Std[ε_0] [με]	Std[1/E] [1/MPaE6]	Std[ϕ_∞/E] [1/MPaE6]	Std[$\varepsilon_{s,\infty}$] [με]	Std[α] [με/°C]
2	0,10	1,92	12	0,22

From the estimated parameters we can calculate:

- E=39784 MPa;
- φ_∞=2,34.

Using the values obtained with this approach, the temperature compensated strain can be evaluated.

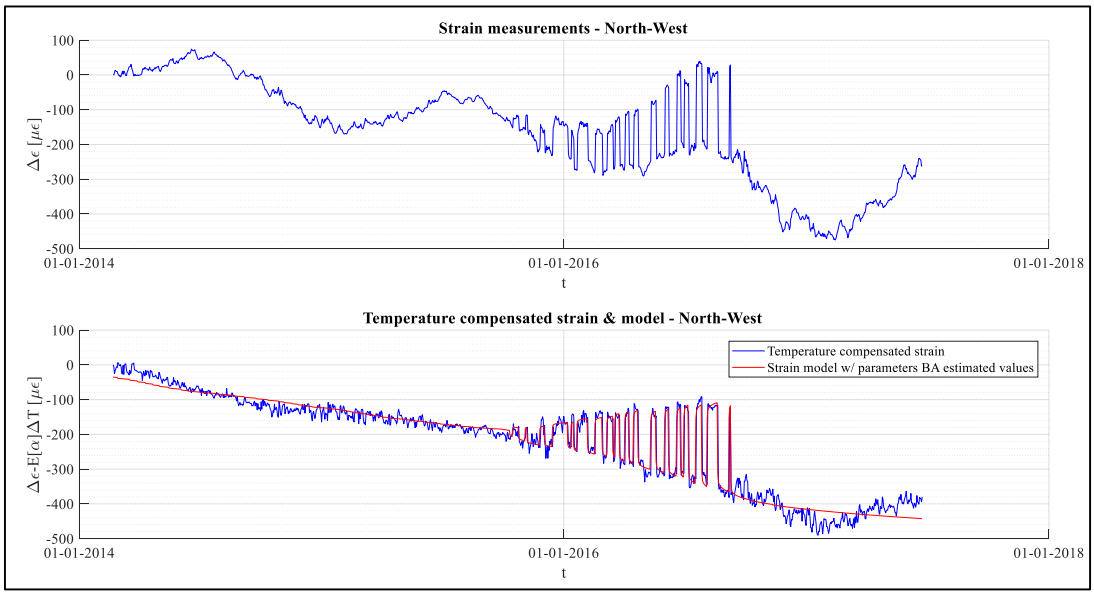

Figure A. 17. Temperature compensated measured strain and model with the parameters BA estimated values for the North-West sensor

At the end of the process, we obtain a posterior distribution for each parameter that is compared with the prior one in the following picture:

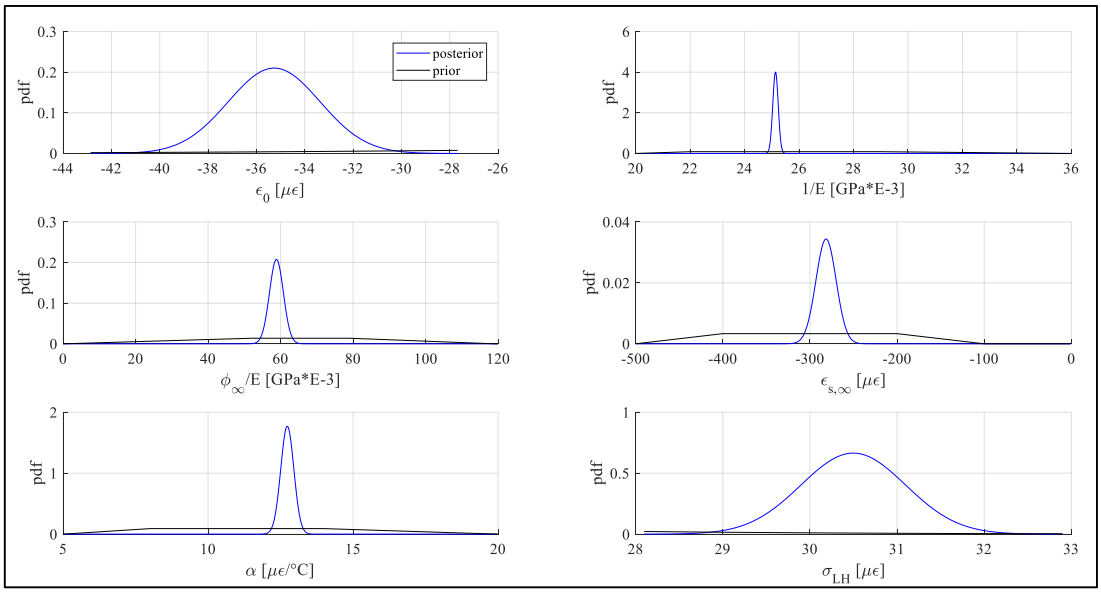

Figure A. 18. Prior (black) vs. Posterior (blue) distributions for the North-West sensor

North-East sensor

Sensor (location)	E[ε₀] [με]	E[1/E] [1/MPaE6]	E[ϕ∞/E] [1/MPaE6]	E[εs,∞] [με]	E[α] [με/°C]	E[σLH] [με]
CT-OD7.5-S-STR-S-1195	-30	25,09	49,18	-133	13,09	27

Table A. 4. CT-OD7.5-S-STR-S-1195 (North-East) BA parameters estimated values

Std[ε₀] [με]	Std[1/E] [1/MPaE6]	Std[ϕ∞/E] [1/MPaE6]	Std[εs,∞] [με]	Std[α] [με/°C]
2	0,06	2,63	20	0,19

From the estimated parameters we can calculate:

- E=39862 MPa;
- φ_∞=1,96.

Using the values obtained with this approach, the temperature compensated strain can be evaluated.

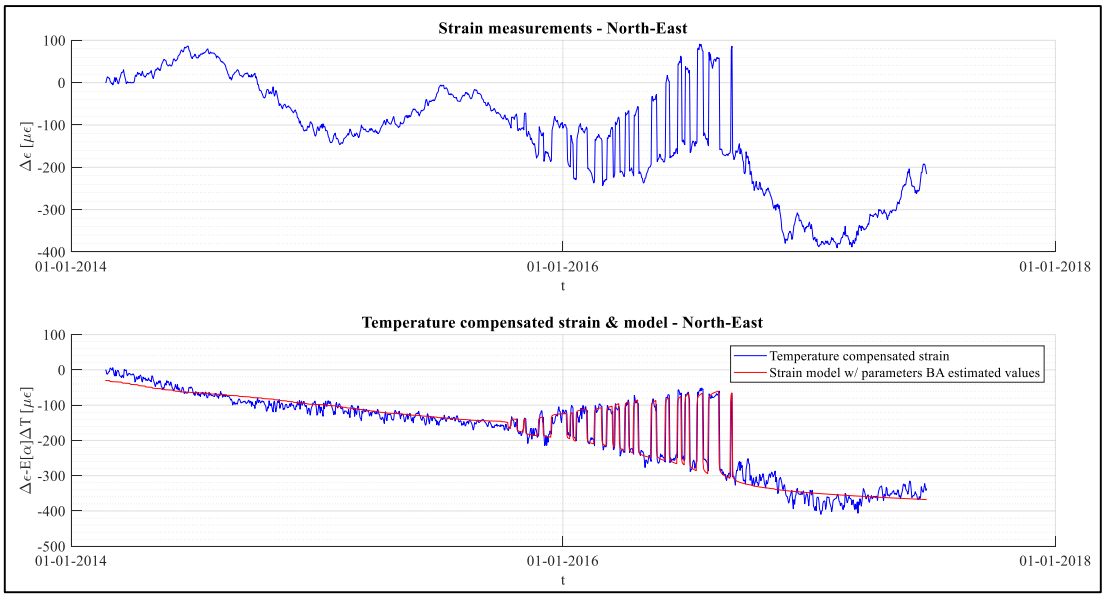

Figure A. 19. Temperature compensated measured strain and model with the parameters BA estimated values for the North-East sensor

At the end of the process, we obtain a posterior distribution for each parameter that is compared with the prior one in the following picture:

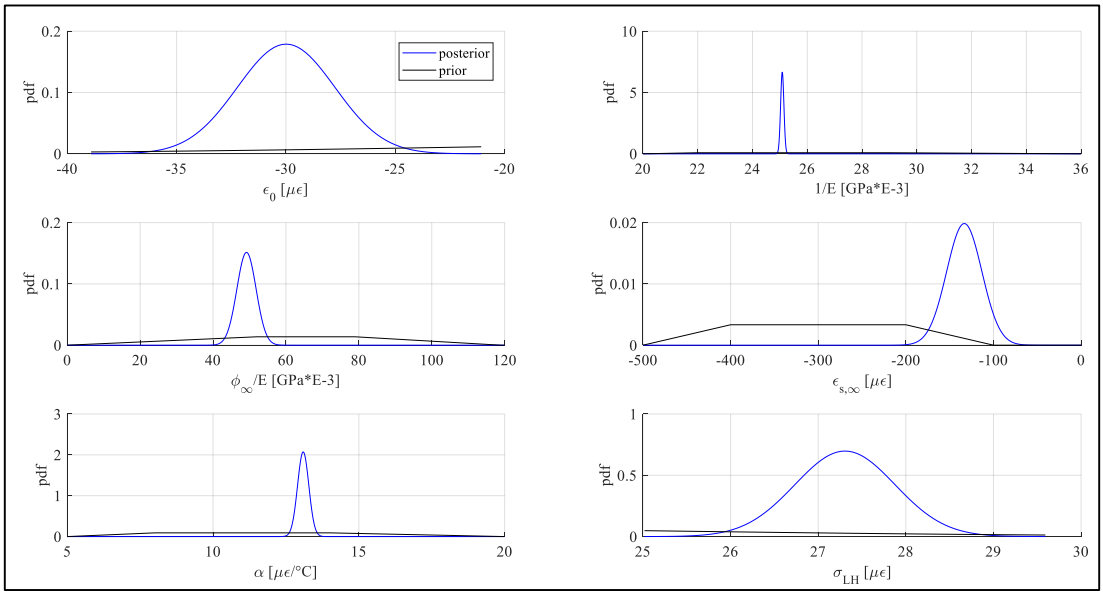

Figure A. 20. Prior (black) vs. Posterior (blue) distributions for the North-East sensor

South-East sensor

Sensor (location)	E[ε₀] [με]	E[1/E] [1/MPaE6]	E[ϕ∞/E] [1/MPaE6]	E[εs,∞] [με]	E[α] [με/°C]	E[σLH] [με]
CT-OD7.5-S-STR-S-1197	-10	25,16	51,15	-281	9,70	30

Table A. 5. CT-OD7.5-S-STR-S-1197 (South-East) BA parameters estimated values

Std[ε₀] [με]	Std[1/E]	Std[ϕ∞/E] [1/MPaE6]	Std[εs,∞] [με]	Std[α] [με/°C]

	[1/MPaE6]			
2	0,12	1,61	12	0,20

From the estimated parameters we can calculate:

- E=39745 MPa;
- φ_∞=2,03.

Using the values obtained with this approach, the temperature compensated strain can be evaluated.

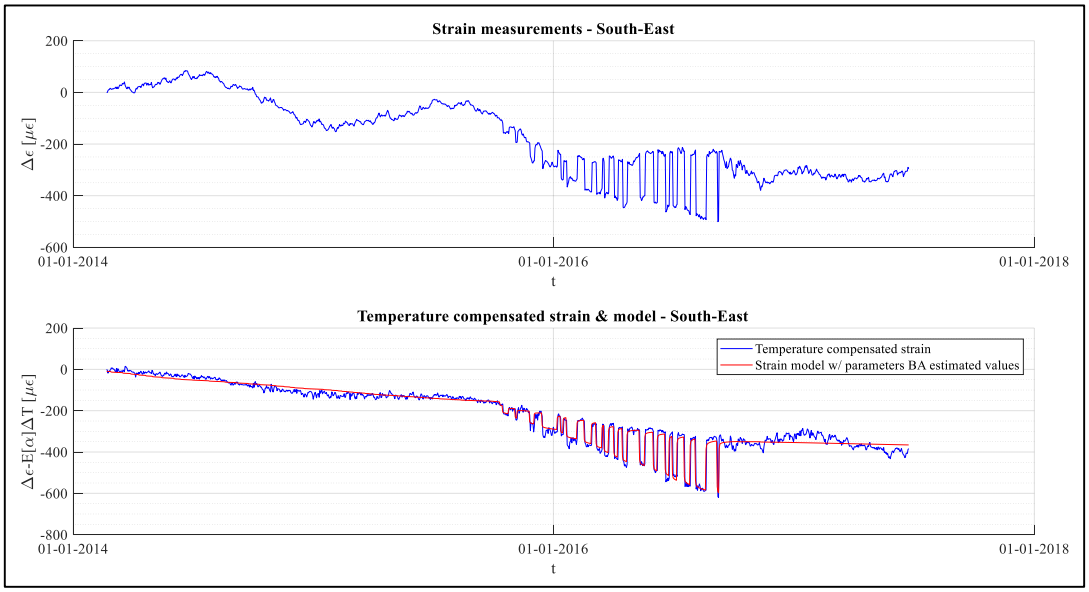

Figure A. 21. Temperature compensated measured strain and model with the parameters BA estimated values for the South-East sensor

At the end of the process, we obtain a posterior distribution for each parameter that is compared with the prior one in the following picture:

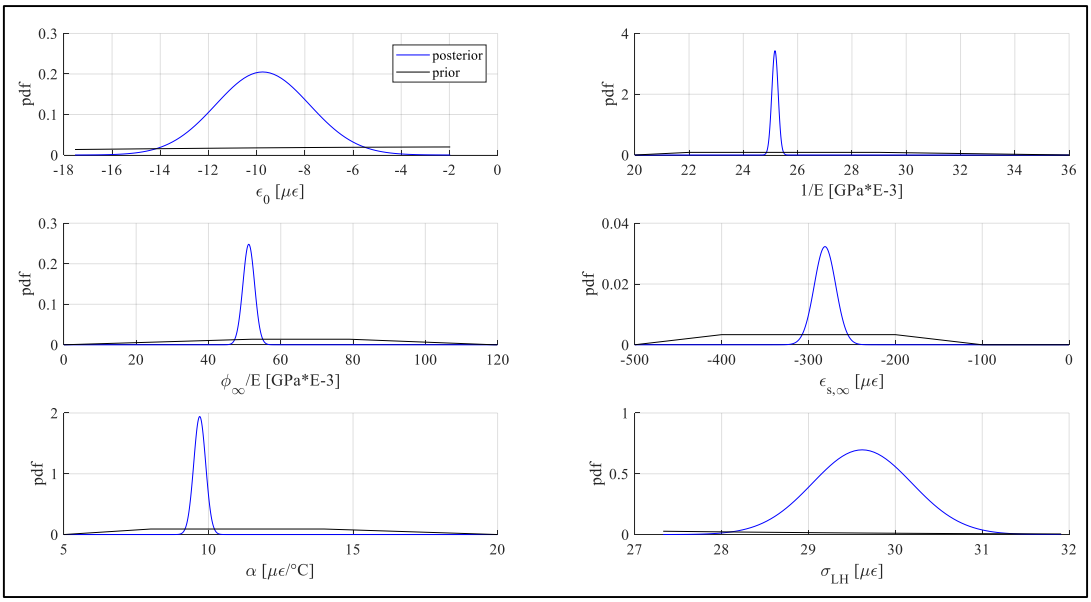

Figure A. 22. Prior (black) vs. Posterior (blue) distributions for the South-East sensor

South-West sensor

Sensor (location)	E[ε₀] [με]	E[1/E] [1/MPaE6]	E[ϕ∞/E] [1/MPaE6]	E[εs,∞] [με]	E[α] [με/°C]	E[σLH] [με]
CT-OD7.5-S-STR-S-1199	-22	25,28	51,70	-286	9,53	30

Table A. 6. CT-OD7.5-S-STR-S-1199 (South-West) BA parameters estimated values

Std[ε₀] [με]	Std[1/E] [1/MPaE6]	Std[ϕ∞/E] [1/MPaE6]	Std[εs,∞] [με]	Std[α] [με/°C]
2	0,19	1,43	9	0,19

From the estimated parameters we can calculate:

- E=39552 MPa;
- φ_∞=2,04.

Using the values obtained with this approach, the temperature compensated strain can be evaluated.

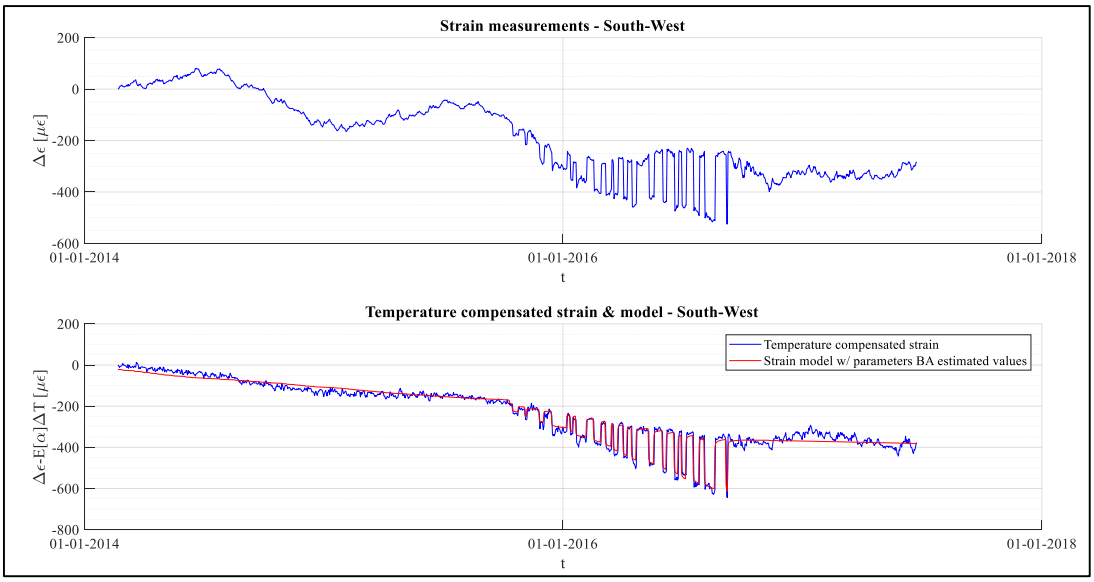

Figure A. 23. Temperature compensated measured strain and model with the parameters BA estimated values for the South-West sensor

At the end of the process, we obtain a posterior distribution for each parameter that is compared with the prior one in the following picture:

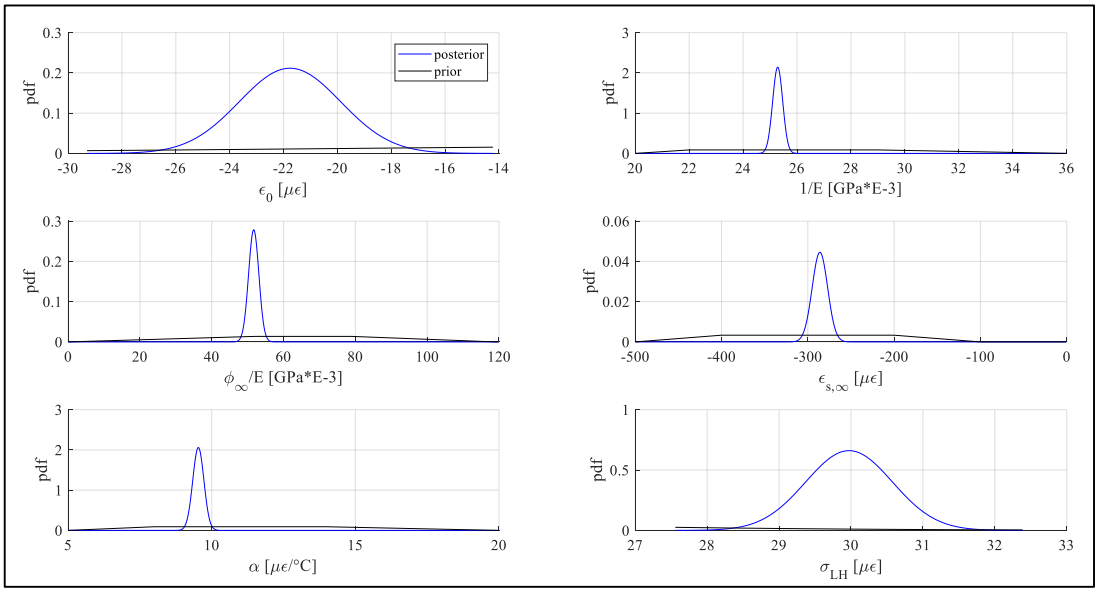

Figure A. 24. Prior (black) vs. Posterior (blue) distributions for the South-West sensor